

## Pharmacological Characterisation of Novel Adenosine Receptor A<sub>3</sub>R Antagonists

Kerry Barkan<sup>1</sup>, Panagiotis Lagarias<sup>2</sup>, Margarita Stampelou<sup>2</sup>, Dimitrios Stamatis<sup>2</sup>, Sam Hoare<sup>3</sup>, Karl-Norbert Klotz<sup>4</sup>, Eleni Vrontaki<sup>2</sup>, Antonios Kolocouris<sup>2\*</sup> and Graham Ladds<sup>1\*</sup>

**Running Title:** Novel antagonists of the A<sub>3</sub>R.

<sup>1</sup> Department of Pharmacology, University of Cambridge, Tennis Court Road, Cambridge, CB2 1PD, UK.

<sup>2</sup> Section of Pharmaceutical Chemistry, Department of Pharmacy, School of Health Sciences, National and Kapodistrian University of Athens, Panepistimiopolis-Zografou, Athens, 15771, Greece.

<sup>3</sup> Pharmechanics LLC, 14 Sunnyside Drive South, Owego, NY 13827, USA

<sup>4</sup> Institute of Pharmacology and Toxicology, University of Würzburg, Versbacher Str. 9 97078 Würzburg, Germany

### Address for correspondence:

Dr Graham Ladds, Department of Pharmacology, University of Cambridge, Tennis Court Road, Cambridge, CB2 1PD Tel; +44 (0) 1223 334020. Email: [grl30@cam.ac.uk](mailto:grl30@cam.ac.uk).

Dr Antonios Kolocouris, Department of Medicinal Chemistry, Faculty of Pharmacy, National and Kapodistrian University of Athens, Panepistimioupolis Zografou, Athens, 15 771. Tel: 210-727-4834, Email: [ankol@pharm.uoa.gr](mailto:ankol@pharm.uoa.gr).

### Author Contributions:

KB, AK and GL conceived and designed the research; KB performed the mammalian assays; KK conducted radioligand binding experiments, PL, DS, EV and AK performed the molecular dynamic simulations; SH derived the equations for the 'Rapid competitor dissociation kinetics' model; KB, GL and AK analysed data; KB and GL wrote manuscript, AK revised and edited the manuscript.

## Summary

### *Background and Purpose*

The adenosine A<sub>3</sub> receptor (A<sub>3</sub>R) belongs to a family of four adenosine receptor (AR) subtypes which all play distinct roles throughout the body. A<sub>3</sub>R antagonists have been described as potential treatments for numerous diseases including asthma. Given the similarity between ARs orthosteric binding sites, obtaining highly selective antagonists is a challenging but critical task.

### *Experimental approach*

39 potential A<sub>3</sub>R, antagonists were screened using agonist-induced inhibition of cAMP. Positive hits were assessed for AR subtype selectivity through cAMP accumulation assays. The antagonist affinity was determined using Schild analysis (pA<sub>2</sub> values) and fluorescent

ligand binding. Further, a likely binding pose of the most potent antagonist (K18) was determined through molecular dynamic (MD) simulations and consistent calculated binding free energy differences between K18 and congeners, using a homology model of A<sub>3</sub>R, combined with mutagenesis studies.

### *Key Results*

We demonstrate that K18, which contains a 3-(dichlorophenyl)-isoxazole group connected through carbonyloxycarboximidamide fragment with a 1,3-thiazole ring, is a specific A<sub>3</sub>R (<1 μM) competitive antagonist. Structure-activity relationship investigations revealed that loss of the 3-(dichlorophenyl)-isoxazole group significantly attenuated K18 antagonistic potency. Mutagenic studies supported by MD simulations identified the residues important for binding in the A<sub>3</sub>R orthosteric site. Finally, we introduce a model that enables estimates of the equilibrium binding affinity for rapidly disassociating compounds from real-time fluorescent ligand-binding studies.

### *Conclusions and Implications*

These results demonstrate the pharmacological characterisation of a selective competitive A<sub>3</sub>R antagonist and the description of its orthosteric binding mode. Our findings may provide new insight for drug discovery.

**Word count: 250**

### **Keywords:**

Adenosine A<sub>3</sub> receptor, antagonist, GPCR, mutagenesis, Schild analysis, functional assay, molecular dynamics

### **Conflict of Interest**

None for any author

### **Abbreviations**

AR, adenosine receptor; A<sub>1</sub>R, A<sub>1</sub> adenosine receptor; A<sub>2A</sub>R, A<sub>2A</sub> adenosine receptor; A<sub>2B</sub>R, A<sub>2B</sub> adenosine receptor; A<sub>3</sub>R, A<sub>3</sub> adenosine receptor; CA200645, fluorescent xanthine amine congener; cAMP, adenosine 3',5' cyclic monophosphate; CHO, Chinese hamster ovary, DMSO, dimethyl sulfoxide; DPCPX, 8-cyclopentyl-1,3-dipropyl-7H-purine-2,6-dione; ERK, extracellular signal-regulated kinase; IB-MECA, (2S,3S,4R,5R)-3,4-dihydroxy-5-[6-[(3-iodophenyl)methylamino]purin-9-yl]-N-methyloxolane-2-carboxamide; HEMADO, (2R,3R,4S,5R)-2-(2-hex-1-ynyl-6-methylaminopurin-9-yl)-5-(hydroxymethyl)oxolane-3,4-diol; MRS 1220, N-(9-chloro-2-furan-2-yl-[1,2,4]triazolo[1,5-c]quinazolin-5-yl)-2-phenylacetamide; NECA, (2S,3S,4R,5R)-5-(6-aminopurin-9-yl)-N-ethyl-3,4-dihydroxyoxolane-2-carboxamide; Nluc, Nano-luciferase; Nluc-A<sub>3</sub>R, NanoLuc-labelled A<sub>3</sub> adenosine receptor; PMA (Phorbol 12-myristate 13-acetate); MD; molecular dynamic; MM-PBSA; Molecular Mechanics-Poisson Boltzmann Surface Area; SBDD, structural-based drug design; vdW, van der Waals.

### **What is already known**

- The search for AR subtype specific compounds often leads to ones with multiple subtype binding

### What this study adds

- This study demonstrates the pharmacological characterisation of a selective competitive A<sub>3</sub>R antagonist
- MD simulations identified the residues important for binding in the A<sub>3</sub>R orthosteric site

### Clinical significance

- This study offers insight into A<sub>3</sub>R antagonists that may provide new opportunities for drug discovery

## INTRODUCTION

The [adenosine A<sub>3</sub> receptor](#) (A<sub>3</sub>R), belongs to a family of four [adenosine receptor](#) (AR) subtypes ([A<sub>1</sub>R](#), [A<sub>2A</sub>R](#), [A<sub>2B</sub>R](#) and A<sub>3</sub>R), and is involved in a range of pathologies including cardiovascular, neurological and tumour-related diseases. In particular, mast cell regulation and myocardial preconditioning are key physiological processes regulated by the A<sub>3</sub>R (Fredholm *et al.*, 2011). Unsurprisingly therefore, A<sub>3</sub>R is a pharmaceutical target. Interestingly, the A<sub>3</sub>R has been described as enigmatic, whereby many of the effects attributed to A<sub>3</sub>Rs are contradictory (Gessi *et al.*, 2008). Despite this, A<sub>3</sub>R antagonists having been described as potential treatments of asthma, chronic obstructive pulmonary disease (COPD) and glaucoma (Miwatashi *et al.*, 2008, Okamura *et al.*, 2004, Haeusler *et al.*, 2015), to name a few, and continuous research into both agonists and antagonists at the A<sub>3</sub>R are warranted. While a number of novel potent and selective A<sub>3</sub>R antagonists have been previously described (Yaziji *et al.*, 2011, Yaziji *et al.*, 2013, Areias *et al.*, 2019), one of the challenges associated with the druggability of the AR family has been the targeting of individual subtypes with sufficient specificity to limit off-target side effects (Chen *et al.*, 2013).

Although all AR members are activated by the endogenous agonist [adenosine](#), the A<sub>2A</sub>R and A<sub>2B</sub>R are predominantly G<sub>s</sub>-coupled whereas A<sub>1</sub>R and A<sub>3</sub>R generally couple to G<sub>i/o</sub>. This classical pathway following A<sub>3</sub>R activation and G<sub>i/o</sub> coupling is the inhibition of adenylate cyclase (AC) resulting in a decrease in cAMP levels. Extracellular signal-regulated kinase 1/2 (ERK1/2) activation has also been described as downstream of A<sub>3</sub>R and is reported to be dependent on βγ-subunits released from pertussis toxin (PTX)-sensitive G<sub>i/o</sub> proteins, phosphatidylinositol-3-kinase (PI3K), the small GTP binding protein Ras, and MAP/ERK kinase (MEK) (Schulte and Fredholm, 2002).

The A<sub>2A</sub>R is one of the best structurally characterised G protein-coupled receptors (GPCRs), with multiple crystal structures available (Carpenter *et al.*, 2016, Lebon *et al.*, 2011, Lebon *et al.*, 2015, Xu *et al.*, 2011, Liu *et al.*, 2012, Doré *et al.*, 2011, Jaakola *et al.*, 2008, Cheng *et al.*, 2017). Although the remaining AR subtypes have proven more difficult to crystallise with the A<sub>3</sub>R structure yet to be resolved, there are a number of A<sub>1</sub>R structures published (Draper-Joyce *et al.*, 2018, Glukhova *et al.*, 2017, Cheng *et al.*, 2017). Thus, *in silico* screening of vast compound libraries against receptor structures, known as structural-based drug design (SBDD), offers huge potential in the development of highly selective

ligands (Carlsson *et al.*, 2010, Katritch *et al.*, 2010, Lenseink *et al.*, 2016, Lagarias *et al.*, 2018). The limited availability of diverse high-resolution structures of the remaining AR subtypes bound to pharmacologically distinct ligands has meant there is a discrepancy between the capability to predict compound binding versus pharmacological behaviour; partial agonism, inverse agonism, biased agonist, antagonism, allosteric modulation etc (Sexton and Christopoulos, 2018). With this in mind, the potential antagonists (K1-K25, K28 and K35) identified in our previously published virtual screening investigation and binding experiments (Lagarias *et al.*, 2018) and some newly identified potential antagonists (K26, K27, K29-K34 and K36-K39) were pharmacologically characterised using cAMP accumulation. We were able to identify a potent and selective A<sub>3</sub>R antagonist, K18 (O4-[[3-(2,6-dichlorophenyl)-5-methylisoxazol-4-yl]carbonyl]-2-methyl-1,3-thiazole-4-carboximidamide) and, using molecular dynamic (MD) simulations combined with site-directed mutagenesis, elude to the potential binding site. Binding free energy calculations of similar in structure analogs of K18 were consistent with the proposed A<sub>3</sub>R orthosteric binding area. Kinetic binding experiments of K5, K17 and K18 using a bioluminescence resonance energy transfer (BRET) method combined with functional assays led to the identification of important structural features of K18 for binding and activity. Further evaluation of this compound (and structurally related analogues) may afford a novel therapeutic benefit in pathologies such as inflammation and asthma.

## RESULTS

### Identification of A<sub>3</sub>R selective antagonists

We initially conducted a blinded screen of 39 compounds (K1-39) to identify selective A<sub>3</sub>R antagonists some of which have previously been identified to bind A<sub>1</sub>R, A<sub>3</sub>R or A<sub>2A</sub>R (Lagarias *et al.*, 2018). Our screen was carried out using A<sub>3</sub>R expressing Flp-In™-Chinese hamster ovary (CHO) cells where cAMP accumulation was detected following a combined stimulation of 10 μM forskolin (to allow A<sub>3</sub>R mediated G<sub>i/o</sub> response to be observed), 1 μM tested compound and the predetermined IC<sub>80</sub> concentration of NECA (3.16 nM). Compounds K1-39 were identified by unblinding (Table 1 and Supplementary Table 1) but are hereinafter referred to as their denoted 'K' number. For the purpose of structure-activity relationships studies, the previously uncharacterised compounds (K26, K27, K29-K34 and K36-K39), were assayed both functionally and through radioligand binding (Supplementary Table 1).

Co-stimulation with 10 μM of both forskolin and NECA reduced the cAMP accumulation when compared to 10 μM forskolin alone and this was reversed with the known A<sub>3</sub>R antagonist [MRS 1220](#) (Table 1 and Supplementary Fig 1). Compounds K1, K10, K11, K17, K18, K20, K23, K25 and K32 were identified as potential antagonists at the A<sub>3</sub>R through their ability to elevate cAMP accumulation when compared to forskolin and NECA co-stimulation. Of the nine potential A<sub>3</sub>R antagonists, eight (excluding K11) appeared to be antagonists at the tested concentration of 1 μM (Supplementary Fig. 2 and Supplementary Table 2).

A number of compounds previously documented (K5, K9, K21, K22 and K24; Lagarias *et al.*, 2018) or determined in this study (K26, K27 and K34) to have sub-micromolar binding affinities for A<sub>3</sub>R showed no activity in our cAMP-based screen (Table 1, Supplementary Table 1). To ensure robustness of our functional screen, full inhibition curves of NECA in the presence or absence of tested compounds (1 μM or 10 μM) were constructed in A<sub>3</sub>R Flp-In CHO cells (Supplementary Fig. 3, Supplementary Table. 3). In this preliminary data all nine

compounds (K5, K9, K11, K21, K22, K24, K26, K27 and K34) appeared to reduce the NECA potency at the highest tested concentration (10  $\mu$ M) but showed no effect at 1  $\mu$ M and thus appear to be low potency antagonists at the A<sub>3</sub>R.

### AR subtype selectivity and specificity

The similarity of the different ARs has meant many compounds display reduced selectivity. Using the A<sub>3</sub>R Flp-In CHO or CHO-K1 cells expressing A<sub>1</sub>R, A<sub>2A</sub>R or A<sub>2B</sub>R incubated with a single high concentration of antagonist (10  $\mu$ M) and increasing concentrations of NECA identified K10, K17, K18 and K25 as A<sub>3</sub>R selective antagonists (Fig. 1). K20 and K23 were antagonists at both the A<sub>1</sub>R and A<sub>3</sub>R (Fig. 1 and Table 2). K1, K20 and K23 showed weak antagonism at the A<sub>2A</sub>R and none of the tested antagonist showed any antagonism of the NECA stimulated response at the A<sub>2B</sub>R. These selectivity findings agree with our previously published radioligand binding data (Lagarias *et al.*, 2018) and are summarised in Table 2.

### Characterisation of competitive antagonists at the A<sub>3</sub>R

All eight A<sub>3</sub>R antagonists were confirmed to antagonise [IB-MECA](#) (Fig. 2 and Table 3) and preliminary data suggests this extends to NECA antagonism (Supplementary Fig. 4 and Supplementary Table 4) in a concentration-dependent manner. Schild analysis characterised K10, K17, K18, K20, K23, K25 and K32 as competitive antagonists at the A<sub>3</sub>R (Schild slope not significantly different from unity, Fig. 2). Interestingly, the Schild slope deviated from unity for K1 (in competition experiments with NECA, but not IB-MECA) suggesting a more complicated mechanism of antagonism at the A<sub>3</sub>R. K20 and K23 were also characterised as competitive antagonists at the A<sub>1</sub>R (Supplementary Fig. 5 and Supplementary Table 5).

When comparing the activity of A<sub>3</sub>R selective antagonists (K10, K17, K18 and K25), K18 was the most potent, showed A<sub>3</sub>R specificity and greater A<sub>3</sub>R binding affinity (Table 2) and we propose it as our lead compound. The original competition binding experiments that identified the panel of antagonist was performed using [<sup>3</sup>H]HEMADO (Lagarias *et al.*, 2018). To ensure that the different ligands used in our studies was not influencing our characterisation of the compounds, we assessed the ability of K18 to antagonise cAMP inhibition by HEMADO at the A<sub>3</sub>R and compared its potency to K17 (Supplementary Fig. 6 and Table 6). In this exploratory data K18 again displayed higher potency than K17 at the A<sub>3</sub>R.

In addition, we wanted to determine if K18 could also antagonise the activity of the A<sub>3</sub>R when an alternative downstream signalling component was measured; ERK1/2 phosphorylation (Fig. 3). In line with previously reported findings (Graham *et al.*, 2001; Schulte and Fredholm, 2002), agonists at the A<sub>3</sub>R increased ERK1/2 phosphorylation after 5 minutes, with IB-MECA 10-fold more potent than NECA (Supplementary Fig. 7) and preliminary data suggests this was entirely G<sub>i/o</sub>-mediated (pERK1/2 levels were abolished upon addition of PTX). K18 was able to antagonise A<sub>3</sub>R-mediated phosphorylation of ERK1/2 with the antagonist potency (pA<sub>2</sub> values) not significantly different compared to the cAMP-inhibition assay (Fig. 3C).

### A<sub>3</sub>R constitutive activity and inverse agonism

We next determined if any of our competitive antagonist could function as inverse agonists of the A<sub>3</sub>R. In our hands, the A<sub>3</sub>R, when expressed in Flp-In<sup>TM</sup>-CHO cells, displays constitutive activity (Supplementary Fig. 8). All eight characterised A<sub>3</sub>R antagonists showed a concentration-dependent inverse agonism of the A<sub>3</sub>R when compared to DMSO control (Fig. 2). This was also found to be the case for [DPCPX](#), K20 and K23 at the A<sub>1</sub>R (Supplementary

Fig. 9). Notably, DMSO showed a concentration-dependent elevation in cAMP accumulation above that of forskolin alone.

### MD simulation of the binding mode of K18 at A<sub>3</sub>R

We next sought to investigate the potential binding pose of K18 within the A<sub>3</sub>R orthosteric site. Building upon our previous studies where we have generated a homology model of the A<sub>3</sub>R, K18 was docked into the orthosteric site of the A<sub>3</sub>R using the GoldScore scoring function and the highest scoring pose was inserted in a hydrated POPE bilayer. The complex was subjected to MD simulations in the orthosteric binding site of A<sub>3</sub>R with Amber14ff for 100 ns and the trajectory analysed for protein-ligand interactions. We identified a potential binding pose of K18 within the established orthosteric A<sub>3</sub>R binding pocket (Fig. 4). The MD simulations suggest that K18 forms hydrogen bonds, van der Waals (vdW) and  $\pi$ - $\pi$  interactions inside the orthosteric binding site of A<sub>3</sub>R (Fig. 4A). More specifically, MD simulations showed that the 3-(dichlorophenyl) group is positioned close to V169<sup>5,30</sup>, M177<sup>5,40</sup>, I249<sup>6,54</sup> and L264<sup>7,34</sup> of the A<sub>3</sub>R orthosteric binding site forming attractive vdW interactions. The isoxazole ring is engaged in an aromatic  $\pi$ - $\pi$  stacking interaction with the phenyl group of F168<sup>5,29</sup> (Fig. 4A). The thiazole ring is oriented deeper into the receptor favouring interactions with L246<sup>6,51</sup>, L90<sup>3,32</sup> and I268<sup>7,39</sup>. Hydrogen bonding interactions can be formed between: (a) the amino group of the carbonyloxycarboximidamide molecular segment and the amide side chain of N250<sup>6,55</sup>; (b) the nitrogen or the sulphur atom of the thiazole ring and N250<sup>6,55</sup> side chain (Fig. 4A). For structural comparison and insight, we also modelled K5 and K17 binding at the A<sub>3</sub>R given the structural similarity: K17 and K18 possess one and two chlorine atoms attached to the phenyl ring of the phenyl-isoxazole system, respectively, whereas K5 has none (Fig. 4B and C).

### Molecular Mechanics-Poisson Boltzmann Surface Area (MM-PBSA) calculations validate binding pose of K18

We next applied the MM-PBSA method in the MD simulation trajectories of the compounds to calculate their binding free energies ( $\Delta G_{\text{eff}}$  - see methods for derivation (Stamatis *et al.*, 2019)) and evaluated the energetic contributions for their binding (Table 4). The calculated ranking in the binding free energies were in agreement with experimental differences in potencies (K5 < K17 < K18 < MRS 1220). The known A<sub>3</sub>R antagonist MRS 1220 displayed the lowest  $\Delta G_{\text{eff}}$  value, which is also in agreement with the experimental potencies. The calculations suggested that the major difference between the energetic components of  $\Delta G_{\text{eff}}$  values for K5, K17 and K18 is on the solvation energies ( $\Delta G_{\text{solv}}$ ). The two chlorine atoms make K18 more lipophilic and reduce the energy required to transfer the compound from solution to the binding area, increasing the free energy of binding and activity compared to K17 and K5.

### MD simulation of the binding mode of analogs of K18 at A<sub>3</sub>R

Significantly, when the 4-thiazolyl in K17 was changed to 2-,3- or 4-pyridinyl in compounds K32, K10, K11 we observed antagonistic activity only for compounds K32 and K10 (not K11) (Table 1) since the pyridine nitrogen in compounds K32 and K10 can interact with N250<sup>6,55</sup> due to their proximate positions in binding conformation (see Fig. 4B for K17). This interaction is preserved with both the 2-,3-pyridinyl groups but lost when the nitrogen of the pyridinyl group is in the 4-position. In addition, following MD simulations of compounds K26, K27, K29-K34 and K36-K39, we observed that K26 (Supplementary Fig. 10) displayed a similar binding pose to that of K18 (Fig. 4). However, K26 (and K34 for that matter) which containing a *o*-diphenylcarbonyl (also present in K18) functionally showed weak antagonistic potency (> 1  $\mu$ M, Supplementary Fig. 2) suggesting a more complex binding mode is present. We also

observed that compared to K26 and K34, the p-substitution in compounds K29 and K36-38 was not favourable for binding at all since this led to a loss of the vdW interaction with the hydrophobic area of the A<sub>3</sub>R towards TM5 and TM6; as was demonstrated in MD simulations for K36 (Supplementary Fig. 10).

### Experimental evaluation of the binding mode of K18 at A<sub>3</sub>R

Of the identified residues predicted to mediate an interaction between K18 and the A<sub>3</sub>R, the ones which showed (according to the MD simulations) the most frequent and the most important contacts were chosen for investigation and included amino acids L90<sup>3.32</sup>, F168<sup>5.29</sup>, V169<sup>5.30</sup>, M177<sup>5.40</sup>, L246<sup>6.51</sup>, I249<sup>6.54</sup>, N250<sup>6.55</sup>, L264<sup>7.34</sup> and I268<sup>7.39</sup> (Fig. 4). Site-directed mutagenesis was performed replacing each residue with an alanine in the A<sub>3</sub>R and expressed in the Flp-In-CHO™ cells lines. Each mutant was then screened for their ability to suppress forskolin-induced cAMP accumulation in response to NECA/IB MECA stimulation in the presence and absence of K18.

Mutation of residues F168<sup>5.29</sup>, L246<sup>6.51</sup>, N250<sup>6.55</sup> and I268<sup>7.39</sup> abolished agonist induced suppression of forskolin-induced cAMP accumulation and were discontinued in this study (Stamatis *et al.*, 2019). Both L90A<sup>3.32</sup> and M177A<sup>5.40</sup> showed a significantly decreased NECA and IB-MECA potency. L264A<sup>7.34</sup> showed a slight decrease in IB-MECA potency whereas the potency of NECA was similar to WT. Whereas the NECA stimulated cAMP inhibition in V169A<sup>5.30</sup> or I249A<sup>6.54</sup> expressing Flp-In CHOs was comparable to WT, the IB-MECA stimulated cAMP inhibition was enhanced in potency (Table 5). Mutation of V169<sup>5.30</sup> to glutamate, the amino acid present in other AR subtypes, enhanced both NECA and IB-MECA potency.

Further, the affinity (pA<sub>2</sub>) of K18 at the WT and mutant A<sub>3</sub>R were compared in order to determine the potential antagonist binding site (Fig. 5, Table 5). K18 displayed no difference in affinity at I249A<sup>6.54</sup> (compared to WT), whereas M177A<sup>5.40</sup> and V169A<sup>5.30</sup> were significantly smaller. Interestingly, we found an increase in the affinity for L90A<sup>3.32</sup> and L264A<sup>7.34</sup> when compared to WT. As would be expected, the K18 affinity at the A<sub>3</sub>R mutants was not different between agonists, confirming agonist independence (Supplementary Fig. 11). These experimental findings are reflected in our predicted binding pose of K18 at the WT A<sub>3</sub>R (Fig. 4).

### Kinetics of A<sub>3</sub>R antagonists determined through BRET

NanoBRET techniques have been successfully used to determine the real-time kinetics of ligand binding to GPCRs (Stoddart *et al.*, 2018, Sykes *et al.*, 2019, reviewed in Soave *et al.*, 2019). Here, we investigated the ability of the selective A<sub>3</sub>R antagonists MRS 1220, K17 or K18 to inhibit specific binding of the fluorescent A<sub>3</sub>R antagonist CA200645 to Nluc-A<sub>3</sub>R (Stoddart *et al.*, 2015, Bouzo-Lorenzo *et al.*, 2019). The kinetic parameters for CA200645 at Nluc-A<sub>3</sub>R were initially determined as K<sub>on</sub> (k<sub>1</sub>) = 2.86 ± 0.89 × 10<sup>7</sup> M<sup>-1</sup>, K<sub>off</sub> (k<sub>2</sub>) = 0.4397 ± 0.014 min<sup>-1</sup> with a K<sub>D</sub> of 17.92 ± 4.45 nM. (Supplementary Fig 12). Our MRS 1220 kinetic data was fitted with the original 'kinetic of competitive binding' model (Motulsky and Mahan, 1984; built into GraphPad Prism 8.0) with a determined K<sub>on</sub> (k<sub>3</sub>) and K<sub>off</sub> (k<sub>4</sub>) rate of 3.25 ± 0.28 × 10<sup>8</sup> M<sup>-1</sup> min<sup>-1</sup> and 0.0248 ± 0.005 min<sup>-1</sup>, respectively. This gave a residence time (RT) (RT = 1/K<sub>off</sub>) of 40.32 min. It was noticed in the analysis for K5, K17 and K18 that the fit in some cases was ambiguous (Regression with Prism 8: "Ambiguous", 2019) and/or the fitted value of the compound dissociation rate constant was high (k<sub>4</sub> > 1 min<sup>-1</sup>, corresponding to a dissociation t<sub>1/2</sub> of < 42 sec). In order to determine the reliability of the fitted k<sub>4</sub> value, data were also analysed using an equation that assumes compound dissociation is too rapid for the

dissociation rate constant to be determined reliably and the fits to the two equations were compared (“Kinetics of competitive binding, rapid competitor dissociation”, derived in the Appendix I). This model allowed estimate of the equilibrium binding affinity of the compound ( $K_i$ ) but not the binding kinetics of K5, K17 and K18 (Supplementary Fig. 13 and Table 4). These affinity values were in agreement with those obtained via Schild analysis (except for K5) and were approximately 10-fold higher than those determined through radioligand binding (Table 4). Notably, the order of affinity ( $K5 < K17 < K18$ ) was consistent.

### Assessing the species selectivity of A<sub>3</sub>R antagonists

There is a lack of selective antagonists for the rat A<sub>3</sub>R with only a small number reported including the 6-phenyl-1,4-dihydropyridine MRS 1191 and the trazoloquinazoline MRS 1220 which both bind the human A<sub>3</sub>R (Jacobson *et al.*, 1997). Comparison of residues of the binding area between human and rat A<sub>3</sub>R show that they differ in residues 167<sup>5,28</sup>, 169<sup>5,30</sup>, 176<sup>5,37</sup>, 253<sup>6,58</sup>, 264<sup>7,34</sup> (Supplementary Fig. 14). The scarcity of rat A<sub>3</sub>R antagonists prompted us to investigate if our characterised compounds were also potential antagonists at the rat A<sub>3</sub>R. Using a Nluc-tagged rat A<sub>3</sub>R expressing HEK 293 cell line, we conducted NanoBRET ligand-binding experiments whereby we determined the ability of our compounds to inhibit specific binding of the fluorescent antagonist AV039 to Nluc-rat A<sub>3</sub>R. As expected, AV039 was displaced by increasing concentrations of MRS 1220 ( $pK_i$  6.788 ± 0.1) (Supplementary Fig. 15 and Supplementary Table 7). We found very weak binding of K17, K18, K10 and K32, with no binding detected below the concentration of 10 μM, whereas K1, K20, K23 and K25 were determined as potential rat A<sub>3</sub>R antagonists ( $pK_i$  6.07 ± 0.04, 5.71 ± 0.03, 5.93 ± 0.04 and 6.37 ± 0.06, respectively) (Supplementary Fig. 15 and Supplementary Table 7). K25 had a higher binding affinity for the rat A<sub>3</sub>R when compared to the human A<sub>3</sub>R (Table 1) ( $pK_i$  6.37 ± 0.1 and 5.81, respectively).

MD simulations of the rat A<sub>3</sub>R (performed as described previously for the human A<sub>3</sub>R) suggested that the presence of M264<sup>7,34</sup> most likely hampers K18 binding due to steric hindrance of the dichloro-phenyl group (Supplementary Fig. 16). In contrast, MD simulations of K25 against rat A<sub>3</sub>R showed the formation of stable complex (Supplementary Fig. 17). Here, the 2-amido group of the thiophene ring is hydrogen-bonded to the amido group of N250<sup>6,55</sup>. The thiophene ring forms aromatic π-π stacking interaction with F168<sup>5,29</sup> and the 5-(p-chlorophenyl) is oriented deep in the binding area making contacts with L90<sup>3,32</sup>, L246<sup>6,51</sup> and W243<sup>6,48</sup>. M264<sup>7,34</sup> forces the large lipophilic moiety of the thiophene ring (3-NHCOCH<sub>2</sub>SPh(CF<sub>3</sub>)<sub>2</sub>) of K25 to locate close to TM2 favouring contacts with A69<sup>2,61</sup>, V72<sup>2,64</sup>, and I268<sup>7,39</sup> (Supplementary Fig. 17).

### Pharmacokinetic assessments of K18

The metabolic *in vitro*  $t_{1/2}$  (human liver microsomes, 0.1 mg/mL) of K18 (0.1 μM) was determined (0 to 60 minutes) as 24 minutes and the intrinsic clearance ( $CL_{int}$ ) calculated as 287.2 μl/min/mg (Supplementary Figure 18). This was comparable to the reference compound verapamil and terfenadine (0.1 μM) with  $t_{1/2}$  determined as 35 and 12 minutes and  $CL_{int}$  as 200.1 or 581.1 μl/min/mg, respectively. Human plasma stability assessment determined the percentage of K18 (1 μM) remaining after 120 minutes as 90%, with a  $t_{1/2}$  of >120 minutes. This is considerably higher than the reference compound propranolol (1 μM) which was determined to have a half-life of 55 minutes. The  $t_{1/2}$  of K18 (1 μM) in PBS (pH 7.4) over 240 minutes was determined as >240 minutes, with 87% remaining at 240 minutes and was comparable to the reference compound propranolol (1 μM), with a determined  $t_{1/2}$  of >240 minutes.



## DISCUSSION

*In silico* SBDD efforts in ligand discovery, have proven to be highly successful (Meng *et al.*, 2011). However, given the broad and similar orthosteric binding site of ARs, the search for an AR subtype specific compound often leads to compounds active at more than one of the AR subtypes (Kolb *et al.*, 2012). Given that AR subtypes play distinct roles throughout the body, obtaining highly specific receptor antagonists and agonists is crucial. Here, we presented the pharmacological characterisation of eight A<sub>3</sub>R antagonists identified through virtual screening. Of these eight compounds, K10, K17, K18, K20, K23, K25 and K32 were determined to be competitive. Whereas K20 and K23 were antagonists at both the A<sub>1</sub>R and A<sub>3</sub>R, K10, K17, K18, K25 and K32 were A<sub>3</sub>R selective antagonists. Indeed, we found no functional activity, or indeed binding affinity (< 30 μM), at the other AR subtypes.

K1, K20 and K23 showed weak antagonism of the A<sub>2A</sub>R (Figure 1, Table 2). We also tested the compounds at the A<sub>2B</sub>R and determined none of the compound showed A<sub>2B</sub>R antagonistic potency (Figure 1, Table 2). These selectivity findings were in agreement with our radioligand binding data (presented here (Supplementary Table 1) and in Lagarias *et al.*, 2018 for K1-25, K28 and K35). However, a number of compounds previously determined to have micromolar binding affinity for A<sub>3</sub>R (K5, K9, K21, K22, K24, K26, K27 and K34), showed no antagonistic potency in our initial functional screen. Further testing confirmed that these compounds were low potency antagonists and, although supporting the previously published radioligand binding data, confirmed the need for functional testing: not all compounds with binding affinity showed high functional potency.

We showed the A<sub>3</sub>R, when expressed in Flp-In<sup>TM</sup>-CHO cells, displays constitutive activity. Compounds which preferably bind to the inactive (R) state, decreasing the level of constitutive activity (Giraldo *et al.*, 2007) and in the case of a G<sub>i/o</sub>-coupled GPCR leading to an elevated cAMP, are referred to as inverse agonists. All eight characterised A<sub>3</sub>R antagonists and both characterised A<sub>1</sub>R antagonists (K20 and K23) were found to act as inverse agonists. We also reported an elevation in cAMP accumulation when cells were stimulated with DMSO, which was concentration-dependent. Given that even low concentrations of DMSO has been reported to interfere with important cellular processes (Tunçer *et al.*, 2018), the interpretation of these data should be made with caution. The initial virtual screening described in Lagarias *et al.*, 2018 was carried out using a combination of a ligand-based and structure-based strategy and the experimental structure of A<sub>2A</sub>R in complex with the antagonist ZM241385 (PDB ID 3EML) (Jaakola *et al.*, 2008), described as A<sub>2A</sub>R selective antagonist and inverse agonist (Lebon *et al.*, 2011). Our high hit rate for A<sub>3</sub>R selective antagonist appears counter-intuitive since the ligand-based virtual screening tool Rapid Overlay of Chemical Structures (ROCS) was used to predict structures similar to ZM241385 (Lagarias *et al.*, 2018). Indeed, ZM241385 has little affinity for A<sub>3</sub>R and 500- to 1000-fold selectivity for A<sub>2A</sub>R over A<sub>1</sub>R. However, as has been previously reported, the search for an AR subtype specific compound often leads to compounds active at multiple AR subtypes (Kolb *et al.*, 2012), likely due to their similar binding site.

We hypothesized that the presence of a chloro substituent in the phenyl ring of 3-phenyl-isoxazole favoured A<sub>3</sub>R affinity and activity, as following 0Cl < 1Cl < 2Cl i.e. K5 < K17 < K18. This theory is supported by both our radioligand binding, NanoBRET ligand-binding and functional data which determine the relative potency and affinity of the three related compounds K5, K17 and K18 as K5 < K17 < K18. The MD simulations showed that these

compounds adopted a similar binding mode at the A<sub>3</sub>R orthosteric binding site, but the free-energy MM-PBSA calculations showed that K18, having two chlorine atoms and an increased lipophilicity, leaves the solution state more efficiently and enters the highly lipophilic binding area.

For the first time, we have demonstrated the utilisation of a new model which expands on the ‘Kinetic of competitive binding’ model (Motulsky and Mahan, 1984; built into Prism) for fitting fast kinetics data obtained from NanoBRET experiments and assumes the unlabelled ligand rapidly equilibrates with the free receptor. Very rapid competitor dissociation can lead to failure of the fit, eliciting either an ambiguous fit (Regression with Prism 8: “Ambiguous”, 2019) or unrealistically large K<sub>3</sub> and K<sub>4</sub> values. Whereas we were able to successfully fit the MRS 1220 kinetic data with the Motulsky and Mahan model due to its slow dissociation, fitting of K5, K17 and K18 kinetic data with this model often resulted in an ambiguous fit. Our new model, assuming fast compound dissociation, successfully fit the data and allowed the determination of binding affinity. In the cases where the data was able to fit the Motulsky and Mahan model, the dissociation constant was higher (of the order of 1 min<sup>-1</sup>), indicating rapid dissociation. Although we found nearly a 10-fold differences in determined binding affinity for MRS 1220, K5, K17 and K18 between BRET ligand binding and radioligand binding assays, we demonstrated the order of affinity remains consistent. Indeed, this was seen across all three experimental approaches: Schild analysis, NanoBRET ligand-binding assay and radioligand binding.

Our MD simulations describe the potential binding site of K18, our most potent and selective A<sub>3</sub>R antagonist, within the A<sub>3</sub>R orthosteric binding area (Fig. 4A). Here, K18 is stabilised through hydrogen bonding interactions between the amino group and thiazole ring of the ligand and the amide side chain of N250<sup>6.55</sup>. In addition, the dichloro-phenyl ring can be oriented to the unique lipophilic area of A<sub>3</sub>R including V169<sup>5.30</sup>, M177<sup>5.40</sup>, I249<sup>6.54</sup> and L264<sup>7.34</sup> stabilized in that cleft through attractive vdW interactions; K18 is further stabilized through  $\pi$ - $\pi$  aromatic stacking interactions between isoxazole ring and the phenyl group of F168<sup>5.29</sup> and the thiazole group is oriented deeper into the receptor favouring interactions with L246<sup>6.51</sup> and L90<sup>3.32</sup> and possibly with I268<sup>7.39</sup>. The determination of critical residues for antagonist binding becomes particularly difficult in the case of competitive antagonists whereby important amino acids are likely overlapping with those for agonist binding. In combination with our mutagenesis data, the final binding pose of K18 appears to be within the orthosteric binding site, involving residues previously described to be involved in binding of A<sub>3</sub>R compounds (Arruda *et al.*, 2017). We reported no detectable G<sub>i/o</sub> response following co-stimulation with forskolin and NECA or IB-MECA for A<sub>3</sub>R mutants F168A<sup>5.29</sup>, L246A<sup>6.51</sup>, N250A<sup>6.55</sup> and I268A<sup>7.39</sup> (Stamatis *et al.*, 2019). These findings are in line with previous mutagenesis studies investigating residues important for agonist and antagonist binding at the human A<sub>3</sub>R (Gao *et al.*, 2002, May *et al.*, 2012). L90A<sup>3.32</sup>, V169A<sup>5.30</sup>, M177A<sup>5.40</sup>, I249A<sup>6.54</sup> and L264A<sup>7.34</sup> A<sub>3</sub>R all showed a detectable G<sub>i/o</sub> response when stimulated with agonists (Stamatis *et al.*, 2019).

Through performing Schild analysis (results of which were used to inform modelling in Lagarias *et al.*, 2019) we were able to experimentally determine the effect of receptor mutation on antagonist affinity for L90A<sup>3.32</sup>, V169A/E<sup>5.30</sup>, M177A<sup>5.40</sup>, I249A<sup>6.54</sup> and L264A<sup>7.34</sup> A<sub>3</sub>R. The pA<sub>2</sub> value for I249A<sup>6.54</sup> A<sub>3</sub>R was similar to WT, whereas M177A<sup>5.40</sup> and V169A<sup>5.30</sup> were significantly smaller suggesting these residues appear to be involved in K18 binding. Interestingly we found an increase in the pA<sub>2</sub> for L90A<sup>3.32</sup> and L264A<sup>7.34</sup> when compared to WT, suggesting an enhanced ability of K18 to act as an antagonist. Further evidence was provided by the MM-PBSA calculations which were in agreement, based on the proposed binding model, between the calculated binding free energy by congeners of K18 having one

or no chlorine atoms, i.e. compounds K17 and K5, and the known A<sub>3</sub>R antagonist MRS 1220, and binding affinities and antagonistic potencies. Importantly, substitution of the 1,3-thiazole ring in K17 with either a 2-pyridinyl ring (K32) or a 3-pyridinyl ring (K10) but not a 4-pyridinyl ring (K11) maintained A<sub>3</sub>R antagonistic potency. Although we have not directly determined the effects of similar pyridinyl ring substitutions on the higher affinity antagonist K18, we suspect there would be no significant increase in the potency of K18 given the small changes we observed for K17.

The human and rat A<sub>3</sub>R display 72% homology (Salvatore *et al.*, 1993). Antagonists that are A<sub>3</sub>R-selective across species or at rat A<sub>3</sub>R alone are useful pharmacological tools to define the role of these receptors. The lack of rat A<sub>3</sub>R selective antagonists prompted us to investigate if our characterised A<sub>3</sub>R antagonists were potential antagonists at the rat A<sub>3</sub>R. We reported no binding of our lead A<sub>3</sub>R antagonist, K18, at the rat A<sub>3</sub>R and MD simulations suggest this is due to steric hinderance by M264<sup>7,34</sup>. This finding suggests that K18 may not only be A<sub>3</sub>R specific within the human ARs but may also be selective across species. Of the compounds that showed rat A<sub>3</sub>R binding (K1, K20, K23 and K25), K25 showed the highest binding affinity and represents an interesting candidate for further investigation. MD simulations showed K25 forms a stable complex with rat A<sub>3</sub>R and we reported a potential binding pose.

In conclusion, through pharmacological characterisation of a number of potential A<sub>3</sub>R antagonists, this study has determined K18 as a specific (<1 μM) A<sub>3</sub>R competitive antagonist. Our mutagenic studies, supported by MD simulations, identified the residues important for K18 binding are located within the orthosteric site of the A<sub>3</sub>R. Importantly, the absence of a chloro substituent, as is the case in K5, led to affinity loss. Further MD simulations have investigated the selectivity profile of K18 and have demonstrated that K18 failed to bind A<sub>1</sub>R and A<sub>2A</sub>R due to a more polar area close to TM5, TM6 when compared to A<sub>3</sub>R (Lagarias *et al.*, 2019). While a number of novel potent and selective A<sub>3</sub>R antagonists have been previously described (Yaziji *et al.*, 2011, Yaziji *et al.*, 2013, Areias *et al.*, 2019) we present findings of a unique scaffold which can be used as a starting point for detailed structure-activity relationships (SARs) and represents a useful tool that warrants further assessment for its therapeutic potential.

## MATERIALS AND METHODS

### Cell culture and Transfection

Cell lines were maintained using standard subculturing routines as guided by the European Collection of Cell Culture (ECACC) and checked annually for mycoplasma infection using an EZ-PCR mycoplasma test kit from Biological Industries (Kibbutz Beit-Haemek, Israel). All procedures were performed in a sterile tissue culture hood using aseptic technique and solutions used in the propagation of each cell line were sterile and pre-warmed to 37°C. All cells were maintained at 37°C with 5% CO<sub>2</sub>, in a humidified atmosphere. This study used CHO cell lines as a model due to the lack of endogenous AR subtype expression (Brown *et al.*, 2008). CHO-K1-A<sub>1</sub>R, CHO-K1-A<sub>2A</sub>R, CHO-K1-A<sub>2B</sub>R and CHO-K1-A<sub>3</sub>R cells were routinely cultured in Hams F-12 nutrient mix (21765029, Thermo Fisher Scientific) supplemented with 10% Foetal bovine serum (FBS) (F9665, Sigma-Aldrich). Flp-In-CHO cells purchased from Thermo Fisher Scientific (R75807) were maintained in Hams F-12 nutrient mix supplemented with 10% FBS containing 100 μg/mL Zeocin™ Selection Antibiotic (Thermo Fisher Scientific).

Stable Flp-In-CHO cell lines were generated through co-transfection of the pcDNA5/FRT expression vector (Thermo Fisher Scientific) containing the gene of interest and the Flp recombinase expressing plasmid, pOG44 (Thermo Fisher Scientific). Transfection of cells seeded in a T25 flask at a confluency of  $\geq 80\%$  was performed using TransIT<sup>®</sup>-CHO Transfection Kit (MIR 2174, Mirus Bio), in accordance with the manufacturer's instructions. Here, a total of 6  $\mu\text{g}$  of DNA (receptor to pOG44 ratio of 1:9) was transfected per flask at a DNA:Mirus reagent ratio of 1:3 (w/v). 48 hours post-transfection, selection using 600  $\mu\text{g}/\text{mL}$  hygromycin B (Thermo Fisher Scientific) (concentration determined through performing a kill curve) was performed for two days prior to transferring the cells into a fresh T25 flask. Stable Flp-In-CHO cell lines expressing the receptor of interest were selected using 600  $\mu\text{g}/\text{mL}$  hygromycin B whereby the media was changed every two days. Successful mutant cell line generation for non-signalling mutants were confirmed by Zeocin<sup>™</sup> sensitivity (100  $\mu\text{g}/\text{mL}$ ).

The Nluc-tagged human A<sub>3</sub>R expressing HEK 293 cell line along with the Nluc-tagged rat A<sub>3</sub>R pcDNA3.1+ construct for the generation of stable Nluc-tagged rat A<sub>3</sub>R expressing HEK 293 cells were kindly gifted to us by Stephen Hill and Stephen Briddon (University of Nottingham). HEK 293 cells in a single well of 6-well plate (confluency  $\geq 80\%$ ) were transfected with 2  $\mu\text{g}$  of DNA using polyethyleneimine (PEI, 1 mg/ml, MW = 25,000 g/mol) (Polysciences Inc) at a DNA:PEI ratio of 1:6 (w/v). Briefly, DNA and PEI were added to separate sterile tubes containing 150 mM sodium chloride (NaCl) (total volume 50  $\mu\text{l}$ ), allowed to incubate at room temperature for 5 minutes, mixing together and incubating for a further 10 minutes prior to adding the combined mix dropwise to the cells. 48 hours post-transfection, stable Nluc-rat A<sub>3</sub>R expressing HEK 293 cell were selected using 600  $\mu\text{g}/\text{mL}$  Geneticin (Thermo Fisher Scientific) whereby the media was changed every two days. HEK 293 cell lines were routinely cultured in DMEM/F-12 GlutaMAX<sup>™</sup> (Thermo Fisher Scientific) supplemented with 10% FBS (F9665, Sigma-Aldrich).

### Constructs

The human A<sub>3</sub>R originally in pcDNA3.1+ (ADRA3000000, cdna.org) was cloned into the pcDNA5/FRT expression vector and co-transfected with pOG44 to generate a stable Flp-In-CHO cell line. Mutations within the A<sub>3</sub>R were made using the QuikChange Lightning Site-Directed Mutagenesis Kit (Agilent Technologies) in accordance with the manufacturer's instructions. The Nluc-tagged rat A<sub>3</sub>R pcDNA3.1+ construct, used in the generation of the stable Nluc-tagged rat A<sub>3</sub>R expressing HEK 293 cell line was kindly gifted to us by Stephen Hill and Stephen Briddon (University of Nottingham). All oligonucleotides used for mutagenesis were designed using the online Agilent Genomics 'QuikChange Primer Design' tool and are detailed in Stamatis *et al.*, 2019 (Table S4) and purchased from Merck. All constructs were confirmed by in-house Sanger sequencing.

### Compounds

Adenosine, NECA ((2S,3S,4R,5R)-5-(6-aminopurin-9-yl)-N-ethyl-3,4-dihydroxyoxolane-2-carboxamide), IB-MECA ((2S,3S,4R,5R)-3,4-dihydroxy-5-[6-[(3-iodophenyl)methylamino]purin-9-yl]-N-methyloxolane-2-carboxamide), HEMADO ((2R,3R,4S,5R)-2-(2-hex-1-ynyl-6-methylaminopurin-9-yl)-5-(hydroxymethyl)oxolane-3,4-diol), DPCPX (8-cyclopentyl-1,3-dipropyl-7H-purine-2,6-dione) and MRS 1220 (N-(9-chloro-2-furan-2-yl-[1,2,4]triazolo[1,5-c]quinazolin-5-yl)-2-phenylacetamide) were purchased from Sigma-Aldrich and dissolved in dimethyl-sulphoxide (DMSO). CA200645, a high affinity AR xanthine amine congener (XAC) derivative containing a polyamide linker connected to the BY630 fluorophore, was purchased from HelloBio (Bristol, UK) and dissolved in DMSO.

AV039, a highly potent and selective fluorescent antagonist of the human A<sub>3</sub>R based on the 1,2,4-Triazolo[4,3-a]quinoxalin-1-one linked to BY630 (Vernall *et al.*, 2012), was kindly gifted to us by Stephen Hill and Stephen Briddon (University of Nottingham). PMA was purchased from Sigma-Aldrich. Compounds under investigation were purchased from e-molecules and dissolved in DMSO. The concentration of DMSO was maintained to <1.5% across all experiments (1.26% for all cAMP assays, 1% for pERK1/2 assays and 1.02% or 1.1% for NanoBRET ligand-binding experiments using CA200645 or AV039, respectively).

### **cAMP accumulation assay**

For cAMP accumulation (A<sub>2A</sub>R and A<sub>2B</sub>R) or inhibition (A<sub>1</sub>R or A<sub>3</sub>R) experiments, cells were harvested and re-suspended in stimulation buffer (PBS containing 0.1% BSA and 25 μM rolipram) and seeded at a density of 2,000 cells per well of a white 384-well Optiplate and stimulated for 30 minutes with a range of agonist concentrations. In order to allow the A<sub>1</sub>R/A<sub>3</sub>R mediated G<sub>i/o</sub> response to be determined, co-stimulation with forskolin, an activator of AC (Zhang *et al.*, 1997), at the indicated concentration (depending on cell line) was performed. For testing of potential antagonists, cells received a co-stimulation stimulated with forskolin, agonist and compound/DMSO control. cAMP levels were then determined using a LANCE® cAMP kit as described previously (Knight *et al.*, 2016). In order to reduce evaporation of small volumes, the plate was sealed with a ThermalSeal® film (EXCEL Scientific) at all stages.

### **Phospho-ERK assay**

ERK1/2 phosphorylation was measured using the homogeneous time resolved fluorescence (HTRF)® Phospho-ERK (T202/Y204) Cellular Assay Kit (Cisbio Bioassays, Codolet, France) two-plate format in accordance with the manufacturer's instructions. A<sub>3</sub>R expressing Flp-In-CHO were seeded at a density of 2,000 cells per well of a white 384-well Optiplate and stimulated with agonist and test compounds for 5 minutes at 37°C. Plate reading was conducted using a Mithras LB 940 (Berthold technology). All results were normalised to 5 minutes stimulation with 1 μM PMA, a direct protein kinase C (PKC) activator (Jiang and Fleet, 2012). To determine if the measured pERK1/2 level was G<sub>i</sub>-mediated, we treated cells with Pertussis toxin (PTX) (Tocris Biosciences) for 16 hours at 100 ng/mL prior to pERK assay.

### **Radioligand Binding**

All pharmacological methods followed the procedures as described in the literature (Klotz *et al.*, 1998). In brief, membranes for radioligand binding were prepared from CHO cells stably transfected with hAR subtypes in a two-step procedure. In the first step, cell fragments and nuclei were removed at 1000 x g and then the crude membrane fraction was sedimented from the supernatant at 100000 x g. The membrane pellet was resuspended in the buffer used for the respective binding experiments and it was frozen in liquid nitrogen and stored at -80°C. For radioligand binding at the A<sub>1</sub>R, 1 nM [<sup>3</sup>H]CCPA was used, for A<sub>2A</sub>R 10 nM [<sup>3</sup>H]NECA and for A<sub>3</sub>R 1 nM [<sup>3</sup>H]HEMADO. Non-specific binding of [<sup>3</sup>H]CCPA was determined in the presence of 1 mM theophylline and in the case of [<sup>3</sup>H]NECA and [<sup>3</sup>H]HEMADO 100 μM R-PIA was used. K<sub>i</sub> values from competition experiments were calculated using Prism (GraphPad Software, La Jolla, CA, U.S.A.) assuming competitive interaction with a single binding site. The curve fitting results (see Fig. 8 in Lagarias *et al.*, 2018) showed R<sup>2</sup> values ≥ 0.99 for all compounds and receptors, indicating that the used one-site competition model assuming a Hill slope of n=1 was appropriate.

### **NanoBRET ligand-binding**

Through the use of NanoBRET, real-time quantitative pharmacology of ligand-receptor interactions can be investigated in living cells. CA200645, acts as a fluorescent antagonist at both A<sub>1</sub>R and A<sub>3</sub>R with a slow off-rate (Stoddart *et al.*, 2012). Using an N-terminally NanoLuc (Nluc)-tagged A<sub>3</sub>R expressing cell line, competition binding assays were conducted. The kinetic data was fitted with the 'kinetic of competitive binding' model (Motulsky and Mahan, 1984; built into Prism) to determine affinity (pK<sub>i</sub>) values and the association rate constant (K<sub>on</sub>) and dissociation rates (K<sub>off</sub>) for unlabelled A<sub>3</sub>R antagonists. In several cases this model resulted in an ambiguous fit (Regression with Prism 8: "Ambiguous", 2019). We developed a new model which expands on the 'kinetic of competitive binding' model to accommodate very rapid competitor dissociation, assuming the unlabelled ligand rapidly equilibrates with the free receptor. This method allows determination of compound affinity (pK<sub>i</sub>) from the kinetic data.

In order to identify if the characterised compounds also bound the rat A<sub>3</sub>R, we conducted competition binding assays using Nluc-tagged rat A<sub>3</sub>R expressing HEK 293 cells and the fluorescent compound AV039 (Vernall *et al.*, 2012) rather than xanthine based CA200645, which have previously been reported as inactive at rat A<sub>3</sub>R (Siddiqi *et al.*, 1996). For both human and rat A<sub>3</sub>R experiments, filtered light emission at 450 nm and > 610 nm (640-685 nm band pass filter) was measured using a Mithras LB 940 and the raw BRET ratio calculated by dividing the 610 nm emission with the 450 nm emission. Here, Nluc on the N-terminus of A<sub>3</sub>R acted as the BRET donor (luciferase oxidizing its substrate) and CA200645/AV039 acted as the fluorescent acceptor. CA200645 was used at 25 nM, as previously reported (Stoddart *et al.*, 2015) and AV039 was used at 100 nM (pre-determined K<sub>D</sub>, 102 ± 7.59 nM). BRET was measured following the addition of the Nluc substrate, furimazine (0.1 μM). Nonspecific binding was determined using a high concentration of unlabelled antagonist, MRS 1220 at 10 nM or 10 μM, for human and rat A<sub>3</sub>R, respectively.

### Receptor binding kinetics data analysis

Specific binding of tracer vs time data was analysed using the Motulsky and Mahan method (Motulsky and Mahan, 1984; built into Prism) to determine the test compound association rate constant and dissociation rate constant. Data were fit to the "Kinetics of competitive binding" equation in Prism 8.0 (GraphPad Software Inc, San Diego, CA):

$$[RL]_t = \frac{N[L]k_1}{K_F - K_S} \left[ \frac{k_4(K_F - K_S)}{K_F K_S} - \frac{k_4 - K_S}{K_S} e^{-K_S t} + \frac{k_4 - K_F}{K_F} e^{-K_F t} \right]$$

where,

$$K_F = 0.5 \left\{ K_A + K_B + \sqrt{(K_A - K_B)^2 + 4[L][I]k_1 k_3} \right\}$$

$$K_S = 0.5 \left\{ K_A + K_B - \sqrt{(K_A - K_B)^2 + 4[L][I]k_1 k_3} \right\}$$

$$K_A = [L]k_1 + k_2$$

$$K_B = [I]k_3 + k_4$$

[RL]<sub>t</sub> is specific binding at time *t*, *N* the B<sub>max</sub>, [L] the tracer concentration, [I] the unlabelled competitor compound concentration, *k*<sub>1</sub> the tracer association rate constant, *k*<sub>2</sub> the tracer dissociation rate constant, *k*<sub>3</sub> the compound association rate constant and *k*<sub>4</sub> the compound dissociation rate constant.

Data were also analysed using an equation that assumes compound dissociation is too rapid for the dissociation rate constant to be determined reliably and the fits to the two equations compared (“Kinetics of competitive binding, rapid competitor dissociation”, derived in the Appendix I, Supplementary material). This equation assumes rapid equilibration between compound and receptor and consequently provides an estimate of the equilibrium binding affinity of the compound ( $K_i$ ) but not the binding kinetics of the compound. The equation is,

$$[RL]_t = \frac{N[L]k_1(1 - \rho_I)}{k_{obs,+I}} (1 - e^{-k_{obs,+I}t})$$

where  $\rho_I$  is fractional occupancy of receptors not bound by  $L$ :

$$\rho_I = \frac{[I]}{K_I + [I]}$$

and  $k_{obs,+I}$  is the observed association rate of tracer in the presence of competitor, defined as,

$$k_{obs,+I} = [L]k_1(1 - \rho_I) + k_2$$

The fits to the two equations were compared statistically using a partial F-test in Prism 8 (Motulsky, 2019).

### Pharmacokinetic assessments of K18

Preliminary pharmacokinetic assessments of K18 was out-sourced to Eurofins Panlabs (Missouri, U.S.A) and including tests for intrinsic clearance (human liver microsomes), plasma (human) stability and half-life in PBS. These tests were conducted in duplicate using a single concentration of K18 (0.1  $\mu$ M or 1  $\mu$ M) using the substrate depletion method. Here, the percentage of K18 remaining at various incubation times was detected using high-performance liquid chromatography mass spectrometry (HPLC-MS). Reference compounds ([verapamil](#), [terfenadine](#) and [propranolol](#)) were supplied and tested alongside K18. The half-life ( $t_{1/2}$ ) was estimated from the slope ( $k$ ) of percentage compound remaining ( $\ln(\%K18 \text{ remaining})$ ) versus time ( $t_{1/2} = -\ln(2)/k$ ), assuming first order kinetics. The intrinsic clearance ( $CL_{int}$ , in  $\mu$ l/min/mg) was calculated according to the following formula:

$$CL_{int} = \frac{0.693}{t_{1/2} * (mg \text{ protein}/\mu l)}$$

### Data and Statistical analysis

All *in vitro* assay data was analysed using Prism 8.0 (GraphPad software, San Diego, CA), with all dose-inhibition or response curves being fitted using a 3-parameter logistic equation to calculate response range or  $E_{max}$  and  $IC/EC_{50}$ . Experimental design ensured random distribution of treatments across 96/384-well plates to avoid systematic bias. Agonist stimulation alone was used as an intrinsic control across all experiments. Although initial screening of the 50 compounds was blinded, due to limitations in resources, it was not possible to perform all of our experiments in a blinded manner. Normalisation was used to control for unwanted sources of variation between experimental repeats.

In the rare cases where significant outliers were identified through the ROUT method (performed in Prism with Q set to 2% (defines the chance of falsely identifying one or more outliers)) (Statistics with Prism 7: “How to: Identify outliers”, 2019), these were excluded from data analysis and presentation. Dose-inhibition/dose-response curves were normalised to forskolin, expressed as percentage forskolin inhibition for G<sub>i</sub>-coupled A<sub>1</sub>R and A<sub>3</sub>R (1 µM or 10 µM, respectively) or stimulation for A<sub>2A</sub>R and A<sub>2B</sub>R (100 µM, representing the maximum cAMP accumulation of the system), relative to NECA/IB-MECA (agonist allowing comparison across AR subtypes and a selective A<sub>3</sub>R agonist, respectively). For cAMP experiments on A<sub>3</sub>R mutants, data was normalised to 100 µM forskolin, representing the maximum cAMP accumulation possible for each cell line. In the case of pERK1/2 response, normalisation was performed to PMA, a direct PKC activator providing the maximum pERK1/2 level of the system.

Schild analysis was performed to obtain pA<sub>2</sub> values (the negative logarithm to base 10 of the molar concentration of an antagonist that makes it necessary to double the concentration of the agonist to elicit the original submaximal response obtained by agonist alone (Schild, 1947)) for the potential antagonists. In cases where the Schild slope did not differ significantly from unity, the slope was constrained to unity giving an estimate of antagonist affinity (pK<sub>B</sub>). pA<sub>2</sub> and pK<sub>B</sub> coincide when the slope is exactly unity. Through performing Schild analysis, whereby the pA<sub>2</sub> is independent of agonist, we were able to experimentally determine the effect of receptor mutation on antagonist binding. The pA<sub>2</sub> values obtained through conducting Schild analysis of K18 at WT and mutant A<sub>3</sub>R were compared in order to indicate important residues involved in K18 binding. Whereas an increase in the pA<sub>2</sub> for a particular mutant when compared to WT suggested the antagonist was more potent, a decrease indicated a reduced potency.

All experiments were conducted in duplicate (technical replicates) to ensure the reliability of single values. The data and statistical analysis comply with the recommendations on experimental design and analysis in pharmacology (Curtis *et al.*, 2018). Statistical analysis, performed using Prism 8.0, was undertaken for experiments where the group size was at least n = 5 and these independent values used to calculate statistical significance (\*, p < 0.05; \*\*, p < 0.01; \*\*\*, p < 0.001; \*\*\*\*, p < 0.0001) using a one-way ANOVA with a Dunnett's post-test for multiple comparisons or Students' t-test, as appropriate. Any experiments conducted n < 5 should be considered preliminary. Compounds taken forward for further investigation after our preliminary screening (n = 3) were selected based on a high mean cAMP accumulation (>80%).

## Computational biochemistry

### MD simulations

Preparation of the complexes between human A<sub>3</sub>R with K5, K17, K18 or MRS 1220 and rat A<sub>3</sub>R with K18 or K25 was based on a homology model of A<sub>2A</sub>R (see Appendix II in Supplementary material). Each ligand-protein complex was embedded in hydrated POPE bilayers. A simulation box of the protein-ligand complexes in POPE lipids, water and ions was built using the System Builder utility of Desmond (Desmond Molecular Dynamics System, version 3.0; D.E. Shaw Res. New York, 2011; Maest. Interoperability Tools, 3.1; Schrodinger Res. New York, 2012.). A buffered orthorhombic system in 10 Å distance from the solute atoms with periodic boundary conditions was constructed for all the complexes. The MD



simulations were performed with Amber14 and each complex-bilayer system was processed by the LEaP module in AmberTools14 under the AMBER14 software package (Case *et al.*, 2014). Amber ff14SB force field parameters (Maier *et al.*, 2015) were applied to the protein, lipid14 to the lipids (Dickson *et al.*, 2014), GAFF to the ligands (Wang *et al.*, 2004) and TIP3P (Jorgensen *et al.*, 1983) to the water molecules for the calculation of bonded, vdW parameters and electrostatic interactions. Atomic charges were computed according to the RESP procedure (Bayly *et al.*, 1993) using Gaussian03 (Frisch *et al.*, 2003) and antechamber of AmberTools14 (Case *et al.*, 2014). The temperature of 310 K was used in MD simulations in order to ensure that the membrane state is above the main phase transition temperature of 298 K for POPE bilayers (Koynova and Caffrey, 1998). In the production phase, the relaxed systems were simulated in the NPT ensemble conditions for 100 ns. The visualization of produced trajectories and structures was performed using the programs Chimera (Pettersen *et al.*, 2004) and VMD (Humphrey *et al.*, 1996). All the MD simulations were run on GTX 1060 GPUs in lab workstations or on the ARIS Supercomputer.

### MM-PBSA calculations

Relative binding free energies of the complexes between K5, K17, K18, MRS 1220 and A<sub>3</sub>R was estimated by the 1-trajectory MM-PBSA approach (Massova and Kollman, 2000). Effective binding energies ( $\Delta G_{\text{eff}}$ ) were computed considering the gas phase energy and solvation free energy contributions to binding. For this, structural ensembles were extracted in intervals of 50 ps from the last 50 ns of the production simulations for each complex. Prior to the calculations all water molecules, ions, and lipids were removed, and the structures were positioned such that the geometric centre of each complex was located at the coordinate origin. The polar part of the solvation free energy was determined by calculations using Poisson-Boltzmann (PB) calculations (Homeyer and Gohike, 2013). In these calculations, a dielectric constant of  $\epsilon_{\text{solute}} = 1$  was assigned to the binding area and  $\epsilon_{\text{solute}} = 80$  for water. Using an implicit solvent representation for the calculation of the effective binding energy is an approximation to reduce the computational cost of the calculations. The binding free energy for each complex was calculated using equation (1)

$$\Delta G_{\text{eff}} = \Delta E_{\text{MM}} + \Delta G_{\text{sol}} \quad (1)$$

In equation (1)  $\Delta G_{\text{eff}}$  is the binding free energy for each calculated complex neglecting the effect of entropic contributions or assuming to be similar for the complexes studied.  $\Delta E_{\text{MM}}$  defines the interaction energy between the complex, the protein and the ligand as calculated by molecular mechanics in the gas phase.  $\Delta G_{\text{sol}}$  is the desolvation free energy for transferring the ligand from water in the binding area calculated using the PBSA model. The terms for each complex  $\Delta E_{\text{MM}}$  and  $\Delta G_{\text{sol}}$  are calculated using equations (2) and (3)

$$\Delta E_{\text{MM}} = \Delta E_{\text{elec}} + \Delta E_{\text{vdW}} \quad (2)$$

$$\Delta G_{\text{sol}} = \Delta G_{\text{P}} + \Delta G_{\text{NP}} \quad (3)$$

In equation (2)  $\Delta E_{\text{elec}}$  and  $\Delta E_{\text{vdW}}$  are the electrostatic and the vdW interaction energies, respectively. In equation (3)  $\Delta G_{\text{P}}$  is the electrostatic or polar contribution to free energy of solvation and the term  $\Delta G_{\text{NP}}$  is the non-polar or hydrophobic contribution to solvation free energy. Molecular mechanics energies and the non-polar contribution to the solvation free energy were calculated with the *mmpbsa.pl* module (Miller *et al.*, 2012) of Amber14 (Case *et al.*, 2014).

### Nomenclature of Targets and Ligands

Key protein targets and ligands in this article are hyperlinked to corresponding entries in <http://www.guidetopharmacology.org>, the common portal for data from the IUPHAR/BPS

Guide to PHARMACOLOGY (Harding *et al.*, 2018), and are permanently archived in the Concise Guide to PHARMACOLOGY 2017/18 (Alexander *et al.*, 2017).

## REFERENCES

- Alexander, S. P., Kelly, E., Marrion, N. V., Peters, J. A., Faccenda, E., Harding, S. D., *et al.* (2017). THE CONCISE GUIDE TO PHARMACOLOGY 2017/18: Overview. *British Journal of Pharmacology*, **174**(S1), S1–S16. DOI: 10.1111/bph.13882
- Areias, F., Correia, C., Rocha, A., Brea, J., Castro, M., Loza, M. I., *et al.* (2019). 2- Aryladenine derivatives as a potent scaffold for A1, A3 and dual A1/A3 adenosine receptor antagonists: Synthesis and structure-activity relationships. *Bioorganic & Medicinal Chemistry*, **27**(16), 3551–3558. DOI: 10.1016/j.bmc.2019.06.034
- Arruda, M. A., Stoddart, L. A., Gherbi, K., Briddon, S. J., Kellam, B., & Hill, S. J. (2017). A Non-imaging High Throughput Approach to Chemical Library Screening at the Unmodified Adenosine-A3 Receptor in Living Cells. *Frontiers in Pharmacology*, **8**, 908. DOI: 10.3389/fphar.2017.00908
- Bayly, C. I., Cieplak, P., Cornell, W. D., & Kollman, P. A. (1993). A Well-Behaved Electrostatic Potential Based Method Using Charge Restraints for Deriving Atomic Charges - the Resp Model. *Journal of Physical Chemistry*, **97**(40), 10269–10280. DOI: 10.1021/j100142a004
- Bouzo-Lorenzo, M., Stoddart, L. A., Xia, L., Ijzerman, A. P., Heitman, L. H., Briddon, S. J., & Hill, S. J. (2019). A live cell NanoBRET binding assay allows the study of ligand-binding kinetics to the adenosine A3 receptor. *Purinergic Signalling*, **15**(2), 139–153. <http://doi.org/10.1007/s11302-019-09650-9>
- Brown, R. A., Clarke, G. W., Ledbetter, C. L., Hurle, M. J., Denyer, J. C., Simcock, D. E., *et al.* (2008). Elevated expression of adenosine A1 receptor in bronchial biopsy specimens from asthmatic subjects. *The European Respiratory Journal*, **31**(2), 311–319. DOI: 10.1183/09031936.00003707
- Carlsson, J., Yoo, L., Gao, Z.-G., Irwin, J. J., Shoichet, B. K., & Jacobson, K. A. (2010). Structure-based discovery of A2A adenosine receptor ligands. *Journal of Medicinal Chemistry*, **53**(9), 3748–3755. DOI: 10.1021/jm100240h
- Carpenter, B., Nehmé, R., Warne, T., Leslie, A. G. W., & Tate, C. G. (2016). Structure of the adenosine A(2A) receptor bound to an engineered G protein. *Nature*, **536**(7614), 104–107. DOI: 10.1038/nature18966
- Case, D. A., Babin, V., Berryman, J. T., Betz, R. M., Cai, Q., Cerutti, D. S., & Kollman, P. A. (2014). AMBER 14. University of California, San Francisco.
- Chen, J.-F., Eltzhig, H. K., & Fredholm, B. B. (2013). Adenosine receptors as drug targets - what are the challenges? *Nature Reviews. Drug Discovery*, **12**(4), 265–286. DOI: 10.1038/nrd3955
- Cheng, R. K. Y., Segala, E., Robertson, N., Deflorian, F., Dore, A. S., Errey, J. C., *et al.* (2017). Structures of Human A1 and A2A Adenosine Receptors with Xanthines Reveal Determinants of Selectivity. *Structure (London, England : 1993)*, **25**(8), 1275–1285.e4. DOI: 10.1016/j.str.2017.06.012
- Cheng, Y., & Prusoff, W. H. (1973). Relationship between the inhibition constant (K1) and the concentration of inhibitor which causes 50 per cent inhibition (I50) of an enzymatic reaction. *Biochemical Pharmacology*, **22**(23), 3099–3108.
- Curtis, M. J., Alexander, S., Cirino, G., Docherty, J. R., George, C. H., Giembycz, M. A., *et al.* (2018). Experimental design and analysis and their reporting II: updated and simplified guidance for authors and peer reviewers. *British Journal of Pharmacology*, **175**(7), 987–993. DOI: 10.1111/bph.14153
- Dickson, C. J., Madej, B. D., Skjevik, A. A., Betz, R. M., Teigen, K., Gould, I. R., & Walker, R. C. (2014). Lipid14: The Amber Lipid Force Field. *Journal of Chemical Theory and Computation*, **10**(2), 865–879. DOI: 10.1021/ct4010307
- Dore, A. S., Robertson, N., Errey, J. C., Ng, I., Hollenstein, K., Tehan, B., *et al.* (2011). Structure of the adenosine A(2A) receptor in complex with ZM241385 and the xanthines XAC

- and caffeine. *Structure (London, England : 1993)*, **19**(9), 1283–1293. DOI: 10.1016/j.str.2011.06.014
- Draper-Joyce, C. J., Khoshouei, M., Thal, D. M., Liang, Y.-L., Nguyen, A. T. N., Furness, S. G. B., et al. (2018). Structure of the adenosine-bound human adenosine A1 receptor-Gi complex. *Nature*, **558**(7711), 559–563. DOI: 10.1038/s41586-018-0236-6
- Fredholm, B. B., Ijzerman, A. P., Jacobson, K. A., Linden, J., & Mueller, C. E. (2011). International Union of Basic and Clinical Pharmacology. LXXXI. Nomenclature and Classification of Adenosine Receptors-An Update. *Pharmacological Reviews*, **63**(1), 1–34. DOI: 10.1124/pr.110.003285
- Frisch, M. J., Trucks, G. W., Schlegel, H. B., Scuseria, G. E., Rob, M. A., & Pople, J. A. (2003). *Gaussian 03*. Wallingford, CT.
- Gao, Z.-G., Chen, A., Barak, D., Kim, S.-K., Müller, C. E., & Jacobson, K. A. (2002). Identification by site-directed mutagenesis of residues involved in ligand recognition and activation of the human A3 adenosine receptor. *The Journal of Biological Chemistry*, **277**(21), 19056–19063. DOI: 10.1074/jbc.M110960200
- Gessi, S., Merighi, S., Varani, K., Leung, E., Mac Lennan, S., & Borea, P. A. (2008). The A3 adenosine receptor: an enigmatic player in cell biology. *Pharmacology & Therapeutics*, **117**(1), 123–140. DOI: 10.1016/j.pharmthera.2007.09.002
- Giraldo, J., Serra, J., Roche, D., & Rovira, X. (2007). Assessing receptor affinity for inverse agonists: Schild and Cheng-Prusoff methods revisited. *Current Drug Targets*, **8**(1), 197–202.
- Glukhova, A., Thal, D. M., Nguyen, A. T., Vecchio, E. A., Jörg, M., Scammells, P. J., et al. (2017). Structure of the Adenosine A1 Receptor Reveals the Basis for Subtype Selectivity. *Cell*, **168**(5), 867–877.e13. DOI: 10.1016/j.cell.2017.01.042
- Graham, S., Combes, P., Crumiere, M., Klotz, K. N., & Dickenson, J. M. (2001). Regulation of p42/p44 mitogen-activated protein kinase by the human adenosine A(3) receptor in transfected CHO cells. *European Journal of Pharmacology*, **420**(1), 19–26.
- Haeusler, D., Grassinger, L., Fuchshuber, F., Hoerleinsberger, W. J., Hoffberger, R., Leisser, I., et al. (2015). Hide and seek: a comparative autoradiographic in vitro investigation of the adenosine A3 receptor. *European Journal of Nuclear Medicine and Molecular Imaging*, **42**(6), 928–939. DOI: 10.1007/s00259-014-2985-2
- Harding, S. D., Sharman, J. L., Faccenda, E., Southan, C., Pawson, A. J., Ireland, S., et al. (2018). The IUPHAR/BPS Guide to PHARMACOLOGY in 2018: updates and expansion to encompass the new guide to IMMUNOPHARMACOLOGY. *Nucleic Acids Research*, **46**(D1), D1091–D1106. DOI: 10.1093/nar/gkx1121
- Homeyer, N., & Gohlke, H. (2013). FEW: A workflow tool for free energy calculations of ligand binding. *Journal of Computational Chemistry*, **34**(11), 965–973. DOI: 10.1002/jcc.23218
- Humphrey, W., Dalke, A., & Schulten, K. (1996). VMD: Visual molecular dynamics. *Journal of Molecular Graphics & Modelling*, **14**(1), 33–38. DOI: 10.1016/0263-7855(96)00018-5
- Jaakola, V.-P., Griffith, M. T., Hanson, M. A., Cherezov, V., Chien, E. Y. T., Lane, J. R., et al. (2008). The 2.6 angstrom crystal structure of a human A2A adenosine receptor bound to an antagonist. *Science (New York, N. Y.)*, **322**(5905), 1211–1217. DOI: 10.1126/science.1164772
- Jacobson, K. A., Park, K. S., Jiang, J. L., Kim, Y. C., Olah, M. E., Stiles, G. L., & Ji, X. D. (1997). Pharmacological characterization of novel A3 adenosine receptor-selective antagonists. *Neuropharmacology*, **36**(9), 1157–1165. [http://doi.org/10.1016/s0028-3908\(97\)00104-4](http://doi.org/10.1016/s0028-3908(97)00104-4)
- Jorgensen, W. L., Chandrasekhar, J., Madura, J. D., Impey, R. W., & Klein, M. L. (1983a). Comparison of Simple Potential Functions for Simulating Liquid Water. *Journal of Chemical Physics*, **79**(2), 926–935. DOI: 10.1063/1.445869
- Katritch, V., Jaakola, V.-P., Lane, J. R., Lin, J., Ijzerman, A. P., Yeager, M., et al. (2010). Structure-Based Discovery of Novel Chemotypes for Adenosine A(2A) Receptor Antagonists. *Journal of Medicinal Chemistry*, **53**(4), 1799–1809. DOI: 10.1021/jm901647p
- Klotz, K. N., Hessling, J., Hegler, J., Owman, C., Kull, B., Fredholm, B. B., & Lohse, M. J. (1998). Comparative pharmacology of human adenosine receptor subtypes -characterization of stably transfected receptors in CHO cells. *Naunyn-Schmiedeberg's Archives of Pharmacology*, **357**(1), 1–9.

- Knight, A., Hemmings, J. L., Winfield, I., Leuenberger, M., Frattini, E., Frenguelli, B. G., et al. (2016). Discovery of Novel Adenosine Receptor Agonists That Exhibit Subtype Selectivity. *Journal of Medicinal Chemistry*, **59**(3), 947–964. DOI: 10.1021/acs.jmedchem.5b01402
- Kolb, P., Phan, K., Gao, Z.-G., Marko, A. C., Sali, A., & Jacobson, K. A. (2012). Limits of Ligand Selectivity from Docking to Models: In Silico Screening for A(1) Adenosine Receptor Antagonists. *PLoS ONE*, **7**(11). DOI: 10.1371/journal.pone.0049910
- Koynova, R., & Caffrey, M. (1998a). Phases and phase transitions of the phosphatidylcholines. *Biochimica Et Biophysica Acta-Reviews on Biomembranes*, **1376**(1), 91–145. DOI: 10.1016/S0304-4157(98)00006-9
- Lagarias, P., Vrontaki, E., Lambrinidis, G., Stamatis, D., Convertino, M., Ortore, G., et al. (2018). Discovery of Novel Adenosine Receptor Antagonists through a Combined Structure- and Ligand-Based Approach Followed by Molecular Dynamics Investigation of Ligand Binding Mode. *Journal of Chemical Information and Modeling*, **58**(4), 794–815. DOI: 10.1021/acs.jcim.7b00455
- Lebon, G., Edwards, P. C., Leslie, A. G. W., & Tate, C. G. (2015). Molecular Determinants of CGS21680 Binding to the Human Adenosine A2A Receptor. *Molecular Pharmacology*, **87**(6), 907–915. DOI: 10.1124/mol.114.097360
- Lebon, G., Warne, T., Edwards, P. C., Bennett, K., Langmead, C. J., Leslie, A. G. W., & Tate, C. G. (2011). Agonist-bound adenosine A2A receptor structures reveal common features of GPCR activation. *Nature*, **474**(7352), 521–525. DOI: 10.1038/nature10136
- Lenselink, E. B., Beuming, T., van Veen, C., Massink, A., Sherman, W., van Vlijmen, H. W. T., & Ijzerman, A. P. (2016). In search of novel ligands using a structure-based approach: a case study on the adenosine A2A receptor. *Journal of Computer-Aided Molecular Design*, **30**(10), 863–874. DOI: 10.1007/s10822-016-9963-7
- Liu, W., Chun, E., Thompson, A. A., Chubukov, P., Xu, F., Katritch, V., et al. (2012). Structural basis for allosteric regulation of GPCRs by sodium ions. *Science (New York, N. Y.)*, **337**(6091), 232–236. DOI: 10.1126/science.1219218
- Maier, J. A., Martinez, C., Kasavajhala, K., Wickstrom, L., Hauser, K. E., & Simmerling, C. (2015). ff14SB: Improving the Accuracy of Protein Side Chain and Backbone Parameters from ff99SB. *Journal of Chemical Theory and Computation*, **11**(8), 3696–3713. DOI: 10.1021/acs.jctc.5b00255
- Massova, I., & Kollman, P. A. (2000). Combined molecular mechanical and continuum solvent approach (MM-PBSA/GBSA) to predict ligand binding. *Perspectives in Drug Discovery and Design*, **18**(1), 113–135. DOI: 10.1023/A:1008763014207
- May, L. T., Bridge, L. J., Stoddart, L. A., Briddon, S. J., & Hill, S. J. (2011). Allosteric interactions across native adenosine-A3 receptor homodimers: quantification using single- cell ligand-binding kinetics. *FASEB Journal : Official Publication of the Federation of American Societies for Experimental Biology*, **25**(10), 3465–3476. DOI: 10.1096/fj.11-186296
- Meng, X.-Y., Zhang, H.-X., Mezei, M., & Cui, M. (2011). Molecular Docking: A Powerful Approach for Structure-Based Drug Discovery. *Current Computer-Aided Drug Design*, **7**(2), 146–157.
- Miller, B. R. I., McGee, T. D. J., Swails, J. M., Homeyer, N., Gohlke, H., & Roitberg, A. E. (2012). MMPBSA.py: An Efficient Program for End-State Free Energy Calculations. *Journal of Chemical Theory and Computation*, **8**(9), 3314–3321. DOI: 10.1021/ct300418h
- Miwatashi, S., Arikawa, Y., Matsumoto, T., Uga, K., Kanzaki, N., Imai, Y. N., & Ohkawa, S. (2008). Synthesis and biological activities of 4-phenyl-5-pyridyl-1,3-thiazole derivatives as selective adenosine A3 antagonists. *Chemical & Pharmaceutical Bulletin*, **56**(8), 1126–1137.
- Motulsky, H. J. (n.d.). Interpreting the extra sum-of squares F test. Retrieved May 30, 2019, from Motulsky, H. J., & Mahan, L. C. (1984). The Kinetics of Competitive Radioligand Binding Predicted by the Law of Mass-Action. *Molecular Pharmacology*, **25**(1), 1–9.
- Okamura, T., Kurogi, Y., Hashimoto, K., Sato, S., Nishikawa, H., Kiryu, K., & Nagao, Y. (2004). Structure-activity relationships of adenosine A3 receptor ligands: new potential therapy for the treatment of glaucoma. *Bioorganic & Medicinal Chemistry Letters*, **14**(14), 3775–3779. DOI: 10.1016/j.bmcl.2004.04.099

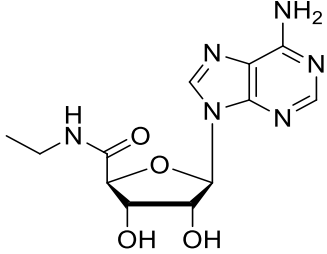
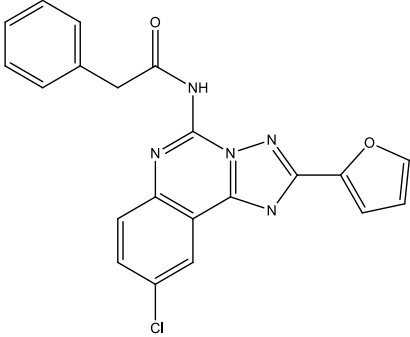
- Pettersen, E. F., Goddard, T. D., Huang, C. C., Couch, G. S., Greenblatt, D. M., Meng, E. C., & Ferrin, T. E. (2004). UCSF chimera - A visualization system for exploratory research and analysis. *Journal of Computational Chemistry*, **25**(13), 1605–1612. DOI: 10.1002/jcc.20084
- Schild, H. O. (1947). pA, a new scale for the measurement of drug antagonism. *British Journal of Pharmacology and Chemotherapy*, **2**(3), 189–206.
- Schulte, G., & Fredholm, B. B. (2002). Signaling pathway from the human adenosine A<sub>3</sub> receptor expressed in Chinese hamster ovary cells to the extracellular signal-regulated kinase 1/2. *Molecular Pharmacology*, **62**(5), 1137–1146.
- Sexton, P. M., & Christopoulos, A. (2018). To Bind or Not to Bind: Unravelling GPCR Polypharmacology. *Cell*, **172**(4), 636–638. DOI: 10.1016/j.cell.2018.01.018
- Siddiqi, S. M., Ji, X.-D., Melman, N., Olah, M. E., Jain, R., Evans, P., et al. (1996). Survey of Nonxanthine Derivatives as Adenosine Receptor Ligands. *Nucleosides & Nucleotides*, **15**(1-3), 693–717. <http://doi.org/10.1080/07328319608002416>
- Stamatis, D., Lagarias, P., Kerry, Kerry, Vrontaki, E., Ladds, G., & Kolocouris, A. (2019). Structural Characterization of Agonist Binding to an A<sub>3</sub> Adenosine Receptor through Biomolecular Simulations and Mutagenesis Experiments. *Journal of Medicinal Chemistry*, **62**(19), 8831–8846. DOI: 10.1021/acs.jmedchem.9b01164
- Stoddart, L. A., Johnstone, E. K. M., Wheal, A. J., Goulding, J., Robers, M. B., Machleidt, T., et al. (2015). Application of BRET to monitor ligand binding to GPCRs. *Nature Methods*, **12**(7), 661–. DOI: 10.1038/NMETH.3398
- Stoddart, L. A., Kilpatrick, L. E., & Hill, S. J. (2018). NanoBRET Approaches to Study Ligand Binding to GPCRs and RTKs. *Trends in Pharmacological Sciences*, **39**(2), 136–147. DOI: 10.1016/j.tips.2017.10.006
- Soave, M., Briddon, S. J., Hill, S. J., & Stoddart, L. A. (2019). Fluorescent ligands: Bringing light to emerging G protein-coupled receptor paradigms. *British Journal of Pharmacology*, DOI: 10.1111/bph.14953
- Stoddart, L. A., Vernall, A. J., Denman, J. L., Briddon, S. J., Kellam, B., & Hill, S. J. (2012). Fragment screening at adenosine-A<sub>3</sub> receptors in living cells using a fluorescence-based binding assay. *Chemistry & Biology*, **19**(9), 1105–1115. DOI: 10.1016/j.chembiol.2012.07.014
- Sykes, D. A., Stoddart, L. A., Kilpatrick, L. E., & Hill, S. J. (2019). Binding kinetics of ligands acting at GPCRs. *Molecular and Cellular Endocrinology*, **485**, 9–19. DOI: 10.1016/j.mce.2019.01.018
- Tunçer, S., Gurbanov, R., Sheraj, I., Solel, E., Esenturk, O., & Banerjee, S. (2018). Low dose dimethyl sulfoxide driven gross molecular changes have the potential to interfere with various cellular processes. *Scientific Reports*, **8**(1), 14828. DOI: 10.1038/s41598-018-33234-z
- Vernall, A. J., Stoddart, L. A., Briddon, S. J., Hill, S. J., & Kellam, B. (2012). Highly potent and selective fluorescent antagonists of the human adenosine A<sub>3</sub> receptor based on the 1,2,4-triazolo[4,3-a]quinoxalin-1-one scaffold. *Journal of Medicinal Chemistry*, **55**(4), 1771–1782. <http://doi.org/10.1021/jm201722y>
- Wang, J. M., Wolf, R. M., Caldwell, J. W., Kollman, P. A., & Case, D. A. (2004). Development and testing of a general amber force field. *Journal of Computational Chemistry*, **25**(9), 1157–1174. DOI: 10.1002/jcc.20035
- Xu, F., Wu, H., Katritch, V., Han, G. W., Jacobson, K. A., Gao, Z.-G., et al. (2011). Structure of an agonist-bound human A<sub>2A</sub> adenosine receptor. *Science (New York, N.Y.)*, **332**(6027), 322–327. DOI: 10.1126/science.1202793
- Yaziji, V., Rodríguez, D., Coelho, A., García-Mera, X., Maatougui, El, A., Brea, J., et al. (2013). Selective and potent adenosine A<sub>3</sub> receptor antagonists by methoxyaryl substitution on the N-(2,6-diarylpyrimidin-4-yl)acetamide scaffold. *European Journal of Medicinal Chemistry*, **59**, 235–242. DOI: 10.1016/j.ejmech.2012.11.010
- Yaziji, V., Rodríguez, D., Gutiérrez-de-Terán, H., Coelho, A., Caamaño, O., García-Mera, X., et al. (2011). Pyrimidine derivatives as potent and selective A<sub>3</sub> adenosine receptor antagonists. *Journal of Medicinal Chemistry*, **54**(2), 457–471. DOI: 10.1021/jm100843z
- Zhang, G., Liu, Y., Ruoho, A. E., & Hurley, J. H. (1997). Structure of the adenylyl cyclase catalytic core. *Nature*, **386**(6622), 247–253. DOI: 10.1038/386247a0

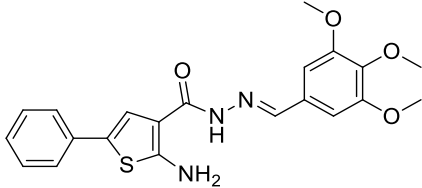
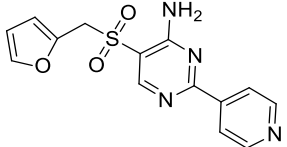
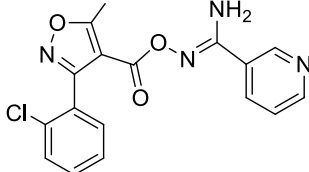
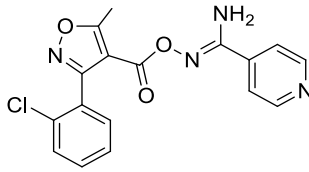
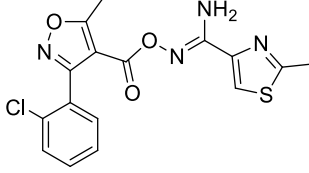
Regression with Prism 8: 'Ambiguous'. (2019).  
[https://www.graphpad.com/guides/prism/8/curve-fitting/reg\\_analysischeck\\_nonlin\\_ambiguous.htm](https://www.graphpad.com/guides/prism/8/curve-fitting/reg_analysischeck_nonlin_ambiguous.htm)  
Statistics with Prism 7: 'How to: Identify outliers'. (2019).

### **Acknowledgments**

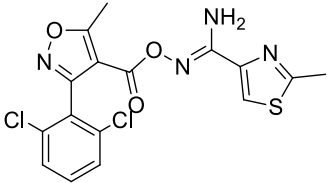
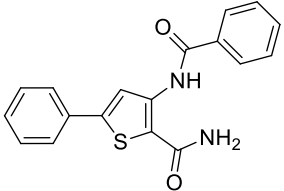
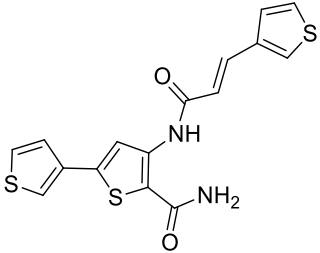
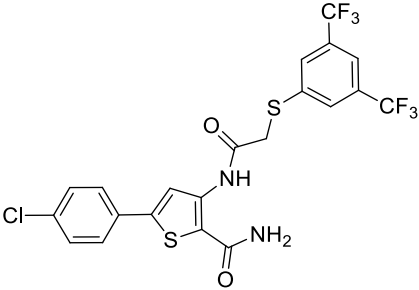
We gratefully acknowledge the support of the Leverhulme Trust (RPG-2017-255) (KB and GL) and the BBSRC (BB/M00015X/2) (GL). This research represents part of the Ph.D work of P.L. We thank Chiesi Hellas which supported this research (SARG No 10354) and the State Scholarships Foundation (IKY) for providing a Ph.D fellowship to P.L. (MIS 5000432, NSRF 2014-2020). The work of E.V. is implemented through IKY scholarships programme and co-financed by the European Union (European Social Fund - ESF) and Greek national funds through the action entitled "Reinforcement of Postdoctoral Researchers", in the framework of the Operational Program "Human Resources Development Program, Education and Lifelong Learning" of the National Strategic Reference Framework (NSRF) 2014 – 2020. This work was supported by computational time granted from the Greek Research & Technology Network (GRNET) in the National HPC facility - ARIS - under project IDs pr005010. We would like to thank Stephen Hill, Stephen Briddon and Mark Soave (University of Nottingham) for gifting the Nluc-A<sub>3</sub>R cell line, Nluc-rat A<sub>3</sub>R construct, the fluorescent antagonist AV039 and their technical advice. We are also grateful to Sonja Kachler for her technical assistance.

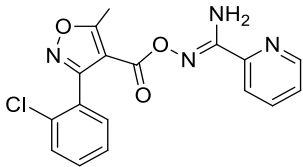
**Table 1. Mean cAMP accumulation as measured in Flp-In CHO cells stably expressing A<sub>3</sub>R following stimulation with 10 μM forskolin only (DMSO) or 10 μM forskolin, NECA at the predetermined IC<sub>80</sub> concentration and 1 μM test compound/MRS 1220/DMSO control. Binding affinities were obtained through radioligand binding assays against the A<sub>1</sub>R, A<sub>2A</sub>R and A<sub>3</sub>R.**

Compound	Compound name	Chemical structure	cAMP accumulation		Radioligand binding (K <sub>i</sub> (μM)) <sup>c</sup>		
			Mean <sup>a</sup>	Mean difference <sup>b</sup>	A <sub>3</sub> R	A <sub>1</sub> R	A <sub>2A</sub> R
	NECA		60.32 ±3.41	-	ND	ND	ND
	DMSO	CH <sub>3</sub> -SO-CH <sub>3</sub>	100.00 ±1.15	-39.68	ND	ND	ND
	MRS 1220		111.30 ±1.65	-50.95	ND	ND	ND

<b>K1</b>	HTS12884SC <sup>1</sup>		84.81 ±4.90	-24.49	<b>3.10</b>	>100	<b>2.67</b>
<b>K8</b>	KM03338 <sup>1</sup>		51.56 ±5.80	8.757	>100	>100	>100
<b>K10</b>	STK300529 <sup>1</sup>		84.91 ±5.37	-24.59	<b>4.49</b>	>60	>60
<b>K11</b>	SKT323144 <sup>1</sup>		80.78 ±4.77	-20.46	<b>5.15</b>	>60	30
<b>K17</b>	SPB02734 <sup>1</sup>		82.41 ±7.55	-22.09	<b>4.16</b>	>30	>60



<b>K18</b>	SPB02735 <sup>1</sup>		102.6 ±2.13	-42.27	<b>0.89</b>	>100	>100
<b>K20</b>	GK03725 <sup>1</sup>		97.86 ±2.60	-37.54	<b>0.91</b>	<b>1.09</b>	<b>7.29</b>
<b>K23</b>	GK01176 <sup>1</sup>		88.02 ±1.70	-27.70	<b>1.65</b>	<b>1.18</b>	<b>4.69</b>
<b>K25</b>	GK01513 <sup>1</sup>		88.66 ±5.36	-28.34	<b>1.55</b>	>100	>100

<b>K32</b>	STK323544		83.39 ±5.27	-23.07	<b>2.40</b>	>100	>100
------------	-----------	---	-------------	--------	-------------	------	------

<sup>1</sup>Indicates previously published in Lagarias *et al.*, 2018

<sup>a</sup>cAMP accumulation mean ± SEM expressed as %10 μM forskolin response where  $n = 3$  independent experimental repeats, conducted in duplicate. Potential antagonists were selected for further investigation based on a high mean cAMP accumulation (>80%).

<sup>b</sup>Difference between the mean cAMP accumulation between 'NECA' and each compound expressed as %10 μM forskolin response

<sup>c</sup>Binding affinity measured in three independent experiments and where indicated, previously published in Lagarias *et al.*, 2018. Bold denotes binding affinity < 10 μM.

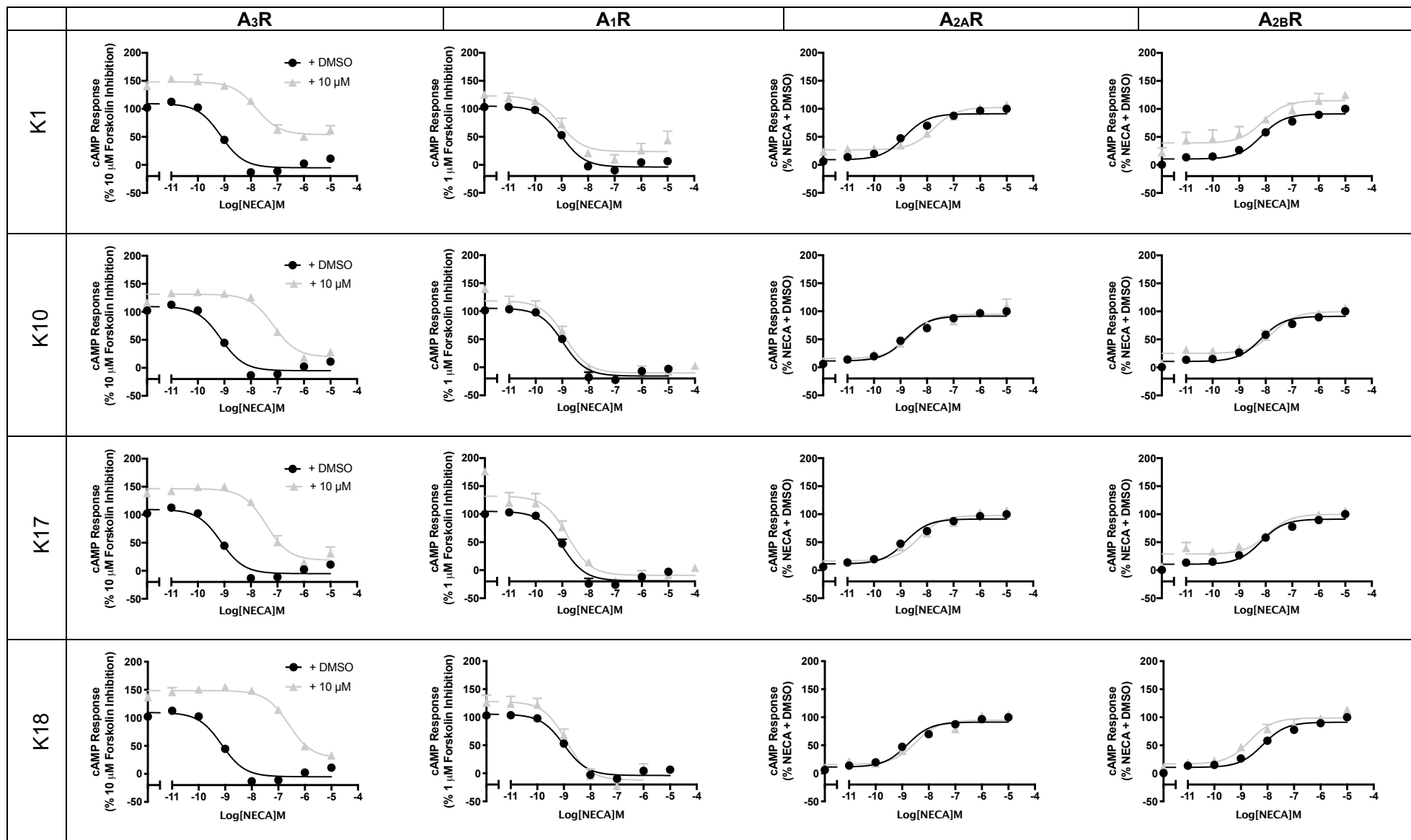




**Figure 1. Characterisation of A<sub>3</sub>R antagonist at all AR subtypes.** A<sub>3</sub>R Flp-In CHO cells or CHO-K1 cells (2000 cells/well) stably expressing one of the remaining AR subtypes were exposed to forskolin in the case of G<sub>i</sub>-coupled A<sub>1</sub>R and A<sub>3</sub>R (1 μM or 10 μM, respectively) or DMSO control in the case of G<sub>s</sub>-coupled A<sub>2A</sub>R and A<sub>2B</sub>R, NECA and test compound (10 μM) for 30 min and cAMP accumulation detected. All values are mean ± SEM expressed as percentage forskolin inhibition (A<sub>1</sub>R and A<sub>3</sub>R) or stimulation (A<sub>2A</sub>R and A<sub>2B</sub>R), relative to NECA. *n* ≥ 3 independent experimental repeats, conducted in duplicate.

**Table 2. Potency of NECA stimulated cAMP inhibition or accumulation as determined in Flp-In CHO or CHO-K1 cells expressing one of four ARs subtype (A<sub>3</sub>R, A<sub>1</sub>R, A<sub>2A</sub>R or A<sub>2B</sub>R).** Cells stably expressing A<sub>3</sub>R, A<sub>1</sub>R, A<sub>2A</sub>R or A<sub>2B</sub>R were stimulated with 10 μM forskolin (in the case of A<sub>3</sub>R and A<sub>1</sub>R), 10 μM tested compound/DMSO and increasing concentrations of NECA.

	pIC <sub>50</sub> /pEC <sub>50</sub> <sup>a</sup>			
	A <sub>3</sub> R	A <sub>1</sub> R	A <sub>2A</sub> R	A <sub>2B</sub> R
<b>NECA only</b>	9.24 ±0.1	8.98 ±0.1	7.88 ±0.1	7.24 ±0.2
<b>K1</b>	8.01 ±0.2****	8.97 ±0.1	7.12 ±0.1****	7.23 ±0.2
<b>K10</b>	7.74 ±0.2****	8.82 ±0.1	7.84 ±0.1	7.19 ±0.2
<b>K17</b>	7.59 ±0.1****	8.68 ±0.1	7.76 ±0.1	7.15 ±0.2
<b>K18</b>	6.70 ±0.1****	8.85 ±0.1	7.75 ±0.1	7.10 ±0.2
<b>K20</b>	7.12 ±0.2****	7.43 ±0.1 ****	7.12 ±0.1****	7.08 ±0.1
<b>K23</b>	7.72 ±0.1****	7.38 ±0.1 ****	7.26 ±0.1**	7.04 ±0.2
<b>K25</b>	7.64 ±0.1****	9.00 ±0.1	7.98 ±0.1	7.22 ±0.2
<b>K32</b>	7.56 ±0.1****	8.85 ±0.1	7.80 ±0.1	7.14 ±0.2

<sup>a</sup>Negative logarithm of NECA concentration required to produce a half-maximal response in the absence (NECA only) or presence of 10 μM compound at each AR subtype

Data are expressed as mean ± SEM obtained in *n* = 5 independent experimental repeats, conducted in duplicate. Statistical significance (\*, *p* < 0.05; \*\*, *p* < 0.01; \*\*\*, *p* < 0.001; \*\*\*\*, *p* < 0.0001) compared to 'NECA only' was determined by one-way ANOVA with Dunnett's post-test.

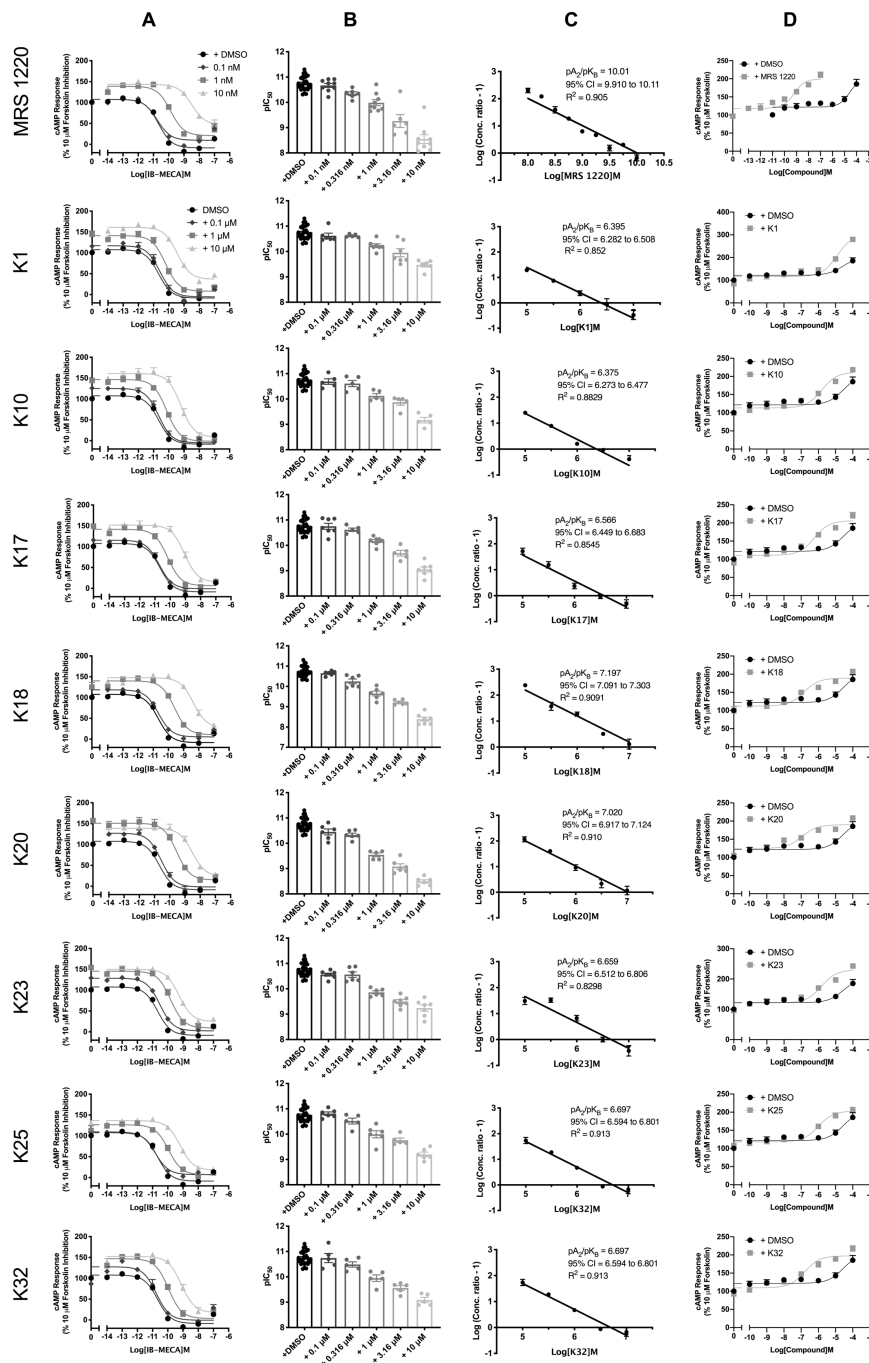


**Figure 2. IB-MECA stimulated cAMP inhibition at WT A<sub>3</sub>R: activity of MRS 1220 and potential antagonists.** Flp-In-CHO cells (2000 cells/well) stably expressing WT A<sub>3</sub>R were exposed to forskolin 10 μM, IB-MECA and test compound/MRS 1220/DMSO control for 30 min and cAMP accumulation detected. **A**) Representative dose response curves are shown as mean ± SEM expressed as percentage forskolin inhibition (10 μM) relative to IB-MECA. Key indicated in K1 is identical for all 'K' test compounds shown. **B**) pIC<sub>50</sub> values for individual repeats including half-log concentration are shown as mean ± SEM **C**) Schild analysis of data represented in **A/B**. A slope of 1 indicates a competitive antagonist. The x-axis is expressed as -log (molar concentration of antagonist) giving a negative Schild slope. **D**) Inverse agonism at the A<sub>3</sub>R. cAMP accumulation following a 30-minute stimulation with forskolin (10 μM) and increasing concentrations of antagonist/DMSO control was determined in WT A<sub>3</sub>R expressing Flp-In-CHO cells. Representative dose response curves are shown as mean ± SEM expressed as percentage forskolin (10 μM), relative to IB-MECA.

**Table 3. IB-MECA stimulated cAMP inhibition at WT A<sub>3</sub>R: activity of MRS 1220 and potential antagonists.** Forskolin stimulated cAMP inhibition was measured in Flp-In-CHO stably expressing A<sub>3</sub>R following stimulation with 10 μM forskolin, compound at the indicated concentration and varying concentrations of IB-MECA.

WT A <sub>3</sub> R Flp-In-CHO							Inverse agonism	
		pIC <sub>50</sub> <sup>a</sup>	E <sub>min</sub> <sup>b</sup>	Basal <sup>c</sup>	True Basal <sup>d</sup>	Span <sup>e</sup>	n	pEC <sub>50</sub> <sup>f</sup>
<b>IB-MECA only</b>		10.72 ±0.1	-8.42 ±2.6	107.7 ±2.6	102.2 ±2.9	116.1 ±3.5	27	
<b>MRS 1220</b>	0.1 nM	10.67 ±0.1	9.8 ±3.5**	107.6 ±3.7	99.7 ±4.0	97.9 ±4.9*	9	9.21 ±0.2
	1 nM	9.90 ±0.1****	20.9 ±3.8***	139.0 ±3.1****	124.8 ±4.1**	118.1 ±4.8	8	
	10 nM	8.39 ±0.1****	46.7 ±4.9****	143.6 ±2.1****	133.8 ±3.6****	96.9 ±5.1*	8	
<b>K1</b>	0.1 μM	10.55 ±0.1	-5.4 ±4.5	117.2 ±4.3	105.9 ±4.3	122.5 ±5.9	6	4.93 ±0.1
	1 μM	10.23 ±0.1***	7.9 ±4.5*	141.3 ±3.7****	132.0 ±6.6****	133.3 ±5.6	7	
	10 μM	9.47 ±0.1****	36.8 ±4.4****	161.3 ±2.9****	152.6 ±5.4****	124.5 ±5.1	6	
<b>K10</b>	0.1 μM	10.69 ±0.1	-5.2 ±4.3	125.3 ±4.0**	125.1 ±6.3*	130.5 ±5.6	5	5.81 ±0.1
	1 μM	10.13 ±0.1****	-1.3 ±4.4	146.7 ±3.5****	140.4 ±4.2****	148.1 ±5.5**	5	
	10 μM	9.12 ±0.1****	8.5 ±6.4	161.1 ±3.9****	150.0 ±5.8****	152.6 ±7.2****	5	
<b>K17</b>	0.1 μM	10.75 ±0.1	-0.9 ±3.2	115.5 ±3.3	111.8 ±4.5	116.5 ±4.5	7	6.24 ±0.2
	1 μM	10.17 ±0.1****	6.5 ±3.8	141.7 ±3.2****	131.7 ±5.2****	135.3 ±4.8*	7	
	10 μM	9.05 ±0.1****	14.83 ±5.2***	151.7 ±3.0****	143.9 ±6.1****	137.9 ±5.8*	7	
<b>K18</b>	0.1 μM	10.65 ±0.1	5.4 ±2.6	118.6 ±2.6	118.5 ±4.1	113.1 ±3.5	6	6.84 ±0.2
	1 μM	9.65 ±0.1****	10.7 ±4.1*	140.1 ±2.6****	125.6 ±5.1**	129.4 ±4.7	6	
	10 μM	8.38 ±0.1****	28.0 ±5.9****	147.7 ±2.4****	138.6 ±2.4****	119.7 ±6.1	7	
<b>K20</b>	0.1 μM	10.45 ±0.1	-1.6 ±4.1	127.1 ±4.2****	124.5 ±6.4**	128.7 ±5.6	6	6.96 ±0.2
	1 μM	9.54 ±0.1****	15.1 ±6.5**	151.0 ±4.3****	145.3 ±9.8****	135.9 ±7.4	5	
	10 μM	8.50 ±0.1****	23.3 ±7.8****	139.0 ±3.4****	128.0 ±8.0**	115.7 ±8.2	6	
<b>K23</b>	0.1 μM	10.56 ±0.1	-2.4 ±3.3	128.6 ±3.1****	123.4 ±5.2**	126.2 ±4.4	7	5.83 ±0.2
	1 μM	9.86 ±0.1****	9.2 ±4.5*	145.4 ±3.4****	139.6 ±6.4****	135.2 ±5.5	6	
	10 μM	9.24 ±0.1****	24.9 ±4.3****	149.9 ±2.7****	142.3 ±4.9****	125.1 ±4.9	7	
	0.1 μM	10.81 ±0.1	7.1 ±2.5	109.5 ±2.5	108.9 ±3.3	102.4 ±3.4	6	



<b>K25</b>	1 $\mu$ M	10.12 $\pm$ 0.1****	6.7 $\pm$ 3.8	126.7 $\pm$ 2.9**	124.0 $\pm$ 4.1*	120.1 $\pm$ 4.6	5	6.01 $\pm$ 0.1
	10 $\mu$ M	9.21 $\pm$ 0.1****	17.5 $\pm$ 3.2****	136.6 $\pm$ 1.8****	131.2 $\pm$ 4.1***	119.1 $\pm$ 3.5	6	
<b>K32</b>	0.1 $\mu$ M	10.74 $\pm$ 0.1	-0.6 $\pm$ 4.8	127.6 $\pm$ 4.9**	116.5 $\pm$ 6.0	128.2 $\pm$ 6.6	5	6.79 $\pm$ 0.2
	1 $\mu$ M	9.95 $\pm$ 0.1****	3.6 $\pm$ 4.3	146.9 $\pm$ 3.4****	130.5 $\pm$ 5.8***	143.3 $\pm$ 5.3**	5	
	10 $\mu$ M	9.09 $\pm$ 0.1****	17.7 $\pm$ 5.4***	152.3 $\pm$ 3.3****	140.2 $\pm$ 6.9****	134.6 $\pm$ 6.1	5	

<sup>a</sup>Negative logarithm of IB-MECA concentration required to produce a half-maximal response in the absence (IB-MECA only) or presence of 0.1, 1 or 10  $\mu$ M compound

<sup>b</sup>Minimum cAMP accumulation of IB-MECA as % 10  $\mu$ M forskolin response relative to IB-MECA only; the lower plateau of the fitted sigmoidal dose response curve

<sup>c</sup>The upper plateau of the fitted sigmoidal dose response curve corresponding to % 10  $\mu$ M forskolin inhibition, relative to IB-MECA

<sup>d</sup>The cAMP accumulation when stimulated with compound at the indicated concentration and 10  $\mu$ M forskolin stimulation only

<sup>e</sup>The difference between  $E_{\min}$  and basal signaling

<sup>f</sup>Value reported to determine inverse agonism: Negative logarithm of compound concentration required to produce a half-maximal response

Data are expressed as mean  $\pm$  SEM obtained in *n* separate experiments. Inverse agonist experiments were conducted in 3 separate experiments. Statistical significance (\*,  $p < 0.05$ ; \*\*,  $p < 0.01$ ; \*\*\*,  $p < 0.001$ ; \*\*\*\*,  $p < 0.0001$ ) compared to 'IB-MECA only' was determined by one-way ANOVA with Dunnett's post-test.

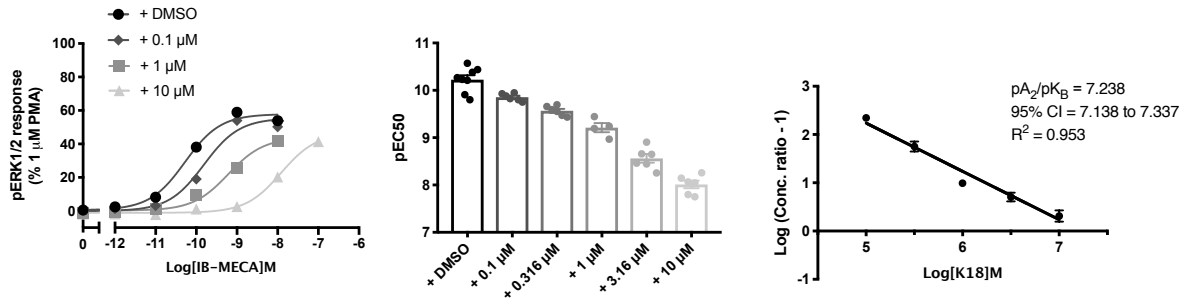


**Figure 3. K18 also reduced levels of agonist stimulated ERK1/2 phosphorylation.** pERK1/2 was detected in Flp-In-CHO cells stably expressing A<sub>3</sub>R (2000 cells/well) stimulated for 5 minutes with IB-MECA, with or without K18. **A)** Representative dose response curves for IB-MECA with K18 at the indicated concentration or DMSO control shown as mean  $\pm$  SEM expressed as % 1  $\mu$ M PMA response. **B)** pEC<sub>50</sub> values for individual repeats are shown as mean  $\pm$  SEM. **C)** Schild analysis of data represented in **A/B**.

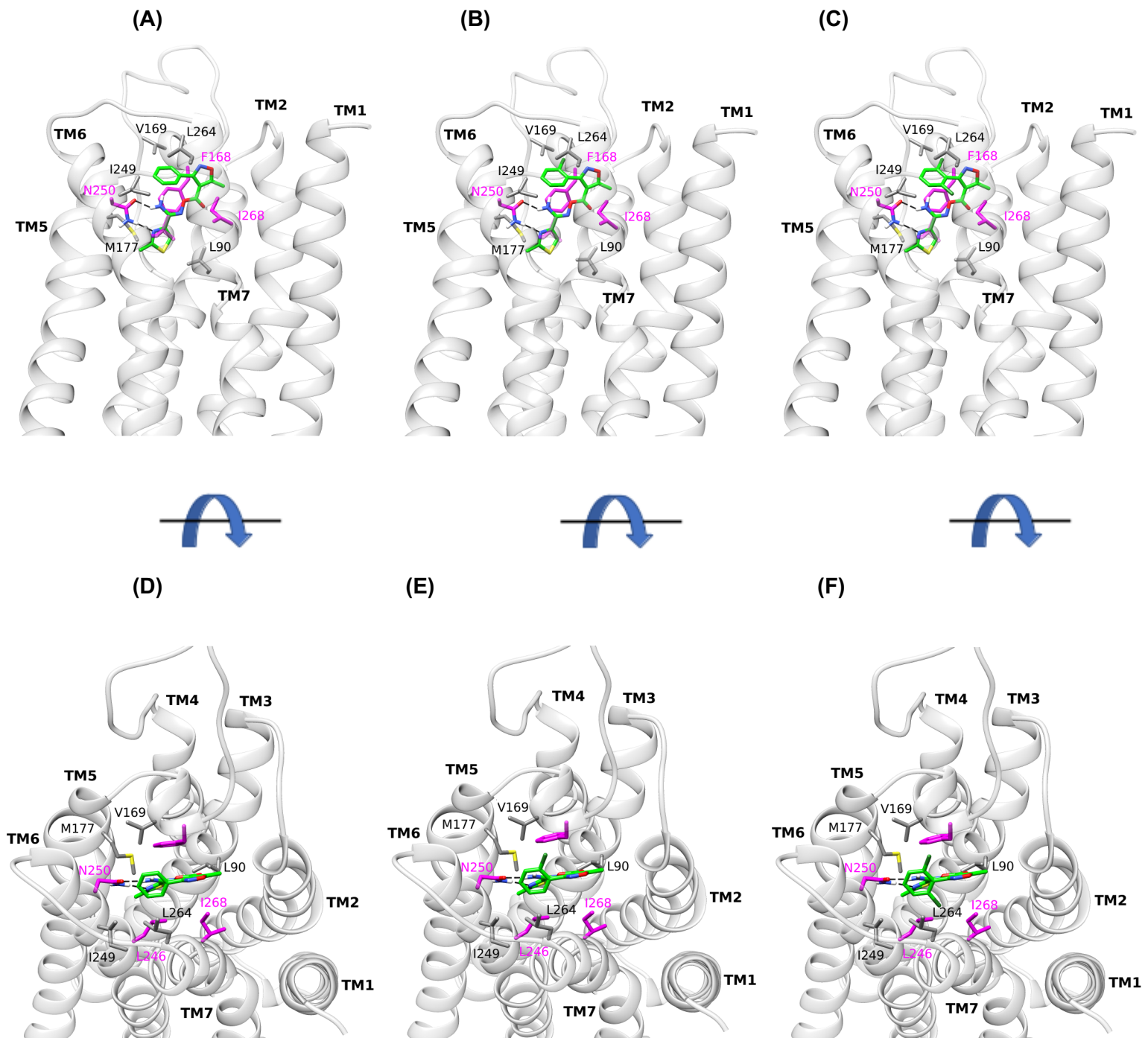


**Figure 4. Orthosteric binding area average structure of WT A<sub>3</sub>R in complex with K5, K17 and K18 from MD simulations with Amber14ff.** Side (A), top (D) view of K5 complex; side (B), top (E) view of K17 complex; side (C), top (F) view of K18 complex. Side chains of critical residues for binding indicated from the MD simulations are shown in sticks. Residues L90<sup>3,32</sup>, V169<sup>5,30</sup>, M177<sup>5,40</sup>, I249<sup>6,54</sup> and L264<sup>7,34</sup>, in which carbon atoms are shown in grey, were confirmed experimentally; in residues F168<sup>5,29</sup>, L246<sup>6,51</sup>, I268<sup>7,39</sup> and N250<sup>6,55</sup> carbon atoms are shown in magenta; nitrogen, oxygen and sulfur atoms are shown in blue, red and yellow respectively.

**Table 4. Binding of K5, K17, K18 and MRS 1220 to the A<sub>3</sub>R orthosteric binding area.** Effective binding energies ( $\Delta G_{\text{eff}}$ ) and energy components ( $E_{\text{vdW}}$ ,  $E_{\text{EL}}$ ,  $\Delta G_{\text{solv}}$ ) in kcal mol<sup>-1</sup> calculated using the MM-PBSA method.

	$E_{\text{vdW}}^a$	$E_{\text{EL}}^b$	$\Delta G_{\text{solv}}^c$	$\Delta G_{\text{eff}}^d$	$pK_B/pK_i^e$		
					Schild analysis <sup>f</sup>	NanoBRET <sup>g</sup>	Radioligand binding <sup>h</sup>
MRS 1220	-64.6 ± 2.6	-11.5 ± 2.5	39.2 ± 2.4	-36.9 ± 3.6	10.07	9.99 ± 0.04	8.2 - 9.2
K5	-42.0 ± 2.7	-9.6 ± 5.2	30.8 ± 4.3	-20.8 ± 4.3	ND	6.06 ± 0.09	5.02
K17	-47.0 ± 2.4	-8.8 ± 2.7	29.8 ± 2.9	-25.9 ± 3.6	6.35	6.33 ± 0.03	5.38
K18	-46.3 ± 2.9	-7.5 ± 2.4	26.9 ± 3.1	-26.9 ± 2.7	7.20	6.92 ± 0.10	6.05

<sup>a</sup>vdW energy of binding calculated using molecular mechanics

<sup>b</sup>Electrostatic energy of binding calculated using molecular mechanics

<sup>c</sup>Difference in solvation energy between the complex, the protein and the ligand, i.e.  $G_{\text{complex, solv}} - (G_{\text{protein, solv}} + G_{\text{ligand, solv}})$

<sup>d</sup>Effective binding free energy calculated as  $\Delta G_{\text{eff}} = \Delta E_{\text{MM}} + \Delta G_{\text{solv}}$ ; in Table 4,  $\Delta E_{\text{MM}} = E_{\text{vdW}} + E_{\text{EL}}$  (see Materials and Methods)

<sup>e</sup>Equilibrium dissociation constant of MRS 1220, K5, K17 and K18 as determined through three independent experimental approaches: Schild analysis ( $pK_B$ ), NanoBRET ( $pK_i$ ) or radioligand binding ( $pK_i$ )

<sup>f</sup> $pK_B$  obtained through Schild analysis in A<sub>3</sub>R stably expressing Flp-In CHO cells

<sup>g</sup> $pK_i$  (mean ± SEM) obtained in NanoBRET binding assays using Nluc-A<sub>3</sub>R stably expressing HEK 293 cells and determined through fitting our “Kinetics of competitive binding, rapid competitor dissociation” model or in the case of MRS 1220 through fitting with the ‘Kinetics of competitive binding’ model with a determined  $K_{\text{on}}$  ( $k_3$ ) and  $K_{\text{off}}$  ( $k_4$ ) rate of  $3.25 \pm 0.28 \times 10^8 \text{ M}^{-1} \text{ min}^{-1}$  and  $0.0248 \pm 0.005 \text{ min}^{-1}$ , respectively

<sup>h</sup> $pK_i$  values previously published for K5, K17 and K18 (Lagarias *et al.*, 2018) or MRS 1220 (Stoddart *et al.*, 2015) through radioligand binding assays.

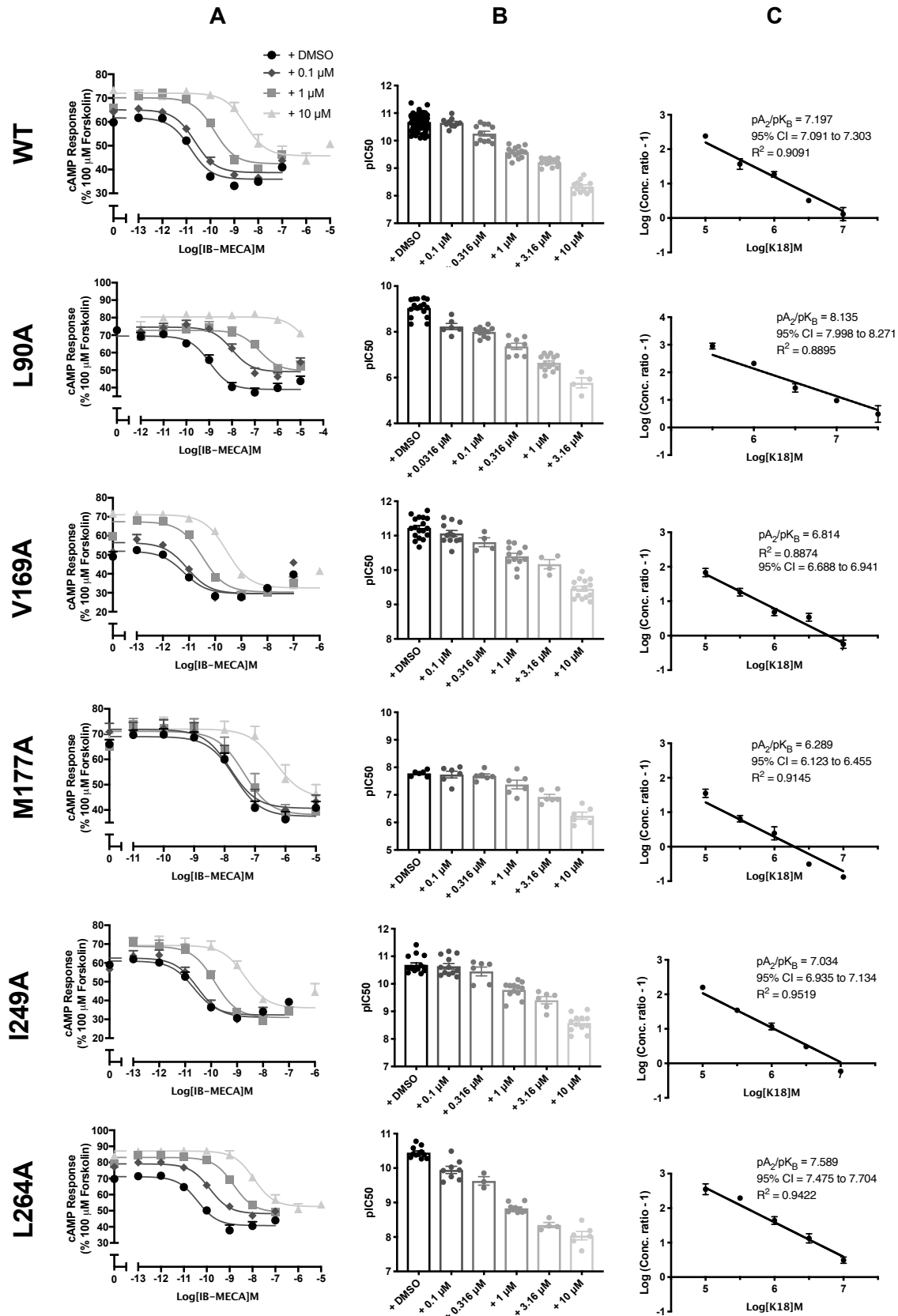


**Figure 5. IB-MECA stimulated cAMP inhibition at WT or mutant A<sub>3</sub>R with increasing concentrations of K18.** Flp-In-CHO cells (2000 cells/well) stably expressing WT or mutant A<sub>3</sub>R were exposed to forskolin 10  $\mu$ M, IB-MECA and K18 at varying concentrations for 30 min and cAMP accumulation detected. **A)** Representative dose response curves are shown as mean  $\pm$  SEM expressed as percentage maximum forskolin response (100  $\mu$ M). **B)** pIC<sub>50</sub> values for individual repeats including half-log concentration are shown as mean  $\pm$  SEM **C)** Schild analysis of data represented in **A/B**.

**Table 5. Antagonistic potency of K18 at A<sub>3</sub>R mutants.** cAMP accumulation as measured in Flp-In-CHO cells stably expressing WT or mutant A<sub>3</sub>R following stimulation with 10 μM forskolin, varying concentrations of IB-MECA and +/-K18 at the indicated concentration.

<b>+ DMSO</b>						
	<b>pIC<sub>50</sub><sup>a</sup></b>	<b>E<sub>min</sub><sup>b</sup></b>	<b>Basal<sup>c</sup></b>	<b>True Basal<sup>d</sup></b>	<b>Span<sup>e</sup></b>	<b>n</b>
<b>WT</b>	10.73 ±0.1	35.0 ±1.6	60.1 ±0.9	57.7 ±1.3	25.1 ±2.0	11
<b>L90A</b>	9.03 ±0.1****	43.3 ±3.2	73.2 ±2.7***	71.5 ±2.9***	29.9 ±1.8	8
<b>V169A</b>	11.33 ±0.1****	30.9 ±1.7	55.3 ±2.4	54.1 ±2.5	24.3 ±2.1	10
<b>M177A</b>	7.65 ±0.1****	38.6 ±2.7	70.2 ±2.0*	66.7 ±1.8	31.6 ±2.0	7
<b>I249A</b>	10.76 ±0.1	34.9 ±2.2	62.6 ±2.7	59.9 ±2.6	27.7 ±1.3	11
<b>L264A</b>	10.53 ±0.1	41.1 ±2.2	72.0 ±2.3**	70.8 ±2.6**	30.9 ±2.2	9
<b>+ 0.1 μM K18</b>						
	<b>pIC<sub>50</sub><sup>a</sup></b>	<b>E<sub>min</sub><sup>b</sup></b>	<b>Basal<sup>c</sup></b>	<b>True Basal<sup>d</sup></b>	<b>Span<sup>e</sup></b>	<b>n</b>
<b>WT</b>	10.64 ±0.1	37.3 ±1.8	63.0 ±2.2	61.8 ±2.6	25.8 ±0.9	5
<b>L90A</b>	7.88 ±0.1****	50.2 ±3.4*	77.2 ±2.6**	74.9 ±2.8*	27.0 ±3.1	7
<b>V169A</b>	11.11 ±0.1 *	31.9 ±1.8	62.6 ±2.2	60.6 ±3.1	30.6 ±2.1	7
<b>M177A</b>	7.69 ±0.1****	38.8 ±2.5	70.9 ±2.4	68.7 ±2.3	32.1 ±1.9	5
<b>I249A</b>	10.65 ±0.1	35.6 ±3.1	68.5 ±3.3	67.0 ±3.4	32.9 ±1.3	8
<b>L264A</b>	9.86 ±0.1***	45.7 ±2.0	79.7 ±2.7**	77.7 ±3.0**	34.0 ±2.8	7
<b>+ 1 μM K18</b>						
	<b>pIC<sub>50</sub><sup>a</sup></b>	<b>E<sub>min</sub><sup>b</sup></b>	<b>Basal<sup>c</sup></b>	<b>True Basal<sup>d</sup></b>	<b>Span<sup>e</sup></b>	<b>n</b>
<b>WT</b>	9.65 ±0.1	38.3 ±2.4	67.4 ±1.5	63.0 ±1.8	29.1 ±2.0	6
<b>L90A</b>	6.61 ±0.1****	54.3 ±3.6**	76.7 ±3.2	73.5 ±3.1	22.4 ±2.6	8
<b>V169A</b>	10.40 ±0.1****	31.9 ±2.3	68.8 ±1.7	66.5 ±2.0	36.9 ±2.5	7
<b>M177A</b>	7.27 ±0.1****	40.0 ±3.5	71.4 ±2.4	66.3 ±2.5	31.4 ±2.0	5
<b>I249A</b>	9.78 ±0.1	36.9 ±3.2	76.3 ±3.7	73.1 ±3.8	39.3 ±2.1*	8
<b>L264A</b>	8.80 ±0.1****	47.9 ±2.7	83.6 ±2.1***	79.8 ±2.4**	35.7 ±3.0	8
<b>+ 10 μM K18</b>						
	<b>pIC<sub>50</sub><sup>a</sup></b>	<b>E<sub>min</sub><sup>b</sup></b>	<b>Basal<sup>c</sup></b>	<b>True Basal<sup>d</sup></b>	<b>Span<sup>e</sup></b>	<b>n</b>
<b>WT</b>	8.38 ±0.2	45.1 ±1.7	72.0 ±1.5	68.9 ±1.6	26.9 ±1.3	7
<b>L90A</b>	ND	59.9 ±2.9**	81.7 ±2.3	78.1 ±2.4	22.8 ±2.0	5
<b>V169A</b>	9.44 ±0.1 ****	33.5 ±1.8**	71.8 ±1.6	69.2 ±1.5	38.3 ±2.0*	8
<b>M177A</b>	6.12 ±0.2****	45.7 ±3.2	72.1 ±2.3	67.6 ±2.4	26.6 ±1.6	5
<b>I249A</b>	8.55 ±0.2	36.6 ±2.1*	78.0 ±4.2	74.7 ±4.2	38.7 ±3.6*	8
<b>L264A</b>	7.98 ±0.1	49.1 ±3.1	85.4 ±2.7*	82.8 ±2.6**	33.7 ±5.0	5

<sup>a</sup>Negative logarithm of IB-MECA concentration required to produce a half-maximal response

<sup>b</sup>Minimum cAMP accumulation of IB-MECA as %100 μM forskolin. The lower plateau of the fitted sigmoidal dose response curve

<sup>c</sup>The upper plateau of the fitted sigmoidal dose response curve corresponding %100 μM forskolin

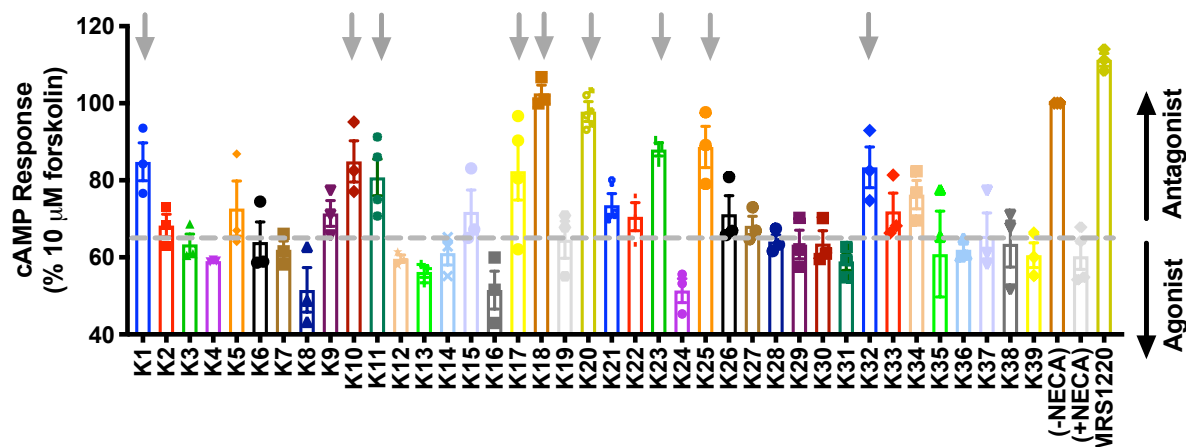
<sup>d</sup>The cAMP accumulation when stimulated with 10 μM forskolin only + DMSO/K18 at the indicated concentration

<sup>e</sup>The difference between E<sub>min</sub> and basal signalling

ND indicates an incomplete dose response curve due to the increased potency of K18 at this mutant.

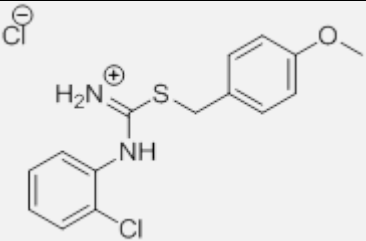
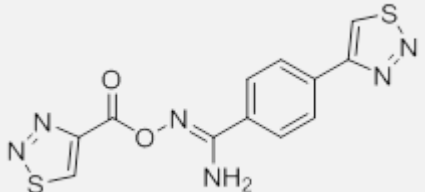
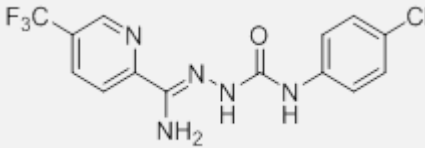
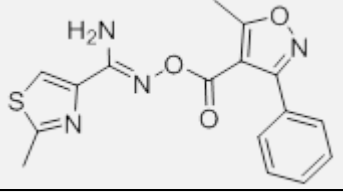
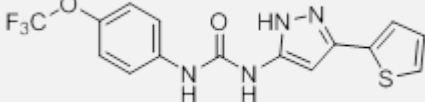
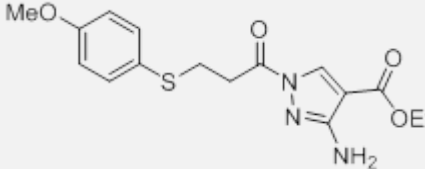
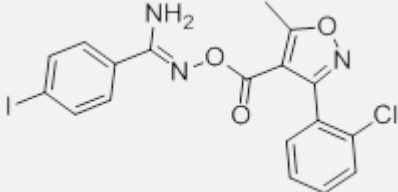
Data are expressed as mean ± SEM obtained in *n* separate experiments. All individual experiments were conducted in duplicate. Statistical significance (\*, *p* < 0.05; \*\*, *p* < 0.01; \*\*\*, *p* < 0.001; \*\*\*\*, *p* < 0.0001) compared to WT IB-MECA stimulation +/- K18 at each indicated concentration was determined by one-way ANOVA with Dunnett's post-test.

## SUPPORTING INFORMATION

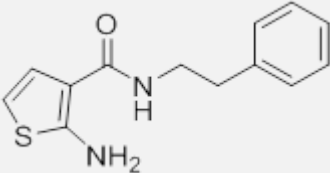
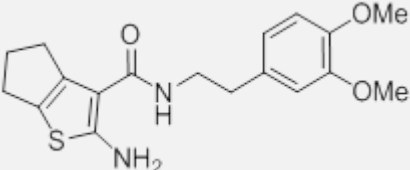
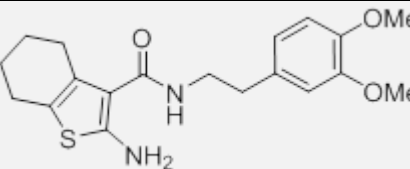
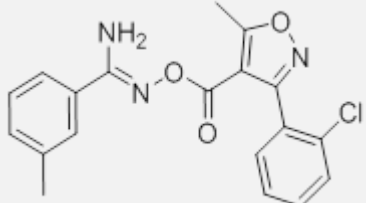
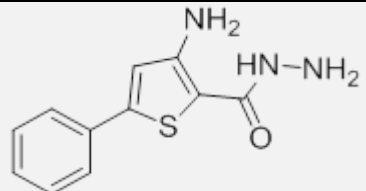
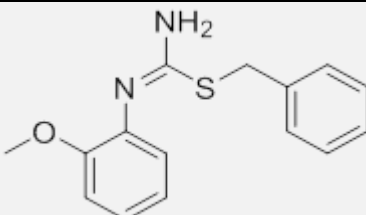
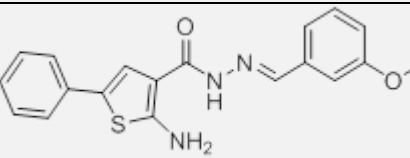
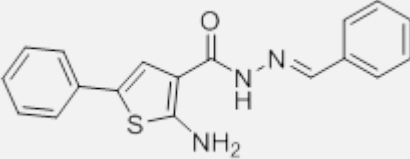
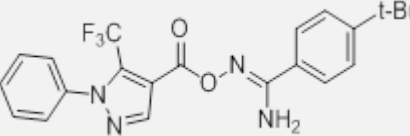


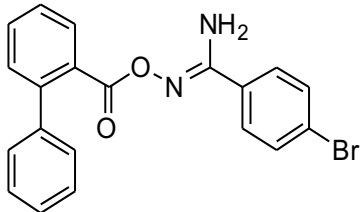
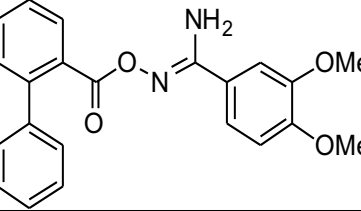
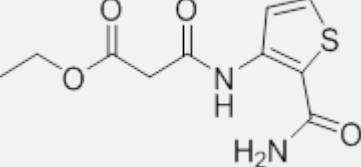
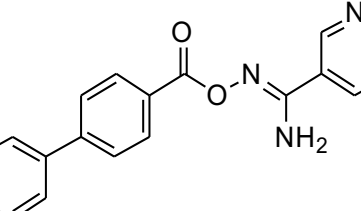
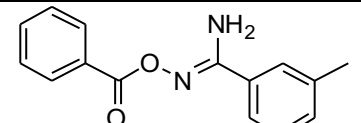
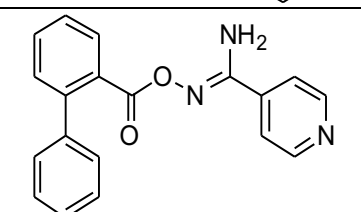
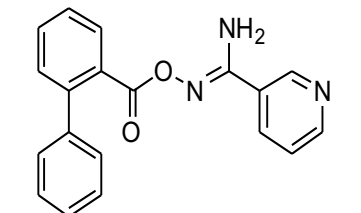
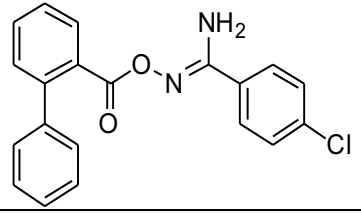
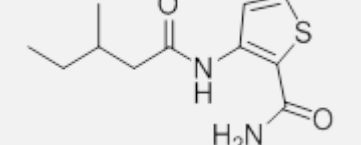
**Supplementary Figure 1. Screening for potential antagonists at the A<sub>3</sub>R.** cAMP accumulation was determined in Flp-In CHO cells stably expressing A<sub>3</sub>R (2000 cells/well) co-stimulated for 30 minutes with 10 μM forskolin, NECA at the pre-determined IC<sub>80</sub> concentration (3.16 nM) and 1 μM of compound/DMSO control. An elevation in cAMP accumulation above that of 10 μM forskolin and NECA, as indicated by the grey dotted line, suggesting the compound is acting as an antagonist (black upwards arrow). Included is MRS 1220 (1 μM) as a positive control for competitive antagonist of A<sub>3</sub>R. A reduction of cAMP accumulation (black downwards arrow) could indicate a compound is acting as an agonist. All values are mean ± SEM expressed as % 10 μM forskolin response ('DMSO') where  $n = 3$  independent experimental repeats, conducted in duplicate. Grey downward arrow indicates potential antagonists with a cAMP level >80%.

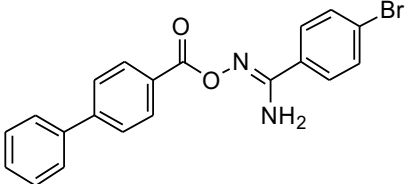
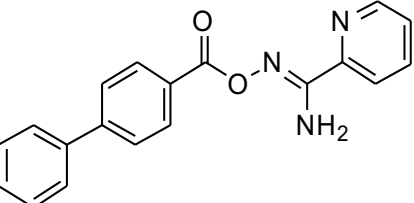
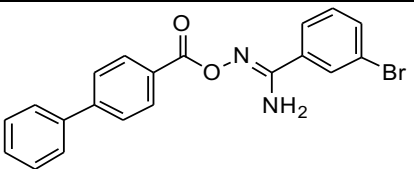
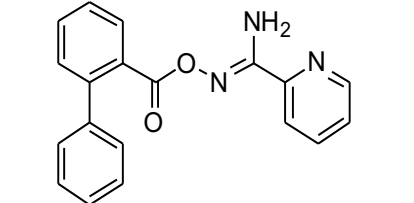
**Supplementary Table 1. Compounds with no apparent antagonist/agonist activity at the A<sub>3</sub>R.** Mean cAMP accumulation as measured in Flp-In CHO cells stably expressing A<sub>3</sub>R following stimulation with 10 μM forskolin only (DMSO) or NECA at the predetermined IC<sub>80</sub> concentration and 1 μM test compound/DMSO control. Binding affinities were obtained through radioligand binding assays and chemical structures of new compounds tested against the A<sub>1</sub>R, A<sub>2A</sub>R and A<sub>3</sub>R are also included.

	Compound Name	Chemical structure	A <sub>3</sub> R Flp-In CHO		Radioligand binding		
			Mean <sup>a</sup>	Mean Change <sup>b</sup>	Ki (μM) <sup>c</sup>		
					A <sub>3</sub> R	A <sub>1</sub> R	A <sub>2A</sub> R
	NECA		60.32 ±3.41	-	-	-	-
	DMSO		100.00 ±1.15	-35.73	-	-	-
K2	S05993 <sup>1</sup>		68.28 ±2.94	-7.96	16.6	>100	61.3
K3	SEW01061 <sup>1</sup>		63.37 ±2.66	-3.05	>100	>100	>100
K4	SPB06895 <sup>1</sup>		59.06 ±0.13	1.26	>100	>100	>100
K5	SPB02733 <sup>1</sup>		72.65 ±7.16	-12.33	<b>9.45</b>	>100	21.8
K6	KM08495 <sup>1</sup>		64.01 ±5.22	-3.69	30.6	>100	>100
K7	HTS06244 <sup>1</sup>		61.96 ±2.31	-1.64	18.3	>100	>100
K9	STK323059 <sup>1</sup>		71.40 ±3.37	8.75	<b>4.13</b>	<b>6.91</b>	>100



K12	STK441862 <sup>1</sup>		59.66 ±0.98	0.66	37.1	>100	>60
K13	STK448949 <sup>1</sup>		56.25 ±1.44	4.07	16.5	>30	>60
K14	STK450213 <sup>1</sup>		61.09 ±3.04	-0.77	14.8	>30	>60
K15	STK106598 <sup>1</sup>		71.79 ±5.69	-11.47	30.9	>100	>100
K16	Z56987720 <sup>1</sup>		51.51 ±4.91	8.81	19.7	>30	31.7
K19	RDR01677 <sup>1</sup>		64.58 ±4.94	-4.26	>100	>100	>100
K21	HTS13009 <sup>1</sup>		73.54 ±2.98	-13.22	<b>5.77</b>	>100	<b>3.93</b>
K22	HTS12882 <sup>1</sup>		70.56 ±3.64	-10.24	<b>5.16</b>	15.2	<b>4.59</b>
K24	GK01514 <sup>1</sup>		51.39 ±3.11	8.93	<b>5.39</b>	<b>7.48</b>	>100

K26	7709975		$71.17 \pm 4.84$	-10.85	<b>5.07</b>	>30	25.1
K27	7709775		$68.20 \pm 2.48$	-7.88	11.9	>30	30.0
K28	GK00478 <sup>1</sup>		$64.14 \pm 1.73$	-3.82	>100	18.0	30.0
K29	5687250		$63.32 \pm 3.72$	-3.00	>100	>100	>100
K30	6169223		$63.57 \pm 3.32$	-3.25	>30	>100	>100
K31	7721356		$58.93 \pm 2.28$	1.39	44.3	>100	>30
K33	STK300607		$71.97 \pm 4.74$	-11.65	>30	>100	>100
K34	7713195		$76.30 \pm 3.70$	-15.98	<b>7.53</b>	>100	>100
K35	Z1848163164 <sub>1</sub>		$71.56 \pm 3.54$	-11.24	27.4	<b>7.33</b>	>30

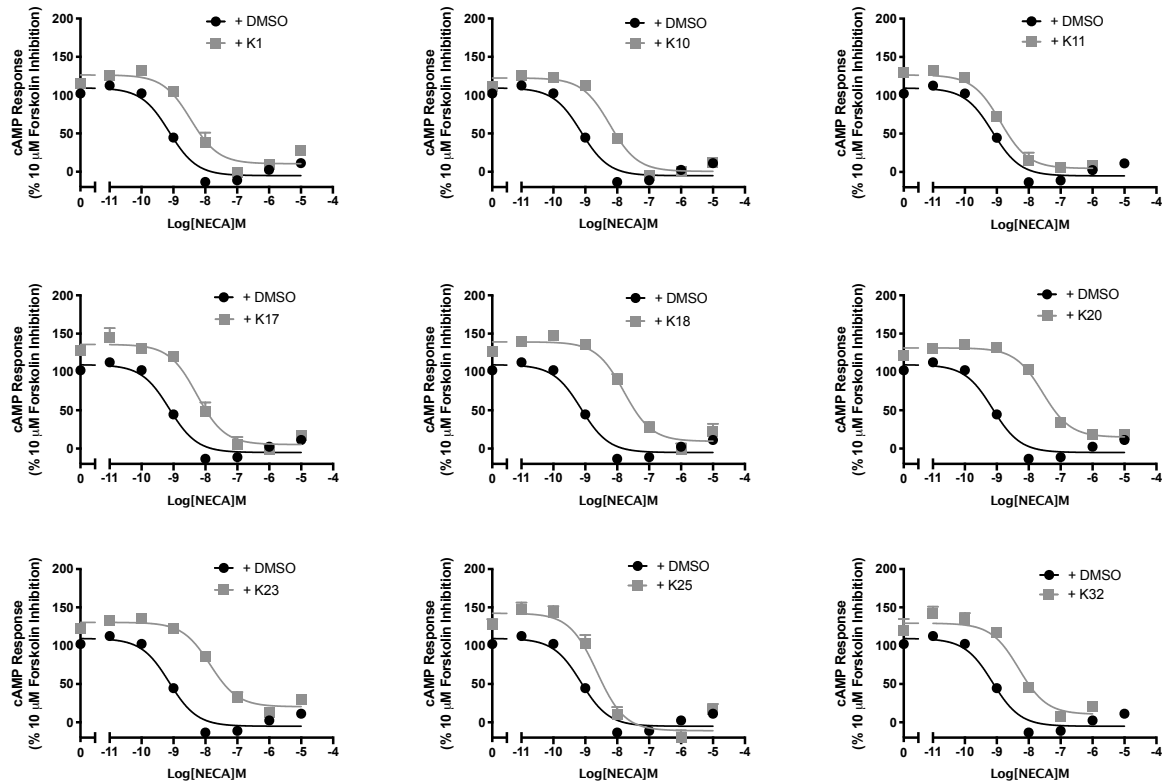
K36	STK710194		61.96 ±1.51	-1.64	>100	>100	>100
K37	5685368		65.57 ±6.00	-5.25	>100	>100	>100
K38	7968745		63.49 ±6.0	-3.17	>100	>100	>100
K39	7712234		60.56 ±3.20	-0.24	22.9	>100	>30

<sup>1</sup>Indicates previously published in Lagarias *et al.*, 2018 and is shown in grey

<sup>a</sup>cAMP accumulation mean ± SEM expressed as %10 μM forskolin response where  $n \geq 3$  independent experimental repeats, conducted in duplicate. Potential antagonists were selected for further investigation based on a high mean cAMP accumulation (>80%).

<sup>b</sup>Difference between the mean cAMP accumulation between 'NECA' and each compound expressed as %10 μM forskolin response

<sup>c</sup>Binding affinity measured in three independent experiments. Bold denotes binding affinity < 10 μM. All compounds did not exhibit binding evidence to A<sub>2B</sub>R.



**Supplementary Figure 2. Screening of potential antagonists at the A<sub>3</sub>R.** A<sub>3</sub>R Flp-In CHO cells (2000 cells/well) were exposed to forskolin 10 μM, NECA and DMSO or 1 μM test compound for 30 min and cAMP accumulation detected. All values are mean ± SEM expressed as percentage forskolin inhibition (10 μM) relative to NECA. *n* ≥ 3 independent experimental repeats, conducted in duplicate.

**Supplementary Table 2. cAMP accumulation as measured in A<sub>3</sub>R Flp-In CHO cells following stimulation with 10 μM forskolin, varying concentrations of NECA and 1 μM test compound/DMSO control**

A <sub>3</sub> R Flp-In CHO					
	pIC <sub>50</sub> <sup>a</sup>	E <sub>min</sub> <sup>b</sup>	Basal <sup>c</sup>	True Basal <sup>d</sup>	Span <sup>e</sup>
<b>NECA only</b>	8.94 ±0.1	-5.02 ±2.4	109.6 ±1.9	100.0 ±1.7	110.4 ±2.2
<b>K1</b>	8.46 ±0.1	10.5 ±4.5	126.9 ±3.3	115.7 ±2.8	118.0 ±3.1
<b>K10</b>	8.23 ±0.1	0.5 ±3.2	122.6 ±0.6	111.0 ±2.0	122.1 ±1.2
<b>K11</b>	8.88 ±0.1	4.7 ±4.3	126.5 ±3.2	109.1 ±2.0	121.9 ±5.2
<b>K17</b>	8.27 ±0.1	5.2 ±4.6	135.7 ±5.4	128.1 ±2.1	131.7 ±0.8
<b>K18</b>	7.79 ±0.1	9.5 ±4.8	139.2 ±3.7	127.2 ±3.2	130.9 ±7.1
<b>K20</b>	7.56 ±0.1	14.9 ±3.1	131.4 ±2.2	127.0 ±3.2	116.5 ±5.4
<b>K23</b>	7.85 ±0.1	20.4 ±3.2	130.5 ±2.6	122.7 ±3.9	110.7 ±2.7
<b>K25</b>	8.63 ±0.1	-10.9 ±5.7	136.6 ±7.1	138.5 ±4.9	134.4 ±5.8
<b>K32</b>	8.31 ±0.1	10.5 ±7.1	129.4 ±4.5	113.1 ±5.6	118.9 ±7.1

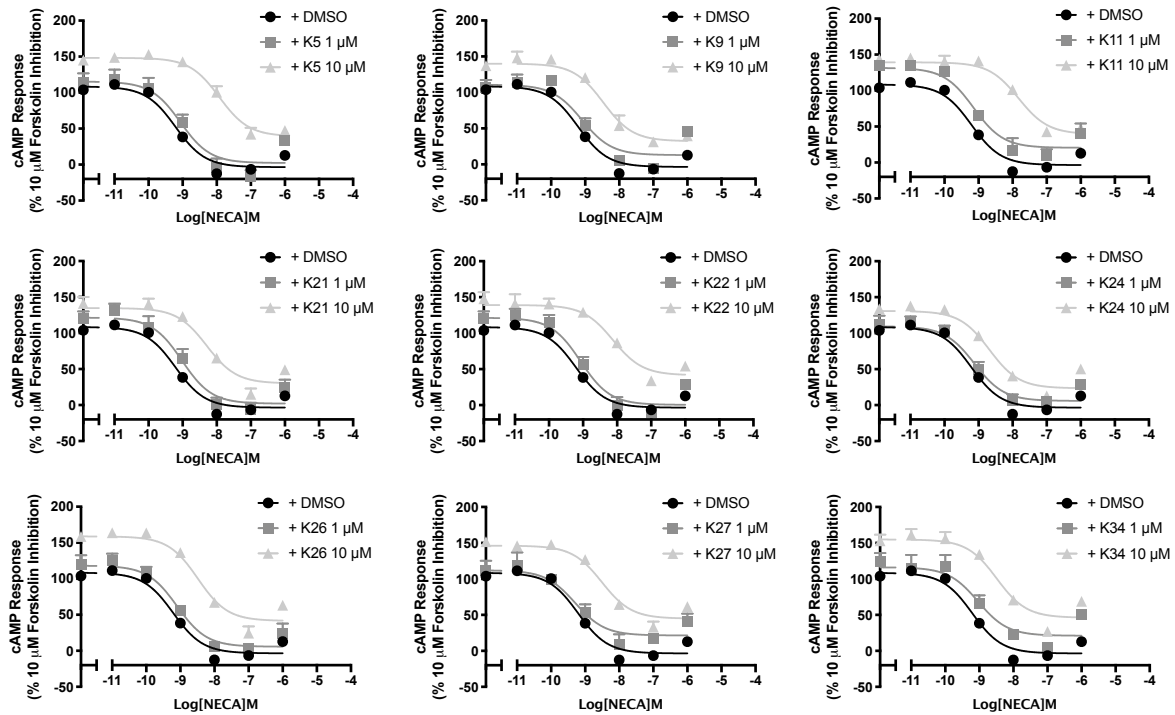
<sup>a</sup>Negative logarithm of NECA concentration required to produce a half-maximal response in the absence (DMSO) or presence of 1 μM compound

<sup>b</sup>Minimum cAMP accumulation of NECA as % 10 μM forskolin response, relative to NECA; the lower plateau of the fitted sigmoidal dose response curve

<sup>c</sup>The upper plateau of the fitted sigmoidal dose response curve corresponding to 100% of the 1 μM forskolin response

<sup>d</sup>The cAMP accumulation when stimulated with 1 μM compound and 10 μM forskolin stimulation only

<sup>e</sup>The difference between E<sub>min</sub> and basal signalling



**Supplementary Figure 3. Determining functional activity of compounds with a micromolar binding affinity for  $A_3R$ .**  $A_3R$  Flp-In CHO cells (2000 cells/well) were exposed to forskolin 10  $\mu$ M, NECA and DMSO or test compound at the indicated concentration for 30 min and cAMP accumulation determined. All values are mean  $\pm$  SEM expressed as percentage forskolin inhibition (10  $\mu$ M) relative to NECA.  $n = 3$  independent experimental repeats, conducted in duplicate.

**Supplementary Table 3. cAMP accumulation as measured in A<sub>3</sub>R Flp-In CHO cells following stimulation with 10 μM forskolin, varying concentrations of NECA and 1 μM or 10 μM test compound/DMSO control**

		<b>A<sub>3</sub>R Flp-In CHO</b>				
		<b>pIC<sub>50</sub><sup>a</sup></b>	<b>E<sub>min</sub><sup>b</sup></b>	<b>Basal<sup>c</sup></b>	<b>True Basal<sup>d</sup></b>	<b>Span<sup>e</sup></b>
<b>NECA only</b>		8.94 ±0.1	-5.02 ±2.4	109.6 ±1.9	100.0 ±1.7	110.4 ±2.2
<b>K5</b>	1 μM	9.06 ±0.2	2.3 ±8.2	115.3 ±7.0	102.5 ±10.1	113.1 ±10.5
	10 μM	7.93 ±0.1	39.3 ±5.6	148.3 ±3.1	142.1 ±9.3	108.9 ±6.2
<b>K9</b>	1 μM	9.09 ±0.2	13.0 ±7.6	110.7 ±6.6	86.2 ±6.0	97.8 ±9.7
	10 μM	8.47 ±0.2	32.3 ±5.7	140.0 ±3.9	123.3 ±3.8	107.7 ±6.7
<b>K11</b>	1 μM	8.88 ±0.1	4.7 ±4.3	126.5 ±3.2	109.1 ±2.0	121.9 ±5.2
	10 μM	7.83 ±0.2	39.4 ±7.5	139.3 ±5.0	119.8 ±9.2	99.9 ±8.2
<b>K21</b>	1 μM	9.02 ±0.2	2.0 ±7.6	121.5 ±6.1	101.6 ±5.1	119.4 ±9.4
	10 μM	8.29 ±0.2	30.1 ±6.8	134.7 ±4.3	118.6 ±4.8	104.6 ±7.7
<b>K22</b>	1 μM	9.07 ±0.2	0.4 ±7.1	121.3 ±5.8	101.9 ±8.4	120.9 ±8.8
	10 μM	8.12 ±0.2	41.6 ±7.1	139.1 ±4.2	124.5 ±8.2	97.5 ±8.0
<b>K24</b>	1 μM	9.12 ±0.2	5.9 ±6.5	109.5 ±4.9	103.6 ±7.7	103.7 ±7.9
	10 μM	8.67 ±0.1	23.4 ±4.5	130.8 ±3.3	117.7 ±0.9	107.4 ±5.7
<b>K26</b>	1 μM	9.10 ±0.2	5.7 ±6.2	118.2 ±4.8	98.9 ±8.8	112.5 ±7.6
	10 μM	8.49 ±0.1	41.5 ±5.7	158.8 ±3.9	143.0 ±5.9	117.3 ±6.6
<b>K27</b>	1 μM	9.29 ±0.2	21.5 ±7.4	112.0 ±6.8	93.1 ±6.7	90.5 ±9.7
	10 μM	8.51 ±0.2	44.9 ±5.3	146.3 ±3.7	133.2 ±3.0	101.4 ±6.2
<b>K34</b>	1 μM	9.04 ±0.2	21.1 ±8.7	116.2 ±6.9	97.1 ±2.1	95.1 ±10.8
	10 μM	8.49 ±0.2	46.2 ±6.7	154.9 ±4.7	143.6 ±7.6	108.7 ±7.8

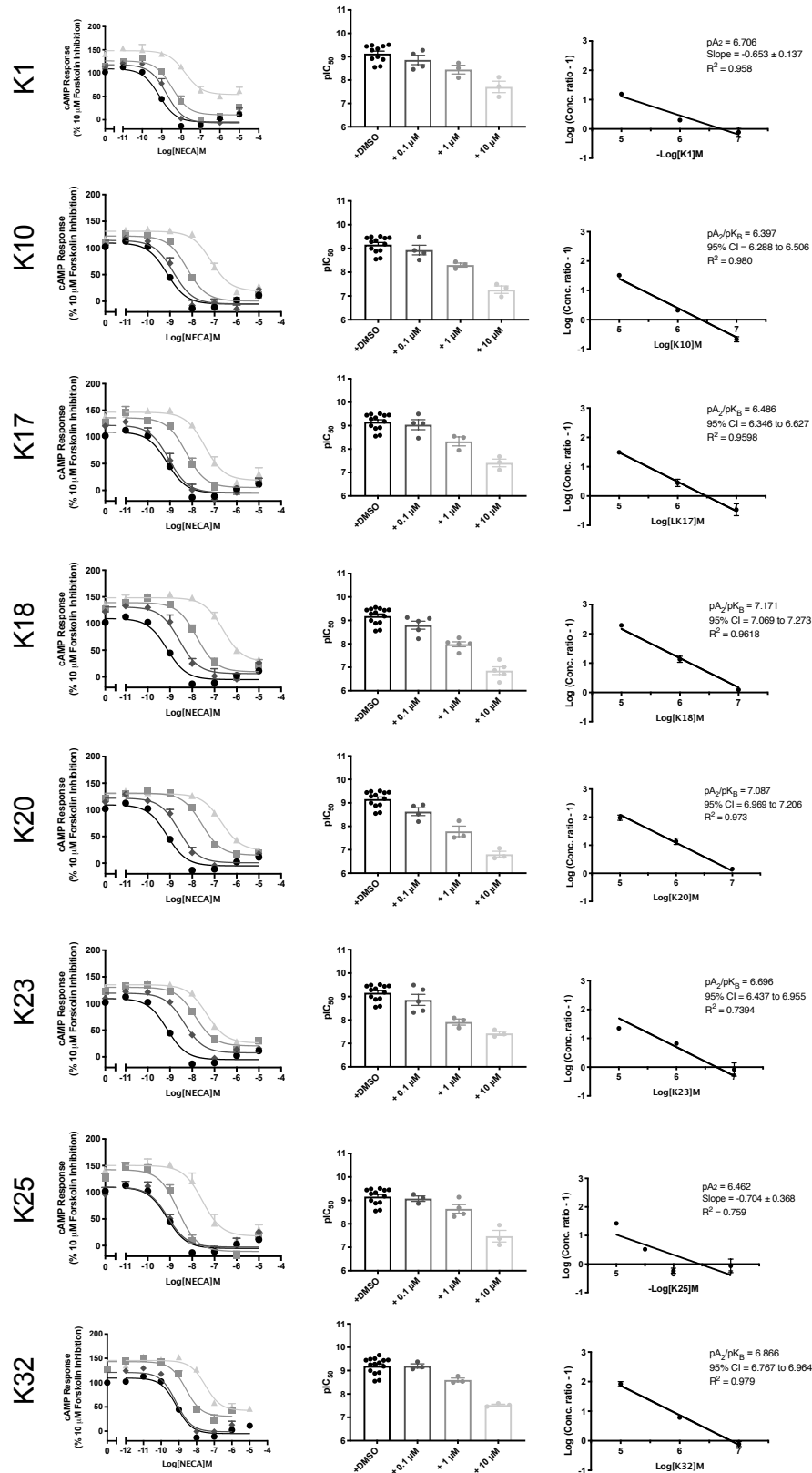
<sup>a</sup>Negative logarithm of NECA concentration required to produce a half-maximal response in the absence (DMSO) or presence of 1 μM or 10 μM compound

<sup>b</sup>Minimum cAMP accumulation of NECA as % 10 μM forskolin response, relative to NECA; the lower plateau of the fitted sigmoidal dose response curve

<sup>c</sup>The upper plateau of the fitted sigmoidal dose response curve corresponding to 100% of the 10 μM forskolin response

<sup>d</sup>The cAMP accumulation when stimulated with 1 μM or 10 μM compound and 10 μM forskolin stimulation only

<sup>e</sup>The difference between E<sub>min</sub> and basal signalling



**Supplementary Figure 4. NECA stimulated cAMP inhibition at WT A<sub>3</sub>R: activity of potential antagonists.** Flp-In-CHO cells (2000 cells/well) stably expressing WT A<sub>3</sub>R were exposed to forskolin 10 μM, NECA and test compound/DMSO control for 30 min and cAMP accumulation detected. **A)** Representative dose response curves are shown as mean ± SEM expressed as percentage forskolin inhibition (10 μM) relative to NECA. **B)** pIC<sub>50</sub> values are shown as mean ± SEM. **C)** Schild analysis of data represented in **A/B**. A slope of 1 indicates a competitive antagonist. The x-axis is expressed as -log (molar concentration of antagonist) giving a negative Schild plot slope.



**Supplementary Table 4. cAMP accumulation as measured in Flp-In-CHO stably expressing A<sub>3</sub>R following stimulation with 10 μM forskolin, compound at the indicated concentration and varying concentrations of NECA**

		WT A <sub>3</sub> R Flp-In-CHO				
		pIC <sub>50</sub> <sup>a</sup>	E <sub>min</sub> <sup>b</sup>	Basal <sup>c</sup>	True Basal <sup>d</sup>	Span <sup>e</sup>
<b>NECA only</b>		8.94 ±0.1	-5.02 ±2.4	109.6 ±1.9	100.0 ±1.7	110.4 ±2.2
<b>K1</b>	0.1 μM	8.73 ±0.2	-8.38 ±5.4	118.3 ±3.3	107.2 ±3.0	117.0 ±2.5
	1 μM	8.46 ±0.1	10.5 ±4.5	126.9 ±3.3	115.7 ±2.8	118.0 ±3.1
	10 μM	7.80 ±0.1	54.1 ±4.5	148.5 ±6.6	145.7 ±2.4	96.9 ±3.3*
<b>K10</b>	0.1 μM	8.76 ±0.2	-6.0 ±5.6	112.9 ±1.9	98.2 ±3.1	109.7 ±2.8
	1 μM	8.23 ±0.1	0.54 ±3.2	122.6 ±0.6	111.0 ±2.0	122.1 ±1.2
	10 μM	7.15 ±0.1	19.2 ±4.5	131.7 ±1.8	121.9 ±2.6	112.6 ±2.6
<b>K17</b>	0.1 μM	9.00 ±0.1	-5.5 ±4.8	122.6 ±1.9	115.0 ±4.4	124.6 ±2.5
	1 μM	8.27 ±0.1	5.2 ±4.6	135.7 ±5.4	128.1 ±2.1	131.7 ±0.8
	10 μM	7.43 ±0.1	18.7 ±5.2	146.6 ±3.3	138.6 ±3.1	131.2 ±4.0
<b>K18</b>	0.1 μM	8.58 ±0.1	6.1 ±5.5	131.1 ±5.4	122.3 ±2.1	127.5 ±4.7
	1 μM	7.79 ±0.1	9.5 ±4.8	139.2 ±3.7	127.2 ±3.2	130.9 ±7.1
	10 μM	6.61 ±0.1	28.3 ±5.5	148.5 ±2.6	143.1 ±1.3	121.7 ±1.4
<b>K20</b>	0.1 μM	8.38 ±0.1	2.2 ±4.1	119.6 ±3.9	122.3 ±2.1	117.9 ±3.4
	1 μM	7.56 ±0.1	14.9 ±3.1	131.4 ±2.2	127.0 ±3.2	116.5 ±5.4
	10 μM	6.68 ±0.1	23.6 ±3.8	130.2 ±1.9	143.1 ±1.3	106.8 ±5.5
<b>K23</b>	0.1 μM	8.36 ±0.1	7.5 ±3.4	119.5 ±3.2	117.3 ±3.2	112.2 ±1.3
	1 μM	7.85 ±0.1	20.4 ±3.2	130.5 ±2.6	122.7 ±3.9	110.7 ±2.7
	10 μM	7.35 ±0.1	25.9 ±3.5	135.3 ±2.3	129.3 ±4.9	109.2 ±7.3
<b>K25</b>	0.1 μM	9.10 ±0.2	-2.7 ±6.2	122.0 ±7.0	126.7 ±6.5	126.6 ±4.4
	1 μM	8.63 ±0.1	-10.9 ±5.7	136.6 ±7.1	138.5 ±4.9	134.4 ±5.8
	10 μM	7.54 ±0.2	17.9 ±7.0	151.7 ±3.5	148.5 ±5.4	136.5 ±2.5
<b>K32</b>	0.1 μM	9.22 ±0.1	-1.3 ±4.9	124.5 ±5.4	107.4 ±5.4	114.9 ±8.4
	1 μM	8.62 ±0.1	30.5 ±4.9	144.8 ±4.1	132.3 ±4.3	115.4 ±6.8
	10 μM	7.53 ±0.1	42.6 ±3.0	144.7 ±2.9	126.5 ±3.0	91.7 ±6.8

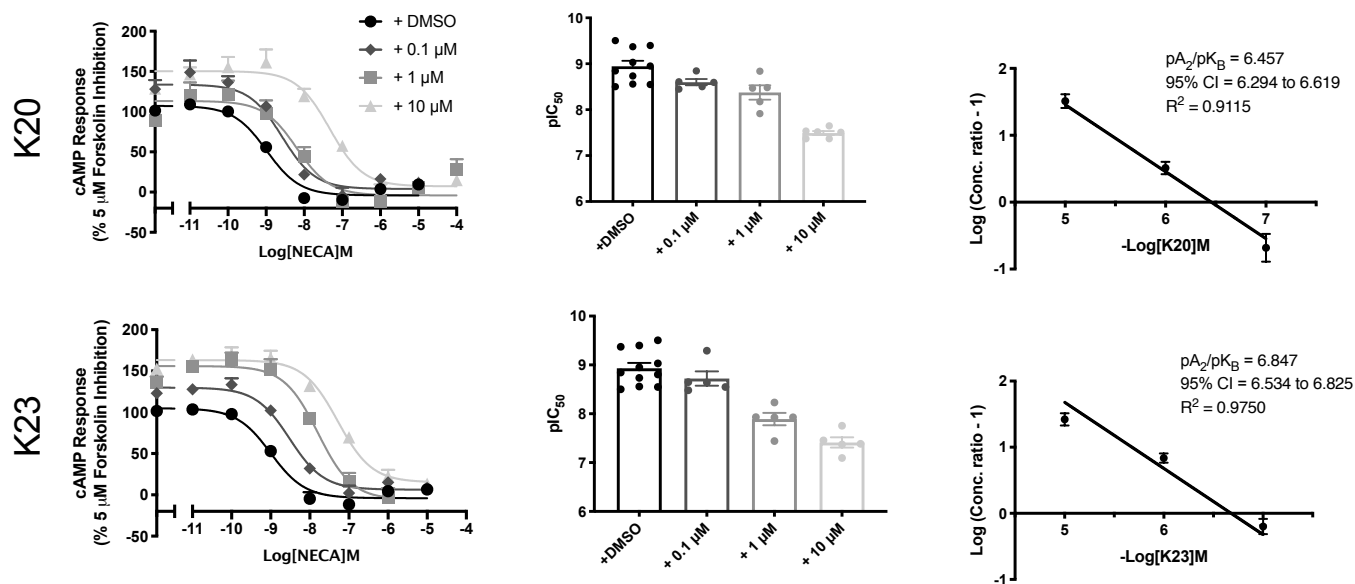
<sup>a</sup>Negative logarithm of NECA concentration required to produce a half-maximal response in the absence (NECA only) or presence of 0.1, 1 or 10 μM compound

<sup>b</sup>Minimum cAMP accumulation of NECA as % 10 μM forskolin response relative to NECA response; The lower plateau of the fitted sigmoidal dose response curve

<sup>c</sup>The upper plateau of the fitted sigmoidal dose response curve corresponding to % 10 μM forskolin inhibition, relative to NECA

<sup>d</sup>The cAMP accumulation when stimulated with compound at the indicated concentration and 10 μM forskolin stimulation only

<sup>e</sup>The difference between E<sub>min</sub> and basal signaling



**Supplementary Figure 5. NECA stimulated cAMP inhibition at A<sub>1</sub>R.** CHO-K1 cells (2000 cells/well) stably expressing A<sub>1</sub>R were exposed to forskolin 5 μM, NECA and test compound/DMSO control for 30 min and cAMP accumulation detected. **A)** Representative dose response curves are shown as mean ± SEM expressed as percentage forskolin inhibition (5 μM) relative to NECA. **B)** pIC<sub>50</sub> values for individual repeats including half-log concentration are shown as mean ± SEM. **C)** Schild analysis of data represented in **A/B**. A slope of 1 indicates a competitive antagonist. The x-axis is expressed as -log (molar concentration of antagonist) giving a negative Schild plot slope.

**Supplementary Table 5. cAMP accumulation as measured in CHO-K1 stably expressing A<sub>1</sub>R following stimulation with 5 μM forskolin, compound at the indicated concentration and varying concentrations of NECA**

		<b>A<sub>1</sub>R CHO-K1</b>				
		<b>pIC<sub>50</sub><sup>a</sup></b>	<b>E<sub>min</sub><sup>b</sup></b>	<b>Basal<sup>c</sup></b>	<b>True Basal<sup>d</sup></b>	<b>Span<sup>e</sup></b>
<b>NECA only</b>		8.94 ±0.1	-5.1 ±1.0	107.5 ±3.4	100.0 ±1.16	111.4 ±4.0
<b>K20</b>	0.1 μM	8.68 ±0.1 *	-5.3 ±9.3	130.1 ±2.6	110.9 ±4.4	135.4 ±6.7
	1 μM	8.37 ±0.1 ****	-3.7 ±3.8	106.6 ±8.5	113.6 ±18.1	98.6 ±5.6
	10 μM	7.38 ±0.1 ****	8.1 ±2.0**	136.6 ±2.3**	140.7 ±6.4*	153.5 ±12.1***
<b>K23</b>	0.1 μM	8.52 ±0.1 ****	3.3 ±5.6	131.6 ±5.1	117.6 ±3.2	128.3 ±7.2
	1 μM	8.00 ±0.1 ****	0.1 ±6.3	132.8 ±3.8*	119.8 ±3.2*	149.5 ±15.5*
	10 μM	7.49 ±0.1 ****	12.2 ±4.7*	178.3 ±16.2****	170.2 ±13.6****	166.0 ±15.0**

<sup>a</sup>Negative logarithm of NECA concentration required to produce a half-maximal response in the absence (NECA only) or presence of compound

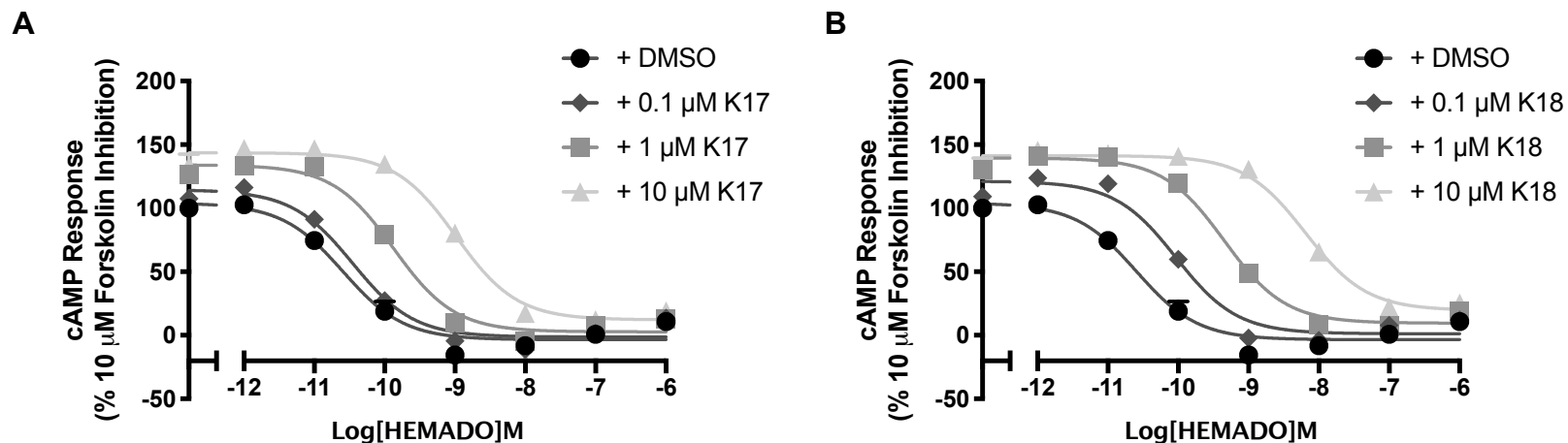
<sup>b</sup>Minimum cAMP accumulation of NECA as % 5 μM forskolin response; the lower plateau of the fitted sigmoidal dose response curve

<sup>c</sup>The upper plateau of the fitted sigmoidal dose response curve corresponding to 100% of the 5 μM forskolin response

<sup>d</sup>The cAMP accumulation when stimulated with compound at the indicated concentration and 5 μM forskolin stimulation only

<sup>e</sup>The difference between E<sub>min</sub> and basal signalling

Statistical significance (\*,  $p < 0.05$ ; \*\*,  $p < 0.01$ ; \*\*\*,  $p < 0.001$ ; \*\*\*\*,  $p < 0.0001$ ) compared to NECA only stimulation was determined by one-way ANOVA with Dunnett's post-test.



**Supplementary Figure 6. Antagonism of the HEMADO induced cAMP inhibition at the A<sub>3</sub>R of A) K17 and B) K18.** A<sub>3</sub>R stably expressing Flp-In CHO cells (2000 cells/well) were exposed to forskolin 10  $\mu$ M, HEMADO and DMSO/test compound at the indicated concentration for 30 min and cAMP accumulation detected. All values are mean  $\pm$  SEM expressed as percentage forskolin inhibition (10  $\mu$ M) relative to HEMADO.  $n = 3$  independent experimental repeats, conducted in duplicate.

**Supplementary Table 6. cAMP accumulation as measured in Flp-In-CHO cells stably expressing A<sub>3</sub>R following stimulation with 10 μM forskolin, HEMADO and varying concentrations of test compound**

		<b>A<sub>3</sub>R CHO-K1</b>				
		<b>pIC<sub>50</sub><sup>a</sup></b>	<b>E<sub>min</sub><sup>b</sup></b>	<b>Basal<sup>c</sup></b>	<b>True Basal<sup>d</sup></b>	<b>Span<sup>e</sup></b>
<b>HEMADO only</b>		10.54 ±0.2	-3.48 ±2.7	103.8 ±4.1	100.1 ±1.9	107.3 ±4.7
<b>K17</b>	0.1 μM	10.45 ±0.1	-1.31 ±2.8	114.3 ±4.0	107.6 ±3.6	115.6 ±4.6
	1 μM	9.89 ±0.1	2.71 ±2.9	134.0 ±3.3	126.4 ±4.1	131.3 ±4.3
	10 μM	8.99 ±0.1	12.16 ±4.1	143.6 ±3.4	133.3 ±9.3	131.5 ±5.2
<b>K18</b>	0.1 μM	10.04 ±0.1	1.20 ±2.9	121.2 ±3.5	109.1 ±2.2	120.0 ±4.4
	1 μM	9.34 ±0.1	9.52 ±3.9	139.5 ±2.8	130.1 ±5.3	130.0 ±3.9
	10 μM	8.12 ±0.1	19.6 ±4.6	141.4 ±2.8	130.2 ±9.3	121.8 ±5.3

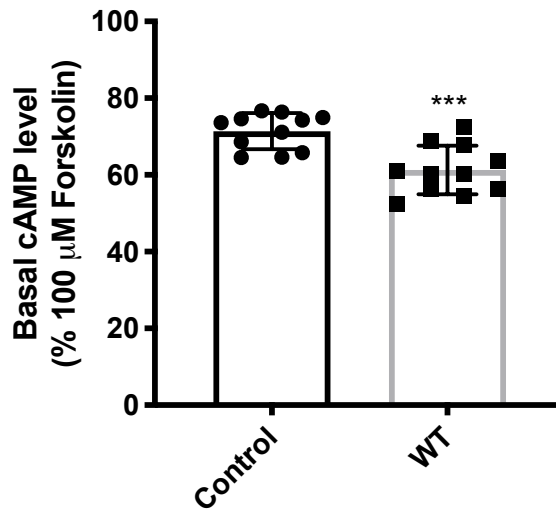
<sup>a</sup>Negative logarithm of HEMADO concentration required to produce a half-maximal response in the absence (HEMADO only) or presence of compound

<sup>b</sup>Minimum cAMP accumulation of HEMADO as % 10 μM forskolin response; the lower plateau of the fitted sigmoidal dose response curve

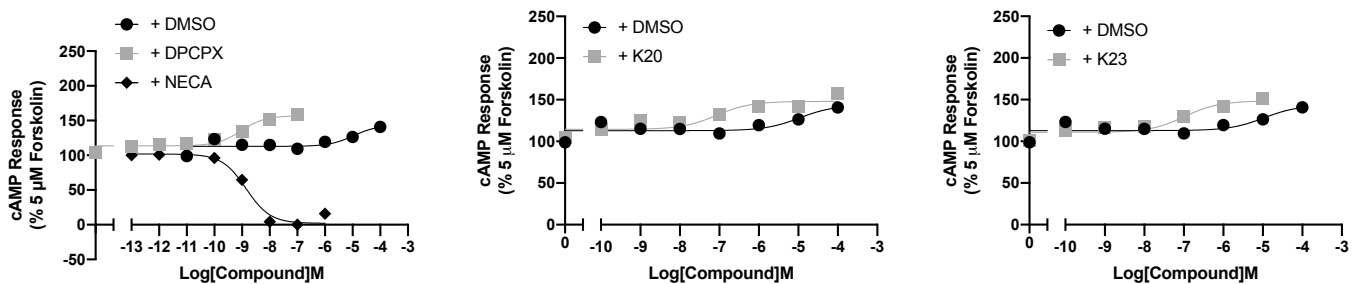
<sup>c</sup>The upper plateau of the fitted sigmoidal dose response curve corresponding to 100% of the 10 μM forskolin response

<sup>d</sup>The cAMP accumulation when stimulated with compound at the indicated concentration and 10 μM forskolin stimulation only

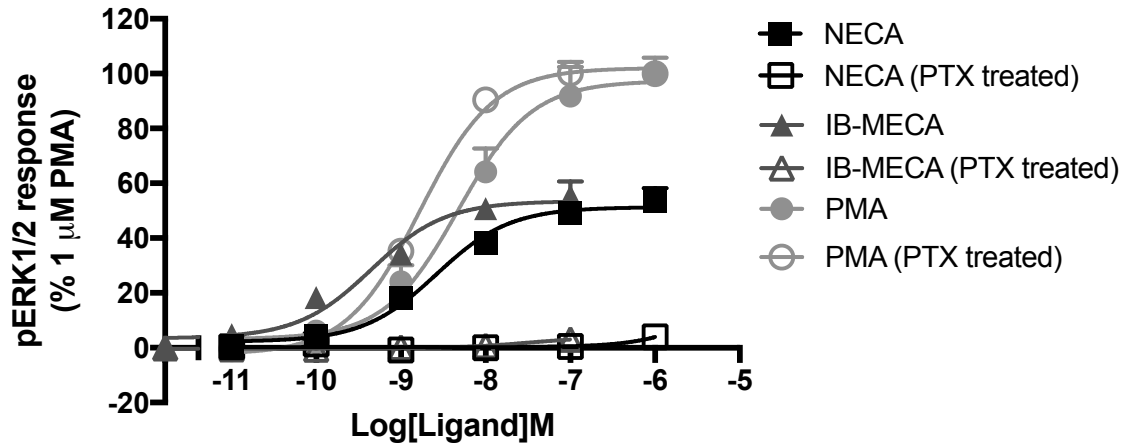
<sup>e</sup>The difference between E<sub>min</sub> and basal signalling



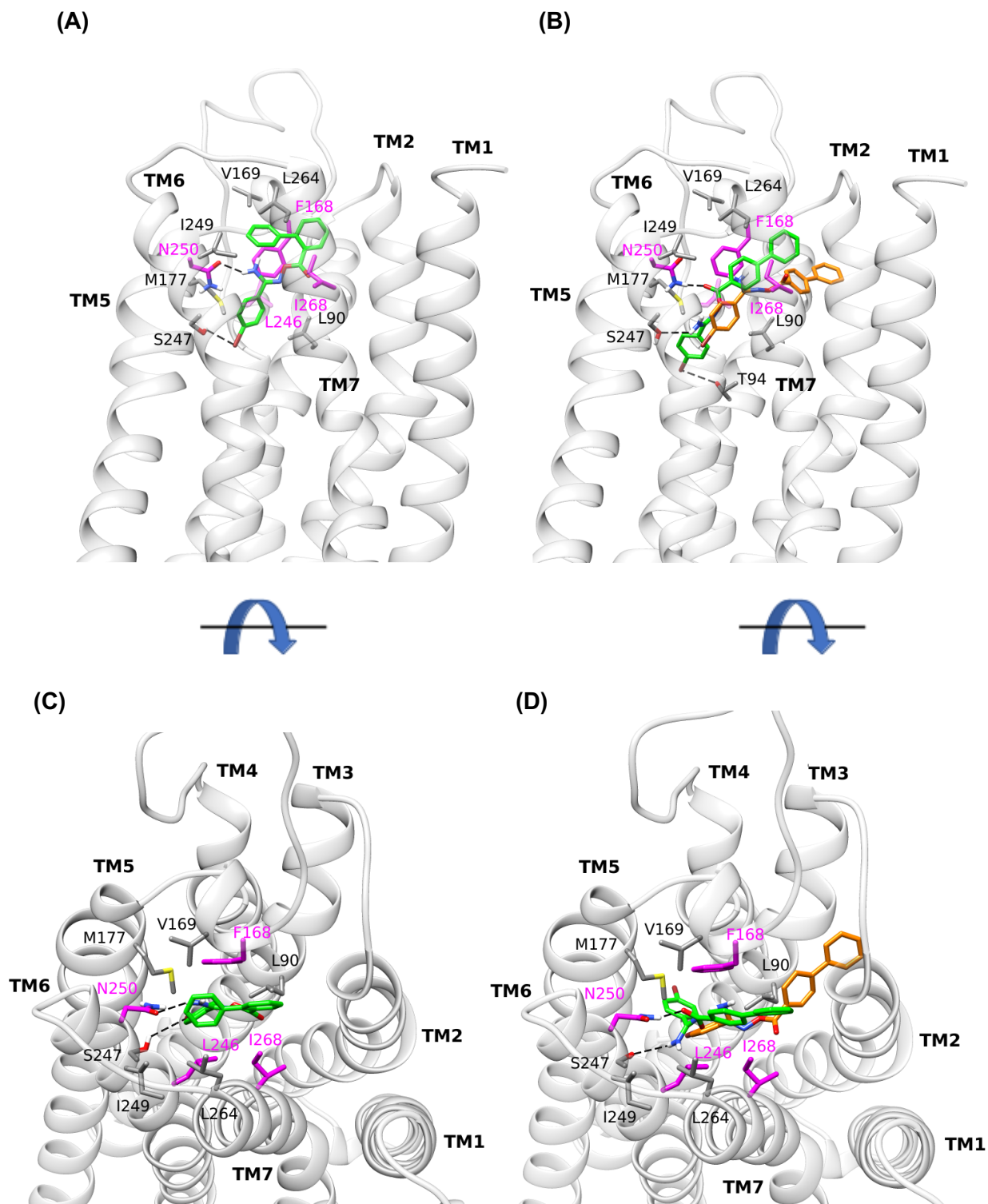
**Supplementary Figure 7. A<sub>3</sub>R shows constitutive activity.** cAMP accumulation following a 30-minute stimulation with forskolin (5 μM and 10 μM) in WT A<sub>3</sub>R expressing Flp-In-CHO cells was reduced compared to control (Flp-In-CHO cells). Statistical significance (\*\*\*,  $p < 0.001$ ) compared to control was determined by Student's t-test.



**Supplementary Figure 8. Inverse agonism at the A<sub>1</sub>R.** cAMP accumulation following a 30-minute stimulation with forskolin (5 μM) and increasing concentrations of antagonist, NECA or DMSO control was determined in A<sub>1</sub>R expressing CHO cells. Representative dose response curves are shown as mean ± SEM expressed as percentage forskolin (5 μM), relative to NECA.

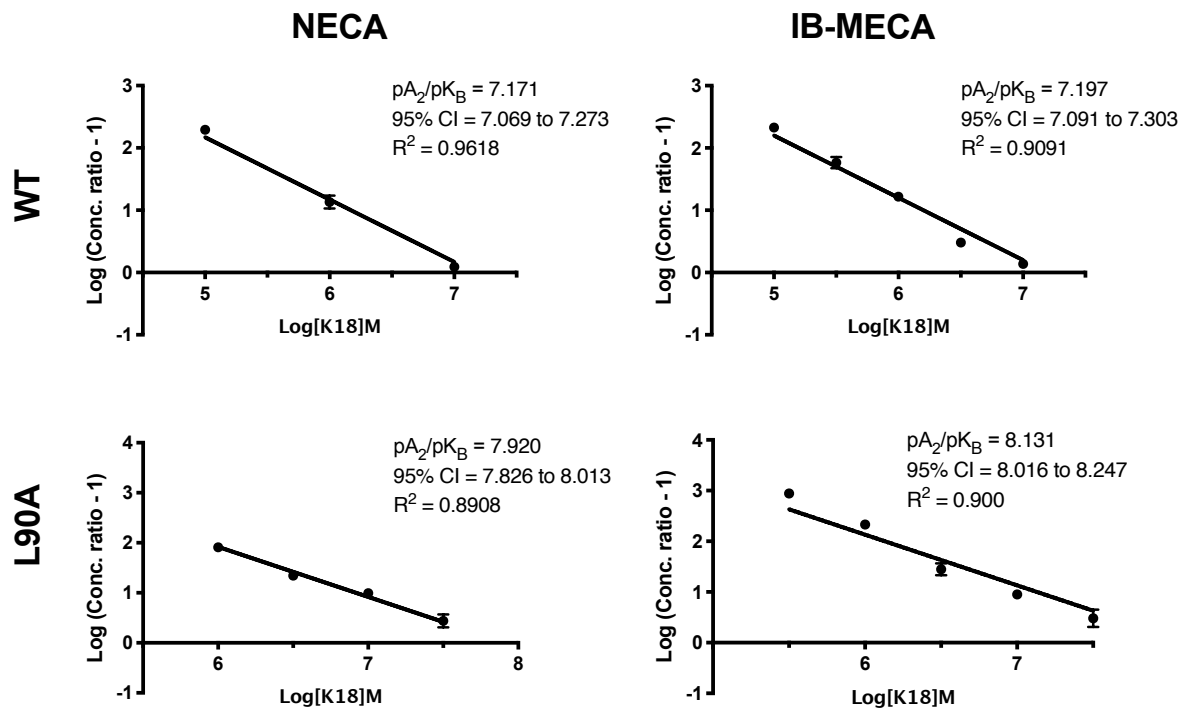


**Supplementary Figure 9. A<sub>3</sub>R stimulated pERK activity is entirely G<sub>i/o</sub> mediated.** pERK was detected in Flp-In-CHO cells stably expressing A<sub>3</sub>R (2000 cells/well) stimulated for 5 minutes with NECA or IB-MECA with or without Pertussis toxin (PTX) treatment (16 hours at 100 ng/mL). All values are mean ± SEM expressed as % 1 μM PMA response where  $n = 3$  for none-PTX treated and  $n = 1$  for PTX treated, conducted in duplicate.

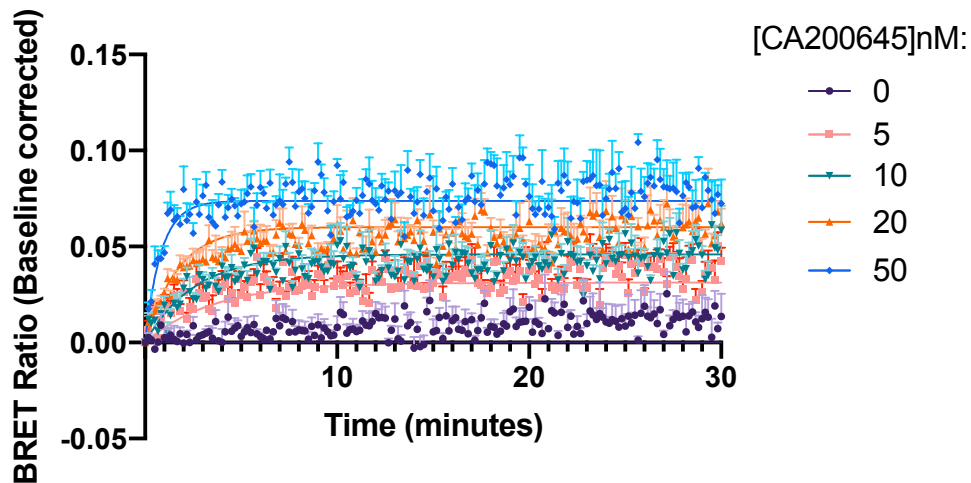


**Supplementary Figure 10. Average structure of WT A<sub>3</sub>R in complex with K26 and K36 from MD simulations with Amber14ff.** Side (A), top (C) view of the average structure of K26 which binds A<sub>3</sub>R ( $K_d = 5.07 \mu\text{M}$ ) but has not antagonistic activity and, side (B), top (D) view of the average structure of K36 which did not bind A<sub>3</sub>R inside the orthosteric binding area from 100 MD simulations. Side chains of critical residues for binding resulted from the MD simulations are shown in sticks. Residues L90<sup>3,32</sup>, V169<sup>5,30</sup>, M177<sup>5,40</sup>, I249<sup>6,54</sup>, L264<sup>7,34</sup>, in which carbon atoms are shown in grey, were confirmed experimentally; in residues F168<sup>5,29</sup>, L246<sup>6,51</sup>, I268<sup>7,39</sup> and N250<sup>6,55</sup> carbon atoms are shown in magenta; nitrogen, oxygen and sulfur atoms are shown in blue, red and yellow respectively. For K36 the conformation adopted after 100 ns, which loses binding interactions with the receptor area, is indicated with orange colour for carbons.

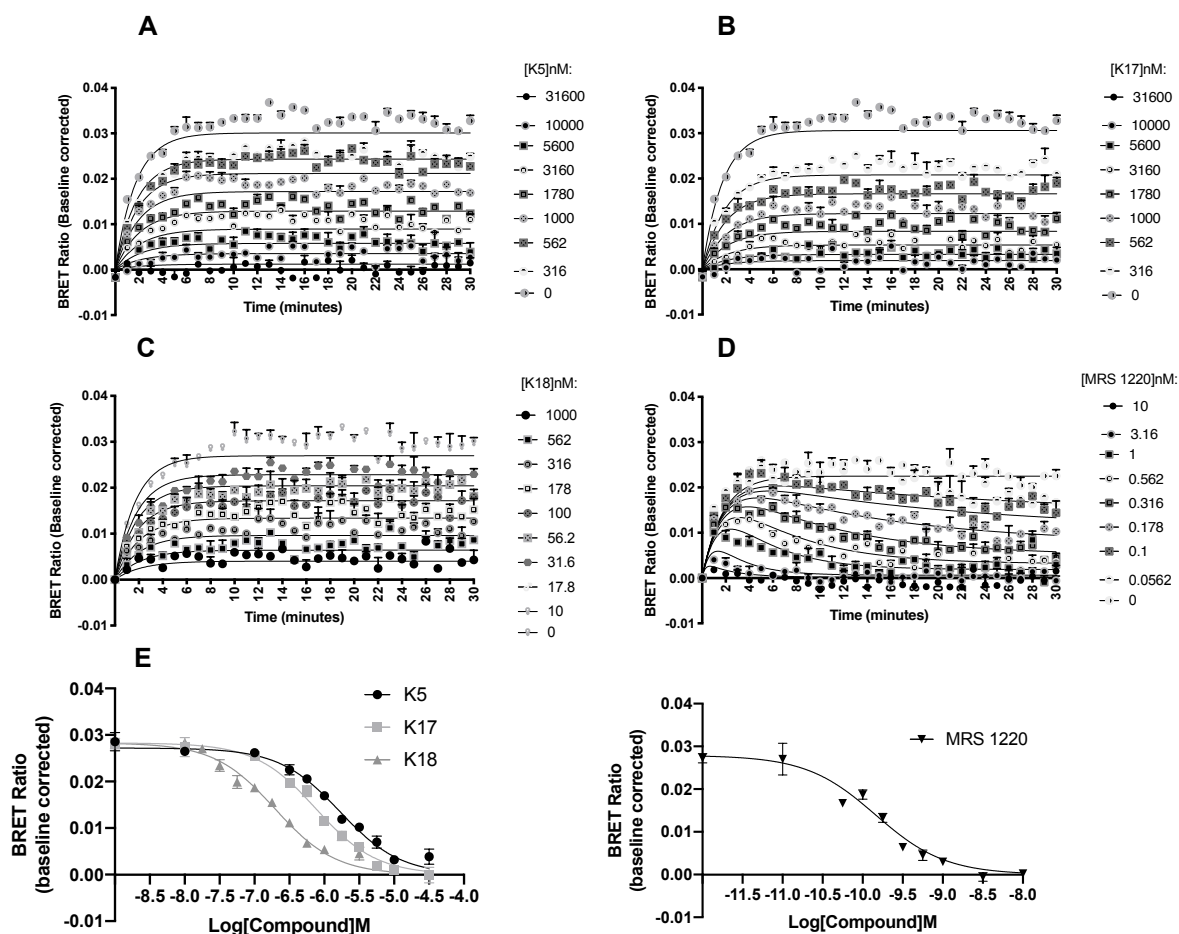




**Supplementary Figure 11.  $pA_2$  values obtained through Schild analysis are agonist independent.** Flp-In-CHO cells (2000 cells/well) stably expressing WT or L90A<sup>3,32</sup> A<sub>3</sub>R were exposed to forskolin 10  $\mu$ M, agonist (NECA or IB-MECA) and K18 at varying concentrations for 30 min and cAMP accumulation detected. IC<sub>50</sub> values determined through fitting three-parameter logistic equation to concentration response data were used to conduct Schild analysis.



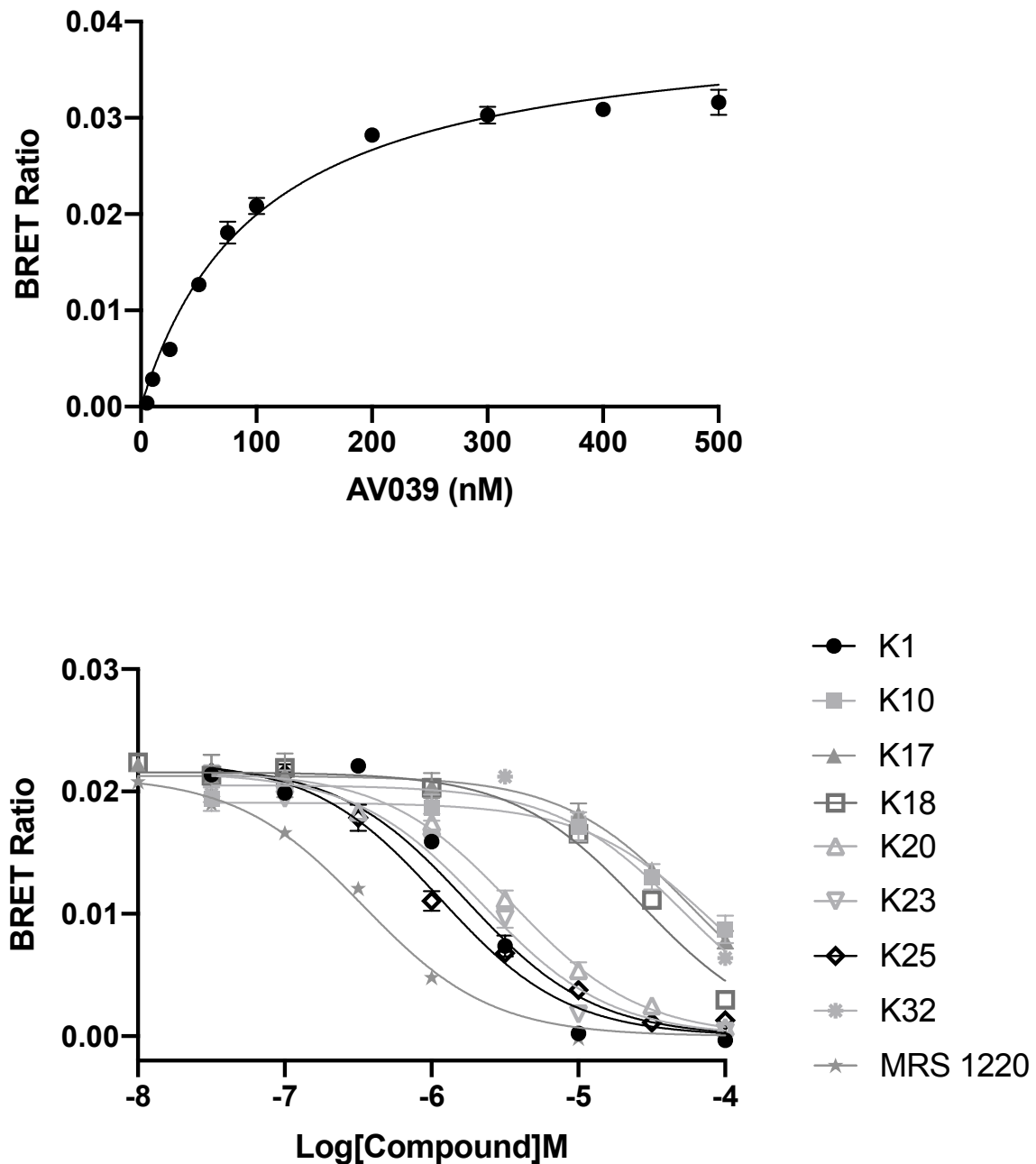
**Supplementary Figure 12. Kinetic measurements of CA200645 binding to Nluc-A<sub>3</sub>R.** HEK 293 cells stably expressing Nluc-A<sub>3</sub>R were stimulated with the fluorescent ligand CA200645 at the indicated concentration. BRET between Nluc and the CA200645 was measured every 5 seconds for 30 minutes at room temperature. Determined kinetic parameters for CA200645 at Nluc-A<sub>3</sub>R were  $K_{on} = 2.86 \pm 0.89 \times 10^7 \text{ M}^{-1}$  and  $K_{off} = 0.4397 \pm 0.014 \text{ min}^{-1}$  with a resulting  $K_D$  of  $17.92 \pm 4.45 \text{ nM}$ . Data were baseline corrected and shown here as representative of five independent experiments, conducted in duplicate.



**Supplementary Figure 13. Inhibition of BRET between Nluc and CA200645 at the A<sub>3</sub>R by K5, K17, K18 and MRS 1220.** HEK293 cells stably expressing Nluc-A<sub>3</sub>R were treated with 5 nM CA200645 and increasing concentrations of unlabelled compound (represented in nM) **A**) K5, **B**) K17, **C**) K18 or **D**) MRS 1220. For MRS 1220, this trace demonstrates a classic tracer ‘overshoot’, as has been previously described observed when the unlabelled compound has a slower off rate than the labelled CA200645 ( $K_{off}$  of  $0.4397 \pm 0.014 \text{ min}^{-1}$  and  $0.0248 \pm 0.005 \text{ min}^{-1}$ , respectively) (Sykes *et al.*, 2019, Motulsky and Mahan, 1984; built into Prism). The data shown are representative of three independent experimental repeats (mean  $\pm$  SEM) fitted with the appropriate model, as determined by statistical comparison between our new model (“Kinetics of competitive binding, rapid competitor dissociation”, derived in the Appendix I) (K5, K17 and K18) or the ‘kinetic of competitive binding’ model (built into Prism) for MRS 1220. (See Materials and Methods for fitting procedure and statistical comparison method.) **E**) The resulting concentration dependent decrease in BRET ratio at 10 minutes was taken to calculate  $pK_i$  through fitting the Cheng-Prusoff equation. Each data point represents mean  $\pm$  SEM of five experiments performed in duplicate.

residues	15	72	73	90	91	94	165	166	167	168	169	174	177	243	246	249	250	253	264	268
hA3	Y	V	S	L	L	T	S	C	Q	F	V	M	M	W	L	I	N	I	L	I
rA3	Y	V	S	L	L	T	S	C	H	F	R	L	M	W	L	I	N	S	M	I

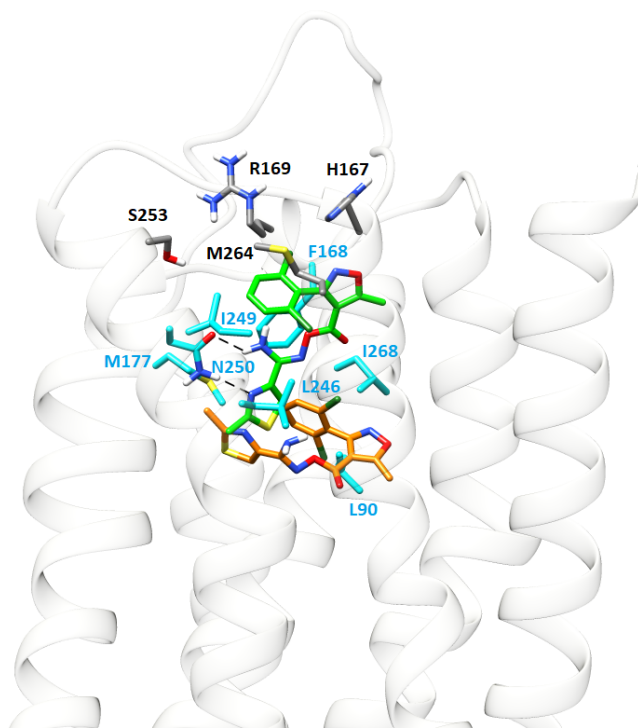
**Supplementary Figure 14. Comparison of the residues of the orthosteric binding area in human and rat A<sub>3</sub>Rs.**



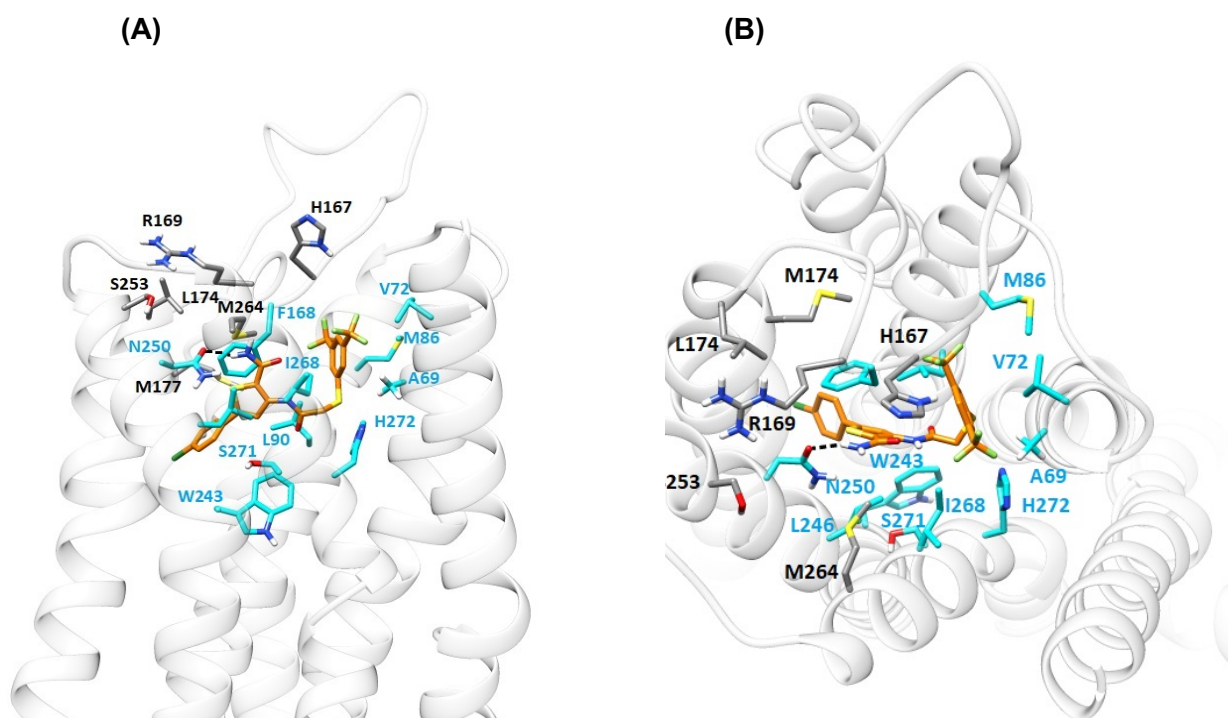
**Supplementary Figure 15. NanoBRET radioligand binding at the rat  $A_3R$ .** **A)** Saturation binding experiment with AV039 with a  $K_D$  determined as  $102 \pm 7.59$  nM through fitting the 'One site – Specific binding' model in Prism. Each data point represents mean  $\pm$  SEM of  $n = 5$  experiments, performed in duplicate. **B)** Inhibition of BRET between Nluc and AV039 at the rat  $A_3R$  by MRS 1220 and K compounds. HEK293 cells stably expressing Nluc-rat  $A_3R$  were treated with 100 nM AV039 and increasing concentrations of unlabelled compound. The resulting concentration dependent decrease in BRET ratio at 5 minutes was taken to calculate  $pK_i$  through fitting the Cheng-Prusoff equation. Each data point represents mean  $\pm$  SEM of  $n$  ( $n=5$  for MRS 1220, K1, K20, K23 and K25,  $n=3$  for K10, K17, K18 and K32) experiments, performed in duplicate.

**Supplementary Table 7. Binding of compounds to the rat A<sub>3</sub>R.** Equilibrium dissociation constant of MRS 1220 and K compounds as determined through NanoBRET ligand-binding ( $pK_i$ )

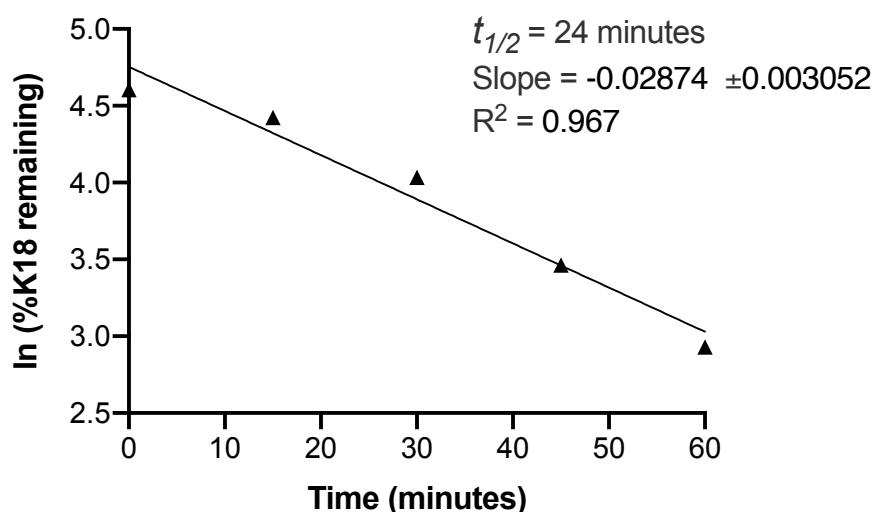
	$pK_i$	$n$
<b>MRS 1220</b>	6.74 ±0.04	5
<b>K1</b>	6.07 ±0.05	5
<b>K10</b>	4.19 ±0.09	3
<b>K17</b>	4.60 ±0.09	3
<b>K18</b>	4.60 ±0.04	3
<b>K20</b>	5.71 ±0.03	5
<b>K23</b>	5.93 ±0.04	5
<b>K25</b>	6.37 ±0.06	5
<b>K32</b>	4.05 ±0.10	3



**Supplementary Figure 16 .** Rat A<sub>3</sub>R in complex with K18. Starting pose (carbons of the ligand in green), after 100 ns MD simulation (carbons of the ligand in orange). Light blue sticks show residues conserved with human A<sub>3</sub>R. M264<sup>7,34</sup> most likely hampers K18 binding due to steric hindrance of the dichloro-phenyl group



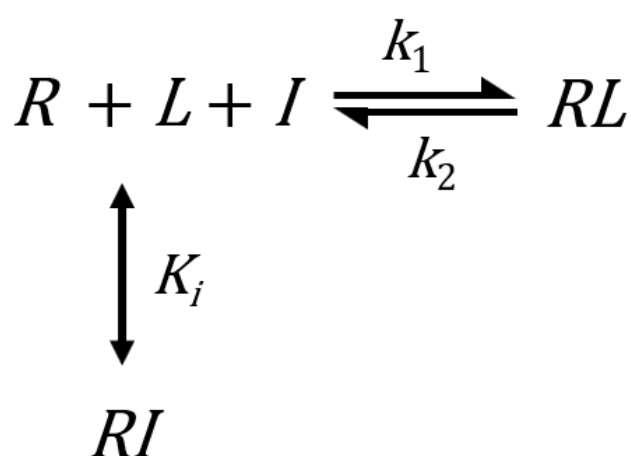
**Supplementary Figure 17.** Average structure of rat A<sub>3</sub>R in complex with K25 from 100 ns MD simulations (carbons of the ligand are shown in orange sticks and light blue sticks show residues in contact with K25). K25 was docked into the orthosteric site of the rat A<sub>3</sub>R using the GoldScore scoring function and the highest scoring pose was inserted in a hydrated POPE bilayer. The complexes were subjected to MD simulations with Amber14ff and K25 adopts a potential binding pose within the orthosteric binding area (A) Side view. (B) Top view.



**Supplementary Figure 18. Intrinsic clearance of K18.** The metabolic stability of K18 (0.1  $\mu$ M) was studied using human liver microsomes (0.1 mg/mL) to derive the metabolic half-life ( $t_{1/2}$ ) from the slope ( $k$ ). The  $t_{1/2}$  of K18 was determined as 24 minutes using the equation:  $t_{1/2} = -\ln(2)/k$ . Intrinsic clearance ( $CL_{int}$ ) was calculated as 287.2  $\mu$ l/min/mg. Each data point represents the mean  $\pm$  SEM of a single test conducted in duplicate.

## Appendix I: Adapting the kinetics of competitive binding equation for rapidly-dissociating unlabelled ligands

The Motulsky and Mahan equation is used to measure the association and dissociation rate constant of unlabelled compounds, in competition with labelled ligand for binding to a receptor (Motulsky and Mahan, 1984). When the unlabelled competitor dissociates rapidly, relative to the early time points of the assay, the fitted parameters can indicate a failure of the fit to provide realistic or sufficiently precise estimates of the model parameters. Here an equation is derived for rapidly-dissociating compounds that provides an estimate of the equilibrium binding affinity rather than the binding rate constants of the unlabelled competitor. It is assumed the competitor is at equilibrium throughout the time course of the binding assay. This is represented by the following scheme, where  $K_i$  is the equilibrium dissociation constant of the competitor:



$R$  is receptor,  $L$  is labelled ligand,  $I$  is unlabelled competitor,  $k_1$  is the association rate constant and  $k_2$  the dissociation rate constant of the labelled ligand. The assumptions underlying the original kinetics of competitive binding equation apply (Motulsky and Mahan, 1984): Only a small fraction (< 10%) of total tracer and compound concentration is bound by receptor ("Zone A"); receptor is exposed simultaneously to both ligands; receptor-ligand binding conforms to a single-site, single-step non-cooperative mass-action mechanism; and unlabelled ligand competitively inhibits tracer binding.

The goal is an equation that describes binding of labelled ligand to receptor over time in the presence of unlabelled competitor. We start with the differential equation for  $[RL]$ :

$$\frac{d[RL]}{dt} = [R][L]k_1 - [RL]k_2$$

Next,  $R$  is substituted by employing the conservation of mass equation:

$$N = [R] + [RI] + [RL]$$

where  $N$  is the total concentration of receptor. Solving for  $[R]$  gives,

$$[R] = N - [RI] - [RL]$$

This expression is now substituted into the differential equation for  $[RL]$ :

$$\frac{d[RL]}{dt} = N[L]k_1 - [RI][L]k_1 - [RL]([L]k_1 + k_2)$$

We now substitute  $[RI]$  with an expression in terms of  $[RL]$ , as follows: Since  $I$  is at equilibrium with the receptor, the ratio of  $R$  to  $RI$  is constant, and can be represented by the following expression:

$$\frac{[RI]}{[R] + [RI]} = \frac{[I]}{K_I + [I]} = \rho_I$$

where the constant  $\rho_I$  is fractional occupancy by  $I$  of accessible receptors, i.e. those not bound by labelled ligand. Next, this equation is rearranged as follows:

$$[RI] = \rho_I([R] + [RI])$$

The bracketed term on the right-hand side,  $[R] + [RI]$  can be re-written in terms of  $[RL]$  and the constant  $N$ , using the conservation of mass equation for the receptor:

$$[R] + [RI] = N - [RL]$$

$[R] + [RI]$  is now substituted with  $N - [RL]$ :

$$[RI] = \rho_I(N - [RL])$$

This is the desired expression:  $[RI]$  is expressed in terms of  $[RL]$ . This expression is now substituted into the differential equation for  $[RL]$ , which gives, after rearranging,

$$\frac{d[RL]}{dt} = N[L]k_1(1 - \rho_I) - [RL]\{[L]k_1(1 - \rho_I) + k_2\}$$

This equation is now integrated to obtain the  $[RL]$  vs  $t$  equation that can be used to fit experimental data:

$$[RL]_t = \frac{N[L]k_1(1 - \rho_I)}{k_{obs,+I}}(1 - e^{-k_{obs,+I}t})$$

where

$$k_{obs,+I} = [L]k_1(1 - \rho_I) + k_2$$

and

$$\rho_I = \frac{[I]}{K_I + [I]}$$



## Appendix II: Supporting information for computational biochemistry

### Preparation of the structures

Structures of the compounds K5, K17, K18 or MRS 1220 were prepared using Maestro (Version 10.5; Schrodinger, Inc.: New York, NY, 2015) and minimized as in a previous paper (Lagarias *et al.*, 2018). The inactive state homologue of A<sub>3</sub>R WT was taken from Adenosiland web-service (Floris *et al.*, 2012). The BLAST algorithm estimated the human A<sub>1</sub>R (Glukhova *et al.*, 2017; PDB ID 5UEN) as the most appropriate template for human A<sub>3</sub>R model having the most similar sequence. The rat A<sub>3</sub>R was generated using the protein structure homology model server SwissModel (Waterhouse *et al.*, 2018). We also applied MODELLER 9.18 (Šali and T. L. Blundell, 1993, Eswar *et al.*, 2003) which selected ten PDB structures with the highest sequential similarity as templates for homology modeling of rat A<sub>3</sub>R. Twenty homology models were generated and the model with the lowest DOPE (Discrete Optimized Protein Energy) value was selected. The two resulting rat A<sub>3</sub>R models created by Swiss Model and MODELLER 9.18 were compared to each other using the Protein Structure Alignment Tool of Desmond Maestro 2018-1 and were found to be very similar (Desmond Molecular Dynamics System, version 3.0; D.E. Shaw Res. New York, 2011; Maest. Interoperability Tools, 3.1; Schrodinger Res. New York, 2012).

The protein models were optimized as previously published using the Protein Preparation Wizard implementation in Schrodinger suite (Protein Prep. Wizard 2015-2; Epik version 2.4, Schrödinger, LLC, New York, NY, 2015; Impact version 5.9, Schrödinger, LLC, New York, NY, 2015; Prime version 3.2, Schrödinger, LLC, New York, NY, 2015). The ZM241385-inactive A<sub>2A</sub>R protein complex from 3EML (Jaakola *et al.*, 2008) was superimposed to human or rat A<sub>3</sub>R WT and the A<sub>2A</sub>R protein was removed resulting in ZM241385-A<sub>3</sub>R complex which was used as a template for docking of K5, K17, K18, K25 or MRS 1220 using GoldScore and ChemPLP scoring functions (Jones *et al.*, 1997, Eldridge *et al.*, 1997) and the GOLD (Version 5.2, Cambridge Crystallogr. Data Cent. Cambridge, U.K., 2015) (Verdonk *et al.*, 2005) as previously described (Lagarias *et al.*, 2018). The top high-scoring poses for K5, K17, K18, K25 or MRS 1220 in complex with A<sub>3</sub>R using GoldScore were better and were kept. These complexes were embedded in POPE bilayers using the System Builder utility of Desmond (Desmond Molecular Dynamics System, version 3.0; D.E. Shaw Res. New York, 2011; Maest. Interoperability Tools, 3.1; Schrodinger Res. New York, 2012). Complex and lipid systems were solvated using the TIP3P water model (Jorgensen, 1983). Na<sup>+</sup> and Cl<sup>-</sup> ions were placed in the water phase to neutralize the systems and to reach the experimental salt concentration of 0.150 M NaCl. A 10 Å-from the solute atoms-buffered orthorhombic system with periodic boundary conditions was constructed for all complexes.

### MD simulations

Each ligand-A<sub>3</sub>R complex in the bilayer was processed by the LEaP module in AmberTools14 under the AMBER14 software package (Case *et al.*, 2014). Amber ff14SB force field parameters (Maier *et al.*, 2015) was applied to the protein, lipid14 to the lipids (Dickson *et al.*, 2014), GAFF to the ligands (Wang *et al.*, 2004) and TIP3P (Jorgensen, 1983) to the water molecules for the calculation of bonded, vdW parameters and electrostatic interactions. Atomic charges were computed according to the RESP procedure (Bayly *et al.*, 1993) using Gaussian03 (Frisch *et al.*, 2003) and *antechamber* of AmberTools14. MD simulations in explicit solvent were performed using PMEMD (Case *et al.*, 2014). MD simulation protocol consists of five stages: a) Minimization, b) Heating, c) Adjustment of density, d) Equilibration

and e) Production. The systems were minimized by 2500 steps of steepest descent to remove bad contacts and 7500 steps of conjugated gradient minimization in the presence of a harmonic restraint with a force constant of  $5 \text{ kcal mol}^{-1} \text{ \AA}^{-2}$  on all atoms of protein and ligand and non-bonded cut-off of  $8.0 \text{ \AA}$ . The next stage in MD simulation protocol is to allow the system to heat up from 0 K to 310 K. Langevin thermostat (dynamics) (Izaguirre *et al.*, 2001) as implemented in Amber14 (Case *et al.*, 2014) was used for temperature control employing a Langevin collision frequency of  $2.0 \text{ ps}^{-1}$ . The system in two consecutive steps to 310 K in the presence of a harmonic restraint with a force constant of  $10 \text{ kcal mol}^{-1} \text{ \AA}^{-2}$  on all membrane, protein, and ligand atoms. In the first step, systems were heated to 100 K in a NVT of 50 ps length where the adjustment of the density was realized using the Berendsen barostat (Berendsen *et al.*, 1984) with a 2 ps coupling time. In the second step, the temperature was raised to 310 K in a NPT $\gamma$  (with  $\gamma = 10 \text{ dyn cm}^{-1}$ ) simulation of 500 ps length. Subsequently, the systems were equilibrated without restraints in a NPT $\gamma$  simulation of 1 ns length with  $T = 310 \text{ K}$  and  $\gamma = 10 \text{ dyn cm}^{-1}$ . The equilibration phase was followed by production simulation for 100 ns with system-specific lengths using the same protocol as in the final equilibration step. In the NPT $\gamma$  simulations semiisotropic pressure scaling to  $p = 1 \text{ bar}$  was applied using a pressure relaxation time of 1.0 ps. For the treatment of long-range electrostatic interactions, the Particle-mesh Ewald summation method (Darden *et al.*, 1993, Essmann *et al.*, 1995) was used, and short-range non-bonding interactions were truncated with an  $8 \text{ \AA}$  cutoff. Bonds involving hydrogen atoms were constrained by the SHAKE algorithm (Ryckaert *et al.*, 1977), and a time step of 2 fs was used for the integration of the equations of motion. Snapshots recorded every 20 ps during the production Properties and dynamics of the protein and ligand systems as well as of the membrane were analyzed with the *ptraj* and *cpptraj* modules of AmberTools12 (Case *et al.*, 2014).

## REFERENCES

- Berendsen, H. J. C., Postma, J. P. M., van Gunsteren, W. F., DiNola, A., & Haak, J. R. (1984). Molecular dynamics with coupling to an external bath. *Journal of Chemical Physics*, **81**(8), 3684. DOI: 10.1063/1.448118
- Case, D. A., Babin, V., Berryman, J. T., Betz, R. M., Cai, Q., Cerutti, D. S., & Kollman, P. A. (2014). AMBER 14. University of California, San Francisco.
- Darden, T., York, D., & Pedersen, L. (1993). Particle mesh Ewald: An N-log(N) method for Ewald sums in large systems. *Journal of Chemical Physics*, **98**(12), 10089. DOI: 10.1063/1.464397
- Dickson, C. J., Madej, B. D., Skjevik, A. A., Betz, R. M., Teigen, K., Gould, I. R., & Walker, R. C. (2014). Lipid14: The Amber Lipid Force Field. *Journal of Chemical Theory and Computation*, **10**(2), 865–879. DOI: 10.1021/ct4010307
- Eswar, N., John, B., Mirkovic, N., Fiser, A., Ilyin, V. A., Pieper, U., et al. (2003). Tools for comparative protein structure modeling and analysis. *Nucleic Acids Research*, **31**(13), 3375–3380. <http://doi.org/10.1093/nar/gkg543>
- Eldridge, M. D., Murray, C. W., Auton, T. R., Paolini, G. V., & Mee, R. P. (1997). Empirical scoring functions: I. The development of a fast empirical scoring function to estimate the binding affinity of ligands in receptor complexes. *Journal of Computer-Aided Molecular Design*, **11**(5), 425–445.
- Essmann, U., Lalić Perera, Berkowitz, M. L., Darden, T., Lee, H., & Pedersen, L. G. (1995). A smooth particle mesh Ewald method. *Journal of Chemical Physics*, **103**(19), 8577. DOI: 10.1063/1.470117

- Floris, M., Sabbadin, D., Medda, R., Bulfone, A., & Moro, S. (2012). Adenosiland: walking through adenosine receptors landscape. *European Journal of Medicinal Chemistry*, **58**, 248–257. DOI: 10.1016/j.ejmech.2012.10.022
- Frisch, M. J., Trucks, G. W., Schlegel, H. B., Scuseria, G. E., Rob, M. A., & Pople, J. A. (2003). *Gaussian 03*. Wallingford, CT.
- Glukhova, A., Thal, D. M., Nguyen, A. T., Vecchio, E. A., Jörg, M., Scammells, P. J., et al. (2017). Structure of the Adenosine A1 Receptor Reveals the Basis for Subtype Selectivity. *Cell*, **168**(5), 867–877.e13. <http://doi.org/10.1016/j.cell.2017.01.042>
- Izaguirre, J. A., Catarello, D. P., Wozniak, J. M., & Skeel, R. D. (2001). Langevin stabilization of molecular dynamics. *Journal of Chemical Physics*, **114**(5), 2090. DOI: 10.1063/1.1332996
- Jaakola, V.-P., Griffith, M. T., Hanson, M. A., Cherezov, V., Chien, E. Y. T., Lane, J. R., et al. (2008). The 2.6 angstrom crystal structure of a human A2A adenosine receptor bound to an antagonist. *Science (New York, N.Y.)*, **322**(5905), 1211–1217. DOI: 10.1126/science.1164772
- Jones, G., Willett, P., Glen, R. C., Leach, A. R., & Taylor, R. (1997). Development and validation of a genetic algorithm for flexible docking. *Journal of Molecular Biology*, **267**(3), 727–748. DOI: 10.1006/jmbi.1996.0897
- Jorgensen, W. L., Chandrasekhar, J., Madura, J. D., Impey, R. W., & Klein, M. L. (1983a). Comparison of Simple Potential Functions for Simulating Liquid Water. *Journal of Chemical Physics*, **79**(2), 926–935. DOI: 10.1063/1.445869
- Lagarias, P., Vrontaki, E., Lambrinidis, G., Stamatis, D., Convertino, M., Ortore, G., et al. (2018). Discovery of Novel Adenosine Receptor Antagonists through a Combined Structure- and Ligand-Based Approach Followed by Molecular Dynamics Investigation of Ligand Binding Mode. *Journal of Chemical Information and Modeling*, **58**(4), 794–815. DOI: 10.1021/acs.jcim.7b00455
- Maier, J. A., Martinez, C., Kasavajhala, K., Wickstrom, L., Hauser, K. E., & Simmerling, C. (2015). ff14SB: Improving the Accuracy of Protein Side Chain and Backbone Parameters from ff99SB. *Journal of Chemical Theory and Computation*, **11**(8), 3696–3713. DOI: 10.1021/acs.jctc.5b00255
- Motulsky, H. J. (n.d.). Interpreting the extra sum-of squares F test. Retrieved May 30, 2019, from Motulsky, H. J., & Mahan, L. C. (1984). The Kinetics of Competitive Radioligand Binding Predicted by the Law of Mass-Action. *Molecular Pharmacology*, **25**(1), 1–9.
- Ryckaert, J.-P., Ciccotti, G., & Berendsen, H. J. C. (1977). Numerical integration of the Cartesian Equations of Motion of a System with Constraints: Molecular Dynamics of n-Alkanes. *Journal of Computational Physics*, **23**(3), 327–341.
- Sali, A., & Blundell, T. L. (1993). Comparative protein modelling by satisfaction of spatial restraints. *Journal of Molecular Biology*, **234**(3), 779–815. <http://doi.org/10.1006/jmbi.1993.1626>
- Sykes, D. A., Stoddart, L. A., Kilpatrick, L. E., & Hill, S. J. (2019). Binding kinetics of ligands acting at GPCRs. *Molecular and Cellular Endocrinology*, **485**, 9–19. DOI: 10.1016/j.mce.2019.01.018
- Verdonk, M. L., Chessari, G., Cole, J. C., Hartshorn, M. J., Murray, C. W., Nissink, J. W. M., et al. (2005). Modeling water molecules in protein-ligand docking using GOLD. *Journal of Medicinal Chemistry*, **48**(20), 6504–6515. DOI: 10.1021/jm050543p
- Wang, J. M., Cieplak, P., & Kollman, P. A. (2000). How well does a restrained electrostatic potential (RESP) model perform in calculating conformational energies of organic and biological molecules? *Journal of Computational Chemistry*, **21**(12), 1049–1074. DOI: 10.1002/1096-987X(200009)21:12<1049::AID-JCC3>3.3.CO;2-6
- Waterhouse, A., Bertoni, M., Bienert, S., Studer, G., Tauriello, G., Gumienny, R., et al. (2018). SWISS-MODEL: homology modelling of protein structures and complexes. *Nucleic Acids Research*, **46**(W1), W296–W303. <http://doi.org/10.1093/nar/gky427>